2008

Modeling and direct numerical simulation of particle-laden turbulent flows

Ying Xu
Iowa State University

Modeling and direct numerical simulation of particle–laden turbulent flows

by

Ying Xu

A dissertation submitted to the graduate faculty

in partial fulfillment of the requirements for the degree of

DOCTOR OF PHILOSOPHY

Co-majors: Mechanical Engineering

Applied Mathematics

Program of Study Committee:
Glenn R. Luecke, Co-major Professor
Shankar Subramaniam, Co-major Professor
Theodore J. Heindel
James C. Hill
Richard H. Pletcher
Jue Yan

Iowa State University

Ames, Iowa

2008

TABLE OF CONTENTS

LIST OF TABLES

LIST OF FIGURES

ACKNOWLEDGMENTS

I would like to take this opportunity to express my thanks to those who helped me with various aspects of conducting research and the writing of this thesis. My sincere gratitude goes to Dr. Shankar Subramaniam for his guidance, patience and support through this research. I would like to express my thanks to Dr. Glenn Luecke for exposing the parallel computing to me. My warmest regards goes to Profs. Richard Pletcher, Theodore Heindel, James Hill and Jue Yan for their invaluable time.

Many thanks to to Madhu Pai, Rahul Garg, Sergiy Markutsya, Sudheer Tenneti and Vidyapati for collaborations and interesting discussions on research, course work. I would also like to express my gratitude to all the graduate students in the Computational Fluid Dynamics center, especially Kunlun Liu, Zhaohui Qin, Jin Sun, Wen Wang, Nan Xie and Xiaofeng Xu.

I am indebted to my husband and my parents for their invaluable support during my Ph.D study. Without their loving care, support and encouragement I will not be able to finish my degree here at Iowa State University.

ABSTRACT

The objective of this study is to improve Eulerian–Eulerian models of particle–laden turbulent flow, especially the interphase TKE transfer term and the dissipation rate in Eulerian–Eulerian models. We begin by understanding the behavior of two existing models—one proposed by Simonin (1996b), and the other by Ahmadi (1989)—in the limiting case of statistically homogeneous particle–laden turbulent flow. The decay of particle-phase and fluid-phase turbulent kinetic energy (TKE) is compared with point-particle direct numerical simulation data. Even this simple flow poses a significant challenge to current models, which have difficulty in reproducing important physical phenomena such as the variation of turbulent kinetic energy decay with increasing particle Stokes number. The model for the interphase TKE transfer timescale is identified as one source of this difficulty. A new model for the interphase transfer timescale is proposed that accounts for the interaction of particles with a range of fluid turbulence scales. A new multiphase turbulence model—the Equilibration of Energy Model (EEM)—is proposed, which incorporates this multiscale interphase transfer timescale. The model for Reynolds stress in both fluid and particle phases is derived in this work. The new EEM model is validated in decaying homogeneous particle–laden turbulence, and in particle–laden homogeneous shear flow. The particle and fluid TKE evolution predicted by the EEM model correctly reproduce the trends with important non-dimensional parameters, such as particle Stokes number.

The interphase transfer of turbulent kinetic energy (TKE) is an important term that affects the evolution of TKE in fluid and particle phases in particle–laden turbulent flow. In this work, we show that the interphase TKE transfer terms must obey a mathematical constraint, which in the limiting case of statistically homogeneous flow with zero mean velocity in both

phases, requires these terms be equal and opposite. In the single–point statistical approach called the two–fluid theory, the interphase TKE transfer terms are unclosed and need to be modeled. Multiphase turbulence models that satisfy this constraint of conservative interphase TKE transfer admit a term-by-term comparison with true direct numerical simulations (DNS) that enforce the exact velocity boundary condition on each particle's surface. Analysis of three models reveals that not all models satisfy the requirement of conservative interphase TKE transfer. DNS that invoke the point–particle assumption also do not obey this principle of conservative interphase TKE transfer, and this precludes comparison of model predictions of TKE budgets in each phase with point–particle DNS. This study motivates the development of multiphase turbulence models based on the insights revealed by this analysis, leading to a meaningful comparison of TKE budgets with true DNS.

The immersed boundary method has the ability to simulate the irregular shape objects on the uniform Cartesian grids. In this work, the true DNS using the immersed boundary method is developed, and the drag force coefficient obtained from DNS is verified with laminar flow past a stationary sphere and a single sphere in the homogeneous turbulence. However the memory requirement of the immersed boundary method is found to be quite high and the parallelization of the immersed boundary method is necessary. The idea of the domain decomposition is used to parallelize the numerical solver for the immersed boundary method in this work, and the performance is studied for the resolution of $512 \times 256 \times 256$.

The parallel immersed boundary method is used to study the effects of particle clusters on fluid phase turbulence. This study is inspired by the experiments of Moran and Glicksman Moran and Glicksman (2003a), where the fluid phase fluctuations are found to be enhanced at the high particle concentration, where particle clusters usually form in the CFB. In the DNS study, we use two types of random particle configurations and study the fluid phase TKE in the fixed bed of spheres. The uniform random particle configuration is denoted as MHC and the one with clusters is denoted as GCG in this study. The DNS study shows that the fluid phase TKE is enhanced with GCG along the streamwise direction in the fixed bed. For both MHC and GCG, the fluid phase Reynolds stress is found to be anisotropic. The 2D energy spectra

studies show that the energy of GCG at lower wavenumber $\kappa < 10$ is higher than that of MHC. The cutoff wavenumber corresponds to the cluster size estimated using the radius of gyration. After examining the dissipation, and interphase TKE transfer term in the transport equation for Reynolds stress, it is noted that the dissipation is reduced in the second half of the fixed bed for GCG. Both the dissipation and the interphase TKE transfer term become anisotropic in the fixed bed, and the state of anisotropy described by the invariants of anisotropic tensor b_{ij} shows that the degree of anisotropy is higher for the interphase TKE transfer tensor compared to that of the dissipation tensor. This study suggests that the length scale based on the particle cluster should be used to estimate the level of gas fluctuations caused by the solid phase, and should be accounted for in multiphase turbulence models.

CHAPTER 1. INTRODUCTION

1.1 Background

Particle–laden flows are abundant in nature and can be found in various industrial systems. Pneumatic conveying systems in chemical, food and pharmaceutical industries, and the transport of pollutants in the atmosphere are typical examples. Energy production systems such as droplets in internal combustion engines, fluidized bed combustions and gasification for coal and biomass involve efforts to find a combustion process conducive to controlling pollutant emissions and efficient energy generation.

It is helpful, before discussing the modeling and simulation methods for particle–laden flows, to classify the regimes of particle–laden flows from the perspective of the interaction between particles and fluid phase motions. Elghobashi (1991) classifies dilute and dense suspensions of particle–laden flow based on the mean distance S between the centers of two neighboring particles and particle diameter d. If $S/d > 10$, the particle–laden flow is considered to be a dilute suspension; if $S/d < 10$, it is considered to be a dense suspension. The mean distance S between the centers of two neighboring particles S, is a second-order statistic from a stochastic point process view point. For the special case of a statistically homogeneous system, S can be related to the particle volume fraction α_p of the system, but in general S is not completely determined by α_p. The particle volume fraction is the ratio of total volume of particle to the system volume.

Crowe el al. (1998) defines dilute dispersed flows as those in which the particle motion is controlled by the hydrodynamic forces (drag and lift). A dense flow is one in which the particle motion is controlled by collisions. A qualitative estimate of the dilute or dense mixture is made by comparing the ratio of particle momentum response time τ_p to the time between particle

collisions τ_C. The time between collisions can be estimated from the collision frequency, and τ_V/τ_C is related to the Reynolds number Re_T and the volume fraction α_p, where Re_T is the particle Reynolds number based on the particle granular temperature. A simple way of classifying the dense and dilute particle–laden flows is based on the particle volume fraction α_p. In industrial processes like fluidized beds, a particulate flow with $\alpha_p < 0.15$ is considered to be dilute. For dilute gas-solid flows, the particle Reynolds number Re_p is usually defined as

$$Re_p \equiv \frac{\rho_f d_p}{\mu}|\mathbf{v} - \mathbf{u}| \tag{1.1}$$

where ρ_f is the fluid thermodynamic density, d_p is the particle diameter, μ is the fluid dynamic viscosity and $|\mathbf{v} - \mathbf{u}|$ is the mean slip velocity between fluid and particle phase.

Dilute particle–laden flows can be further classified according to the mass loading of the mixture, as suggested by Elghobashi (1991). The mass loading is defined as the ratio of total mass of particles to the mass of carrier fluid. In general, for dilute gas–solid flows with volume fraction α_p of order 10^{-6} and mass loading $\phi \ll 1$, one-way coupling is valid, which means that the particle phase has a negligible effect on the fluid-phase motions. The drag force is usually a function of the particle Reynolds number Re_p. The smaller the particle size d_p and particle density ρ_f, the less influence the particles exert on fluid phase motions.

Turbulence in the fluidized bed, for example in the free board of the bed, promotes effective mixing and efficient heat transfer, and it also entrains more particulates into the product gas exiting from the bed. A better understanding of turbulent gas–solid flows helps to improve the efficiency of the industrial applications. Turbulence is generally considered to be suppressed in dense phase gas–particle flows with $\alpha_p > 0.1$, since particle–particle interactions are dominant.

For dilute particle–laden turbulence, which is low in volume fraction (α_p of order 10^{-3} or higher), but with relatively high mass loading ratio ($\phi \geq 1$ due to high thermodynamic density of the particle phase), the influence of particles on the carrier phase mass conservation equation is often neglected, and so are inter–particle collisions. However, the interphase momentum transfer is significant, and hence the carrier phase turbulence is altered by the dispersed phase, and "two-way" coupling needs to be taken into consideration.

Dilute particle–laden turbulent flows with significant mass loading ratio ϕ can be found

in various industrial systems. Several parameters become important in these systems. One is the ratio between the Kolmogorov length scale η and the mean particle diameter d_p, which is usually found to be around one. The other physical parameter is the particle Stokes number $St > 1$ [Moran and Glicksman (2003a)], which is defined as

$$St \equiv \frac{\tau_p}{\tau_f} \tag{1.2}$$

where τ_p is the particle momentum response time and τ_f is a characteristic fluid time scale [1]. According to practical interests and the classification described above, this research focuses on the particle–laden turbulent flows that are low in volume concentration, but with significant mass loading ratio, hence two–way coupling should be taken into account.

There are several key effects and phenomena of particle–laden turbulent flows that are found in the industrial processes like fluidized beds and it is necessary to capture and predict these key effects in modeling and simulation studies. Interactions between particles and fluid phase turbulence lead to the changes in the fluid phase turbulence intensity and the fluid phase dissipation rate. Many direct numerical simulations (DNS) [Squires and Eaton (1990); Elghobashi and Truesdell (1993); Boivin et al. (1998); Sundaram and Collins (1999)] and experimental studies [Tsuji et al. (1984); Bolio et al. (1995); Bolio and Sinclair (1995); Hwang and Eaton (2006a)] report the modulation of turbulence with variation of particle Stokes number St, mass loading ϕ. In the experimental studies of particle–laden homogeneous turbulence by Hwang and Eaton (2006a), the fluid phase turbulent kinetic energy (TKE) is found to decrease with increasing mass loading, which is also reported in DNS studies [Squires and Eaton (1990); Elghobashi and Truesdell (1993); Boivin et al. (1998); Sundaram and Collins (1999)]. The fluid phase TKE modulates differently with particle Stokes number St, that is the decay rate of fluid phase TKE increases with increasing particle Stokes number (for fixed mass loading ratio) in homogeneous turbulence [Sundaram and Collins (1999); Boivin et al. (1998)].

For dilute particle–laden turbulence, the addition of particle phase to a turbulent flow

[1] The particle momentum response time is defined as the time required for a particle relaxed from rest to achieve 63% ($(e-1)/e$) of the free stream velocity [Crowe el al. (1998)], which is a measure of the particle inertia. Particles with $St \ll 1$ correspond to tracer particles and ideally will follow the flow; while particles with $St > 1$ correspond to particles with large inertia, and will not respond to the small fluctuations in the carrier fluid field.

introduces not only new time and length scales, but many other parameters, such as the particle mass loading ϕ, volume fraction α_p, Stokes number St and Reynolds number Re_p. The interaction of turbulence length and time scales with those in the particle phase make this a multiscale interaction problem. Turbulence modulation with variation in particle Stokes number and mass loading discussed earlier is such a multiscale phenomenon that manifests itself over a wide range of length and time scales. True DNS can resolve all the time and length scales in the problem, which makes it a useful tool to study the multiscale interaction problem. The efficient design of transport systems and the control of combustion process rely on the reliable and efficient simulation tools, which can provide valuable insights into particle–laden flows and improve the efficiency of industrial processes. It is not fruitful to use direct numerical simulations in this situation. Instead Computational fluid dynamics (CFD) calculations can facilitate such improvements. CFD calculations require models for particle–laden flow. Models describing particle–laden turbulent flows can be roughly divided into two groups, the two–fluid (or Eulerian–Eulerian approach) [Drew (1983)], and the number–density based Lagrangian–Eulerian approach [Williams (1958); Subramaniam (2002, 2003)]. Both approaches are a statistical description for particle–laden turbulent flows.

In the Eulerian–Eulerian (EE) approach, both phases are treated as continua and flow quantities such as the velocity in each phase are averaged, and these averaged quantities are used to describe the characteristics of the carrier and dispersed–phase flow fields. This approach leads to unclosed terms representing the interaction between the phases. Once these terms are modeled to close the equation system, the EE approach can be used in computational fluid dynamics (CFD) calculations of multiphase flow.

In the Lagrangian–Eulerian (LE) approach, although the continuum description of the fluid phase is generally assumed to be identical to that in the EE representation, the particle phase is treated as composed of discrete objects in the system. The fundamental description of the dispersed phase by means of the droplet–distribution function (ddf) was introduced by Williams (1958) which forms the basis for the LE approach. Subramaniam (2000, 2001) established a firm mathematical base for the LE approach by using the theory of stochastic point processes.

The advantage of using the LE approach is the ability to easily vary the physical properties associated with individual particles (e.g., size or density). Moreover, insight into the unclosed terms in the governing equations for mean mass, momentum and TKE in the EE approach can be gained from the corresponding unclosed terms in the LE approach. The primary drawback is the computational effort required to track a large number of particles in the Lagrangian–Eulerian approach. Therefore, the EE approach is the more practical approach for simulating large-scale particle–laden flow processes.

The EE approach requires sophisticated modeling in order to describe the variation of turbulence modulation with particle Stokes number and mass loading. The goal of this research is to carefully examine the unclosed terms, in particular, the interphase TKE transfer and the dissipation rate, in Eulerian–Eulerian models for particle–laden turbulent flows, and improve the understanding and models for the these unclosed terms.

1.2 Research Approach

For particle–laden turbulent flows, the unclosed terms that are related to the interphase transfer of physical quantities, such as the interphase momentum and TKE transfer, put challenges on the mathematical modeling of gas–solid turbulent flows. To close these terms and obtain a useful model for engineering applications, one has to resort to results from experiments or a numerical simulation database where the unclosed terms are quantified. Experiments can give a "realistic" observation of particle–laden turbulent flows. Simple experiments without influence of gravity and flow inhomogeneities can usually give more insight into the behavior of unclosed terms in the governing equations for particle–laden turbulent flows. However, quantitative information on the unclosed terms is usually difficult to obtain from the experiments.

Direct numerical simulations (DNS) offer an alternative means of investigating particle–laden turbulent flow. The dataset from direct numerical simulations that are useful or pertinent to the modeling of unclosed terms in Eulerian–Eulerian models can be used to validate the EE models used in CFD calculations for multiphase turbulent flows. The numerical schemes

used in DNS can be categorized into those that resolve the flow around each particle [2] and those that do not. For the DNS studies that do not resolve the flow around each particle, the point–particle approximation is usually used with assumptions that the particle size is smaller than the Kolmogorov length scale of the fluid phase turbulence. In this approach, the velocity and location of particles are evolved through the particle velocity evolution equation proposed by Maxey and Riley (1983), while the fluid phase is solved using Navier–Stokes equation with kernel averaging performed to interpolate the interphase momentum transfer to the fluid momentum equations (two–way coupling). Since particles are modeled as point force in the flow field and the boundary layer around each particle is not fully solved, the interphase momentum and energy transfer are usually modeled in most point–particle DNS [Sundaram and Collins (1999)]. The numerical schemes developed for "true" DNS are discrete time immersed boundary method [Yusof (1996)], Lattice–Boltzmann method [Ten Cate et al. (2004)], fictitious domain method [Glowinski et al. (2001)] and arbitrary Lagrangian–Eulerian technique [Hu et al (2001)]. These methods involve minimum modeling in solving flow past rigid bodies. Lubrication forces are introduced when particles approach each other or collide.

For "true" DNS, the no-slip and no-penetration boundary conditions are imposed on the surface of each particle, while the point–particle DNS uses empirical forms of the hydrodynamic forces for the motions of rigid particles. Recent experimental results of particle–laden homogeneous turbulence [Hwang and Eaton (2006a)] suggest that point–particle DNS cannot capture the increased dissipation rate around particles which is important for the turbulence attenuation in particle–laden turbulent flows. These different DNS techniques for particle–laden turbulence require consistent definitions for the unclosed terms in "true" DNS, point–particle DNS and Eulerian–Eulerian models, which in turn lead us to the mathematical constraint on the terms in the governing equations for the evolution of the second-moment of velocity for particle–laden turbulent flow. In this work, the consistent mathematical modeling of interphase TKE transfer is derived.

The Eulerian–Eulerian models with unclosed terms modeled can be used in the CFD calcu-

[2] In the rest of the work, we refer DNS with flow around each particle resolved as "true" DNS.

lation for multiphase turbulent flows, which is useful for the design and scale–up of circulating fluidized combustors and coal gasifiers, etc. These CFD simulations can be further improved if the turbulence model reproduces important physical phenomena such as turbulence modification with variation of particle Stokes numbers. Therefore, the model should be validated in canonical particle–laden turbulent flow problems. In this research model validation is performed by using Direct Numerical Simulation (DNS) data for particle–laden homogeneous turbulence [Sundaram and Collins (1999)] and homogeneous shear flows [Ahmed and Elghobashi (2000)].

The techniques developed for "true" DNS, such as discrete time immersed boundary method, combined with the latest parallel algorithm, can be used to simulate gas–solid turbulent flows with no–slip boundary conditions solved on each particle. One can use the "true" DNS dataset to validate the model parameters. However the "true" DNS for particle–laden turbulence is still a difficult problem to solve today. One reason is limited computational power. In this research, we will focus on homogeneous turbulence past a random array of spheres where the primary interest is to investigate influence of the particle random configuration on fluid phase turbulence. The free stream turbulence is found to destabilize the wake structure and enhance the vortex shedding from stationary particles. In the problem of homogeneous turbulence past stationary random spheres, one can probe the effects of inter–particle spacing on fluid phase turbulence attenuation, which will not be obvious in case of spheres moving with the surrounding turbulence. Moreover, with this test problem we avoid the modeling of sphere collisions and the introduction of the lubrication forces into the system when spheres come close.

The contribution of this work is summarized as follows:

i) A multiscale interaction time scale originally proposed by Pai and Subramaniam (2006) is applied in the Eulerian–Eulerian models and validated in two canonical problems of particle-laden turbulent flow.

ii) A new multiphase turbulence model (EEM) is proposed in this work, and validated in decaying homogeneous particle-laden turbulent flow and homogeneous particle-laden shear flow.

iii) A mathematical constraint for interphase TKE transfer term in EE models of particle–laden turbulent is derived for homogeneous particle-laden turbulent flows with zero mean slip velocity. This principle is then extended to the non-zero mean slip velocity case.

iv) A "true" DNS simulation using the immersed boundary method is built on a legacy code from Yusof (1996). In this work, upstream homogeneous turbulence is introduced in the immersed boundary method.

v) The immersed boundary method is parallelized using the domain decomposition, and the performance of the parallel algorithm is studied. The grid convergence study is enabled due to the parallel immersed boundary method developed in this work.

vi) The DNS study of turbulent flow past a fixed bed of spheres reveals that the particle clusters enhance fluid phase turbulence. The spectra of fluid phase TKE and the redistribution of Reynolds stress are examined in detail.

1.3 Outline of Thesis

In Chapter 2, the Eulerian–Eulerian formulation for two–phase turbulent flow is presented. Existing multiphase turbulence models are then discussed. A general survey of the direct numerical simulation methods for particle–laden turbulence is also presented in Chapter 2. Chapter 3 discusses a new multiscale turbulence model for dilute gas-particle turbulent flows. A mathematical constraint on the interphase TKE transfer term in EE models of particle–laden turbulent flows is derived in Chapter 4, and its implication for multiphase turbulence models and the point–particle DNS is discussed. Chapter 5 describes the numerical scheme of the discrete-time immersed boundary method. In order to study the modulation of turbulence by random arrangements of spheres, the discrete-time immersed boundary method is parallelized using the domain decomposition method and the parallel tri-diagonal matrix solver in Chapter 6. The DNS study of upstream turbulence past fixed beds of spheres is presented in Chapter 7. Suggestions for future work are discussed in Chapter 8.

CHAPTER 2. LITERATURE REVIEW

In this chapter, the Eulerian–Eulerian formulation for particle–laden turbulent flows is shown in Section 2.1 and several popular multiphase turbulence models are discussed in Section 2.2. A general survey of direct numerical simulations for particle–laden turbulence is shown in Section 2.3.

2.1 Eulerian–Eulerian Formulation for Two–phase Flows

The Eulerian–Eulerian (EE), or two-fluid, approach is one of the statistical models for two-phase flow that is used in CFD calculations of multiphase flows. There are several ways of defining averaged equations in the Eulerian–Eulerian approach. One may use temporal or spatial averaging, where time averaging is strictly applicable to only statistically stationary flows, and volume averaging is strictly applicable only to statistically homogeneous flows. Drew's formulation [Drew (1983); Drew and Passman (1999)] of the two–phase flow problem uses the ensemble-averaging which enables this formulation to describe statistically unsteady, inhomogeneous problems.

In Drew's formulation, an indicator function $I_\beta(\mathbf{x}, t)$ is used to denote the βth phase, which is unity if the location $\mathbf{x}$ in the physical space is occupied by phase β at time t, and zero otherwise. It is assumed that (i) the density difference between the two phases is sufficiently large so that the density field can be used to distinguish between the two phases, and (ii) the characteristic length scale of the interface over which this density change occurs is so small that in a continuum description the density changes discontinuously at the interface. The second

assumption implies that in two-phase flows the phase indicator functions satisfy the relation

$$\sum_{\beta=1}^{2} I_\beta(\mathbf{x},t) = 1, \tag{2.1}$$

for all $(\mathbf{x},t)$. The phase index is β and the particle phase is referred to as $\beta = p$ and the fluid phase as $\beta = f$.

The event associated with the random-field representation is $E_0^{(\beta)} = [I_\beta(\mathbf{x},t) = 1]$. The probability of this event defines a probability field $\alpha_\beta(\mathbf{x},t)$:

$$\alpha_\beta(\mathbf{x},t) \equiv P[I_\beta(\mathbf{x},t) = 1]. \tag{2.2}$$

For two-phase flow system, α_β satisfies the relation

$$\sum_{\beta=1}^{2} \alpha_\beta(\mathbf{x},t) = 1. \tag{2.3}$$

In the Eulerian–Eulerian formulation for two-phase flow field, a phasic average is used to describe the two–phase flow [Drew (1983); Drew and Passman (1999)]. The phasic average is a conditional average, which is conditional on the event $E_0^{(\beta)}$, i.e., on the presence of phase β at that space–time location $(\mathbf{x},t)$. In particular, the mean density and velocity field *conditional* on the presence of phase β is used in the Eulerian–Eulerian formulation.

The mean velocity field for phase β can be defined in terms of conditional *density-weighted* average [1]:

$$\tilde{U}_k^{(\beta)} \equiv \frac{\langle \rho I_\beta U_k \rangle}{\langle \rho I_\beta \rangle}. \tag{2.4}$$

These *density-weighted* averages are the most convenient description of the mean velocity in mean momentum equations. The mean velocity conditioned on phase β without density-weighting is defined as:

$$U_k^{(\beta)} \equiv \frac{\langle I_\beta U_k \rangle}{\langle I_\beta \rangle}. \tag{2.5}$$

For the constant density two-phase flows ($\langle \rho | I_\beta = 1 \rangle = \rho_\beta$), the conditional *density-weighted* mean velocity is identical to the unweighted conditional mean velocity:

$$\tilde{U}_k^{(\beta)} \equiv \frac{\langle \rho I_\beta U_k \rangle}{\langle \rho I_\beta \rangle} = \frac{\langle I_\beta U_k \rangle}{\langle I_\beta \rangle} \equiv U_k^{(\beta)}. \tag{2.6}$$

[1] The notation for mean velocity $\tilde{U}_k^{(\beta)}$ is denoted as $U_{\beta,i}$ in Chapter 3.

The mean mass and momentum governing equations are derived by multiplying the standard Navier-Stokes equations with the indicator function $I_\beta(\mathbf{x}, t)$ and taking expectations of the resulting equations.

Mean Mass Conservation

The mean mass conservation in each phase ($\beta = f, p$) is:

$$\frac{\partial}{\partial t}[\alpha_\beta \rho_\beta] + \frac{\partial}{\partial x_k}[\alpha_\beta \rho_\beta \left\langle \tilde{U}_k^{(\beta)} \right\rangle] = \left\langle S_\rho^{(\beta)} \right\rangle . \tag{2.7}$$

where the source term on the RS of Eq. 2.7 is given by

$$\left\langle S_\rho^{(\beta)} \right\rangle = \left\langle \rho \left(U_i - U_i^{(I)} \right) \frac{\partial I_\beta}{\partial x_i} \right\rangle \tag{2.8}$$

and $U_i^{(I)}$ is the velocity of the interface.

Taking the expectations of the instantaneous mass conservation equation, and summing over both phases gives the constraint

$$\left\langle S_\rho^{(f)} \right\rangle = - \left\langle S_\rho^{(p)} \right\rangle . \tag{2.9}$$

For zero interphase mass transfer, such as gas-solid flows, the source term $\left\langle S_\rho^{(\beta)} \right\rangle$ is zero.

Mean Momentum Equation

The mean momentum conservation in each phase ($\beta = f, p$) is:

$$\begin{aligned} &\frac{\partial}{\partial t}[\alpha_\beta \rho_\beta \left\langle \tilde{U}_j^{(\beta)} \right\rangle] + \frac{\partial}{\partial x_k}[\alpha_\beta \rho_\beta \left\langle \tilde{U}_j^{(\beta)} \right\rangle \left\langle \tilde{U}_k^{(\beta)} \right\rangle] \\ &= -\frac{\partial}{\partial x_i}[\alpha_\beta \rho_\beta \tilde{R}_{ij}^{(\beta)}] + \frac{\partial}{\partial x_i} \left\langle I_\beta \tau_{ij} \right\rangle + \left\langle I_\beta \rho b_j \right\rangle + \left\langle M_j^{(\beta)} \right\rangle \end{aligned} \tag{2.10}$$

where $\tilde{R}_{ij}^{(\beta)}$ is the Reynolds stress in phase β, the definition of which is given in Eq. 2.14; $\langle I_\beta \tau_{ij} \rangle$ is the expected stress tensor weighted by the phase indicator function; $\langle I_\beta \rho b_j \rangle$ is the expected body force weighted by the phase indicator function, and $\left\langle M_j^{(\beta)} \right\rangle$ is the interphase momentum transfer source in β phase,

$$\left\langle M_j^{(\beta)} \right\rangle = \left\langle \rho U_j \left(U_i - U_i^{(I)} \right) \frac{\partial I_\beta}{\partial x_i} - \tau_{ij} \frac{\partial I_\beta}{\partial x_i} \right\rangle . \tag{2.11}$$

The interphase momentum transfer source (Eq. 2.11) has two parts: the first term represents the contributions from the interphase mass transfer, while the second term is due to the fact that the interface can support a stress difference. For gas-solid two-phase flows, the first term in $\left\langle M_j^{(f)} \right\rangle$ is zero, and the second term is required for closure through modeling. The interphase momentum source is subjected to the following constraint

$$\left\langle M_j^{(f)} \right\rangle = -\left\langle M_j^{(p)} \right\rangle + \left\langle M^{(I)} \right\rangle \tag{2.12}$$

where $\left\langle M^{(I)} \right\rangle$ is the average momentum associated with the interface. For gas-solid two-phase flows, the average momentum associated with the interface $\left\langle M^{(I)} \right\rangle$ is zero.

Second Moment Equations

The fluctuating velocity in phase β is defined as

$$u_i''^{(\beta)} \equiv U_i - \left\langle \tilde{U}_i^{(\beta)} \right\rangle \tag{2.13}$$

where U_i is the instantaneous velocity field, and $\left\langle \tilde{U}_i^{(\beta)} \right\rangle$ is the conditional *density-weighted* average velocity for phase β. Based on the definition of (density-weighted) fluctuating velocity, the Reynolds stress $\tilde{R}_{ij}^{(\beta)}$ is defined as

$$\tilde{R}_{ij}^{(\beta)} \equiv \frac{\left\langle I_\beta \rho u_i''^{(\beta)} u_j''^{(\beta)} \right\rangle}{\langle I_\beta \rho \rangle} \tag{2.14}$$

For gas-solid two-phase flows, without interphase mass transfer, the evolution equation of the Reynolds stress $\tilde{R}_{ij}^{(\beta)}$ in phase β is

$$\begin{aligned}
&\langle I_\beta \rho \rangle \frac{\tilde{D}_\beta}{\tilde{D}_\beta t} \tilde{R}_{ij}^{(\beta)} + \frac{\partial}{\partial x_k} \left\langle I_\beta \rho u_i''^{(\beta)} u_j''^{(\beta)} u_k''^{(\beta)} \right\rangle = \\
&- \left\{ \left\langle I_\beta \rho u_i''^{(\beta)} u_k''^{(\beta)} \right\rangle \frac{\partial \left\langle \tilde{U}_j^{(\beta)} \right\rangle}{\partial x_k} \right\} - \left\{ \left\langle I_\beta \rho u_j''^{(\beta)} u_k''^{(\beta)} \right\rangle \frac{\partial \left\langle \tilde{U}_i^{(\beta)} \right\rangle}{\partial x_k} \right\} \\
&+ \left\langle u_i''^{(\beta)} \frac{\partial (I_\beta \tau_{kj})}{\partial x_k} \right\rangle + \left\langle u_j''^{(\beta)} \frac{\partial (I_\beta \tau_{ki})}{\partial x_k} \right\rangle \\
&+ \left\langle u_i''^{(\beta)} S_{Mj}^{(\beta)} \right\rangle + \left\langle u_j''^{(\beta)} S_{Mi}^{(\beta)} \right\rangle
\end{aligned} \tag{2.15}$$

where the terms on the left hand side are: (i) the material derivative of the Reynolds stress in phase β with the density-weighted mean velocity in phase β, (ii) the triple velocity correlation

term. The terms on the right hand side are: (iii)-(iv) production of Reynolds stress due to the mean velocity gradients, (v)-(vi) fluctuating velocity-stress gradient correlation, (vii)-(viii) fluctuating velocity-interfacial momentum transfer correlation.

The kinetic energy k_f and k_p in the fluid and particle (or dispersed) phase respectively, are the half of the trace of the Reynolds stress tensor. For gas-solid two–phase flows, if the thermodynamic density is constant in each phase and there is no interphase mass transfer, the evolution equation for kinetic energy in phase β is

$$\alpha_\beta \rho_\beta \frac{\partial k_\beta}{\partial t} + \alpha_\beta \rho_\beta \tilde{U}_k^{(\beta)} \frac{\partial k_\beta}{\partial x_k} + \frac{1}{2} \alpha_\beta \rho_\beta \frac{\partial}{\partial x_k} \left\langle u_i''^{(\beta)} u_i''^{(\beta)} u_k''^{(\beta)} \right\rangle =$$
$$- \left\{ \left\langle I_\beta \rho u_i''^{(\beta)} u_k''^{(\beta)} \right\rangle \frac{\partial \left\langle \tilde{U}_i^{(\beta)} \right\rangle}{\partial x_k} \right\} + \left\langle u_i''^{(\beta)} \frac{\partial (I_\beta \tau_{ki})}{\partial x_k} \right\rangle + \left\langle u_i''^{(\beta)} M_i^{(\beta)} \right\rangle, \qquad (2.16)$$

The third term on the left hand side is the triple velocity correlation term. The terms on the right hand side are

(i) the production of TKE in phase β due to the mean velocity gradient;

(ii) the fluctuating velocity–stress gradient and fluctuating velocity–pressure correlation, where the contribution from pressure correlation is neglected, and this term is modeled as the dissipation in the phase β;

(iii) the fluctuating velocity–interfacial momentum transfer correlation.

The third term is not in the second moment equation for the single phase turbulence. It is this term that puts the challenge on modeling rather than the other two terms on right side of Eq. 2.16.

2.2 Eulerian-Eulerian Multiphase Turbulence Models

We briefly review several multiphase turbulence models in this section, which are all based on the Eulerian–Eulerian approach.

Elghobashi and Abou-Arab (1983) developed a two-equation turbulence model, which describes the conservation of turbulent kinetic energy (TKE) and dissipation rate in the fluid phase based on the volume averaging method. This two phase k-ε model was validated by

comparing with results from particle-laden jet flow [Elghobashi et al. (1984)] and jet flows laden with vaporizing droplets]Mostafa and Elghobashi (1985)]. The volume averaging approach is used in this model, and it could cause problems if this model is used in a spatially inhomogeneous turbulent flow.

Ahmadi and Ma (1990) used the ensemble-averaging method to derive the evolution equation for TKE in the carrier and dispersed phases. The transport equation for dissipation rate in fluid phase is the standard k-ε model for single phase turbulence. Ahmadi's model contains the specification of model constants for dilute two–phase flows and dense granular flows as special limiting cases. Validation of this model has been reported for simple shear flow of a dense mixture [Ma and Ahmadi (1990)] ($\alpha_p > 0.1$).

A four-equation model proposed by Simonin (1996b,a) has been tested by Sofiane (2002) and compared with experimental results for the turbulent gas-solid flows in a vertical pipe [Sinclair and Jackson (1989)], and in a vertical riser [Bolio et al. (1995)]. Based on this model, a single phase k-ε model is added in MFIX (**M**ultiphase **F**low with **I**nterphase e**X**changes) kernel and a turbulent pipe flow test case is included in MFIX.

2.3 Direct Numerical Simulation for Particle–laden Turbulence

Many researchers [Elghobashi and Truesdell (1993); Boivin et al. (1998); Sundaram and Collins (1999); Ahmed and Elghobashi (2000, 2001); Mashayek and Taulbee, (2001); Mashayek and Taulbee (2002); Ferrante and Elghobashi (2003)] have performed DNS studies for particle–laden turbulence, and the flow configurations in these studies include homogeneous turbulence (decaying and stationary), homogeneous shear flow, and plane–strain turbulence.

Elghobashi performed direct numerical simulation of turbulence modulation in particle–laden decaying homogeneous turbulence [Elghobashi and Truesdell (1993)] and homogeneous shear [Ahmed and Elghobashi (2000)]. In both of these studies, the particle size is less than the Kolmogorov length scale η with the Stokes number larger than 1. The modulation of fluid phase TKE with respect to different particle Stokes numbers and mass loading is reported. In the DNS of particle–laden decaying homogeneous turbulence [Elghobashi and Truesdell (1993)],

the rate of energy transfer between phases at wavenumber κ is studied in the Fourier space. This study shows that particles transfer their momentum to the high wavenumber motion of the carrier fluid, and hence increase the energy at higher wavenumber. This increase of energy at higher wavenumber κ is accompanied by an increase of the viscous dissipation rate, and also the increase of the energy transfer from energy-containing range to dissipation range.

These studies reveal a picture of multiscale interaction in particle–laden turbulent flow. Even particles are smaller than the Kolmogorov length scale, the fluid–particle interaction still affects the large scale motions in the carrier phase turbulence through the energy cascade. Although the spectral distribution of the rate of energy transfer between phases at wavenumber κ helps to understand the multiscale interaction of particle–laden turbulence, the spectral data are not easy to use in the model validations.

Boivin et al. (1998) performed point–particle DNS for particle–laden stationary homogeneous turbulence. The particle size is also less than the Kolmogorov length scale η and with $St > 1$. Reynolds number is up to approximately 1.5 for the largest particle size. In this study, modulation of TKE, energy spectrum and dissipation rate with different mass loading ϕ and particle Stokes number St are compared with the unladen homogeneous turbulence. To study the modulation of turbulence due to the momentum transfer between phases, the interphase TKE transfer term Π_{k_f} and Π_{k_p} uses k_{fp} the fluid–particle velocity covariance, which is a pseudo–flow quantity.

DNS study by Sundaram and Collins (1999) studied the particle–laden decaying homogeneous turbulence. The particle parameters are of the similar range as those in Boivin et al. (1998). Different from other DNS studies, dynamical equations for the kinetic energy in fluid and particle phases, and the total energy of the system are derived. The mechanism for the dissipation of total energy of the system is described as two aspects:

1. viscous dissipation occurring throughout the continuous fluid phase (ϕ_v);

2. and the losses due to the drag at the particle interface(ϕ_p). The particle are dissipative to the total energy of the system.

The budget of ϕ_v and ϕ_p is reported in this study, which can be used to validate the multiphase turbulence models in the canonical problem of particle–laden homogeneous turbulence.

The direct numerical study with point–particle approximation reveals the attenuation of fluid phase turbulence with variation of particle inertia, mass loading ratio, and provides data for validation of the multiphase turbulence models. Particle image velocimetry (PIV) experiments by Hwang and Eaton (2006a,b) of homogeneous particle–laden turbulence reveal higher turbulent kinetic energy reduction than that predicted by DNS [Elghobashi and Truesdell (1993); Boivin et al. (1998); Squires and Eaton (1990)]. It is noted that computational restrictions of DNS make it difficult to simulate the same experimental conditions, hence direct comparison is difficult. However, the discrepancy in the attenuation of fluid–phase turbulence indicates the point–particle approximation used in these simulations may not capture all the physics [Hwang and Eaton (2006a,b)].

Lattice Boltzmann simulation of turbulent solid-liquid suspensions is studied by Ten Cate et al. (2004), where the exact boundary conditions are imposed on particles. This is quite different from the physical system focused in this report, where the density ratio between particle and fluid phase is of order one and the solid volume fraction is around 2%–10% in solid-liquid suspensions. In this work, authors compare the modulation of TKE with that reported in point–particle DNS [Elghobashi and Truesdell (1993); Boivin et al. (1998); Sundaram and Collins (1999)]. It is found that the TKE reduction rates at mass loading ratio 10% in Ten Cate et al. (2004) are comparable to that reported in point–particle DNS by Boivin et al. (1998). This implies that although point–particle DNS lacks the details of the small-scale fluid motion as present in lattice Boltzmann simulation, the large-scale motions captured in both simulation approaches are consistent [Ten Cate et al. (2004)].

CHAPTER 3. IMPROVED MULTISCALE TURBULENCE MODEL FOR PARTICLE–LADEN TURBULENT FLOW

The multiscale interaction mechanism revealed by DNS motivates the development of the new Eulerian–Eulerian model for particle–laden turbulence proposed in this chapter[1]. The DNS data of TKE evolution for particle–laden decaying homogeneous turbulence [Sundaram and Collins (1999)] and homogeneous shear [Ahmed and Elghobashi (2000)] is used to validate Eulerian–Eulerian models in this study.

The outline of this chapter is shown as follows:

(1) perform a comparative assessment of model predictions with direct numerical simulation data for a canonical turbulent particle–laden flow;

(2) identify modeling criteria based on this comparative assessment;

(3) propose a new multiphase turbulence model for dilute particle–laden turbulent flows, and derive the transport equations for the Reynolds stress tensor in the fluid and particle phases;

(4) validate this new multiphase turbulence model in canonical turbulent particle–laden flow problems, and ensure that this model satisfies the modeling criteria identified in the comparative study.

[1]This chapter is based on Xu and Subramaniam (2006).

3.1 Comparative Assessment of Simonin and Ahmadi's Multiphase Turbulence Models

An important limiting case of turbulent multiphase flows is statistically homogeneous particle–laden turbulent flow evolving in a zero–gravity environment [Squires and Eaton (1990)]. The principal findings from direct numerical simulations of this flow by Sundaram and Collins (1999), and the results from a comparative assessment of two multiphase turbulence models, are summarized in this section.

If gravity is absent and the mean velocity fields are homogeneous, the mean pressure gradient is zero and the mean momentum equation system results in the trivial solution of zero mean velocity in each phase, which implies a zero mean slip velocity [Subramaniam (2002)]. If the flow field is initialized with zero mean velocity in both phases, the mean velocities will remain zero. In this case, it is easy to study the evolution of second-moments of fluctuating velocity solely influenced by interphase TKE transfer and viscous dissipation (without effects of mean velocity gradients).

In this DNS study [Sundaram and Collins (1999)], rigid, spherical solid particles evolve in freely decaying homogeneous turbulent flow. There is no interphase mass transfer. The flow is dilute, with particle density much larger than fluid density ($\rho_p/\rho_f \approx 10^3$). The particle size is in the sub-Kolmogorov range ($\eta = 0.035$ and $d/\eta < 1$, where d is the mean particle diameter), but the particles are large enough to ignore Brownian motion. Hence, a linear drag law can be applied to each particle in the momentum equations.

The boundary layer around each particle is neglected, and particles are viewed as point particles in the flow field[2]. Particle collisions are assumed to be elastic, so collisions conserve particle kinetic energy. Since the particle volume fraction is quite low, the influence of the particles on the fluid phase continuity equation is neglected, but the effects on fluid momentum are still taken into account.

The predictions from DNS show that the energy in both phases decreases monotonically

[2]However, kernel averaging is performed to interpolate the interphase momentum transfer to the fluid momentum equation.

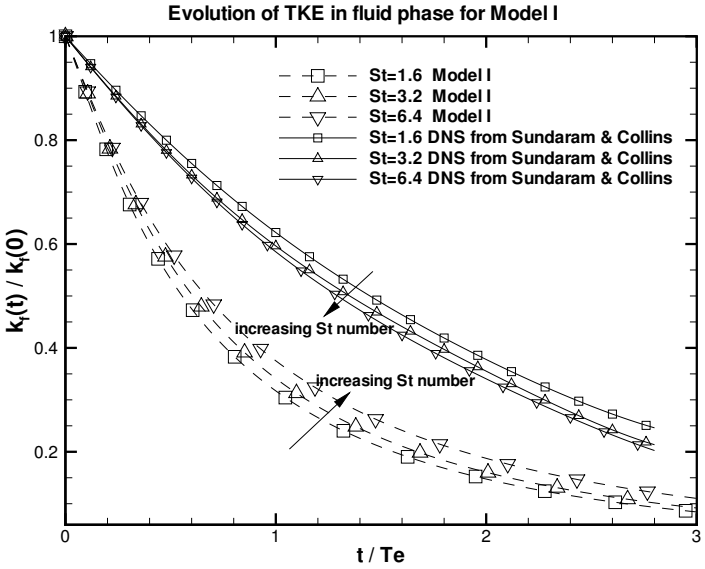

Figure 3.1 Evolution of TKE in fluid phase from Model I for decaying homogeneous particle–laden turbulent flow. Arrows in the figure indicate the direction of increasing particle Stokes number.

and the net effect of particles is to reduce fluid energy. An important non-dimensional quantity that characterizes the inertia of the solid particles is the Stokes number $St = \tau_p/\tau_f$, which is defined as the ratio of the characteristic particle momentum response time $\tau_p = (\rho_p/\rho_f)d^2/18\nu_f$ to a characteristic flow timescale τ_f. In Sundaram and Collins' DNS study [Sundaram and Collins (1999)], the characteristic flow timescale is chosen to be the Kolmogorov timescale $\tau_\eta = (\nu/\varepsilon)^{1/2}$, and therefore the Stokes number in this work is defined as $St \equiv \tau_p/\tau_\eta$. DNS results [Sundaram and Collins (1999)] show that the effect of the particles to reduce fluid energy grows with increasing particle Stokes number. The particle energy also decays monotonically in time and the decay rate increases with increasing particle Stokes number (for fixed mass loading). See the solid lines in Figures 3.1 and 3.2.

We now summarize the two multiphase turbulence models that are used to predict the decay of kinetic energy in the decaying homogeneous turbulence case described above. Hereafter, Simonin's model is referred to as Model I in this work, and Ahmadi's model is referred to as Model II.

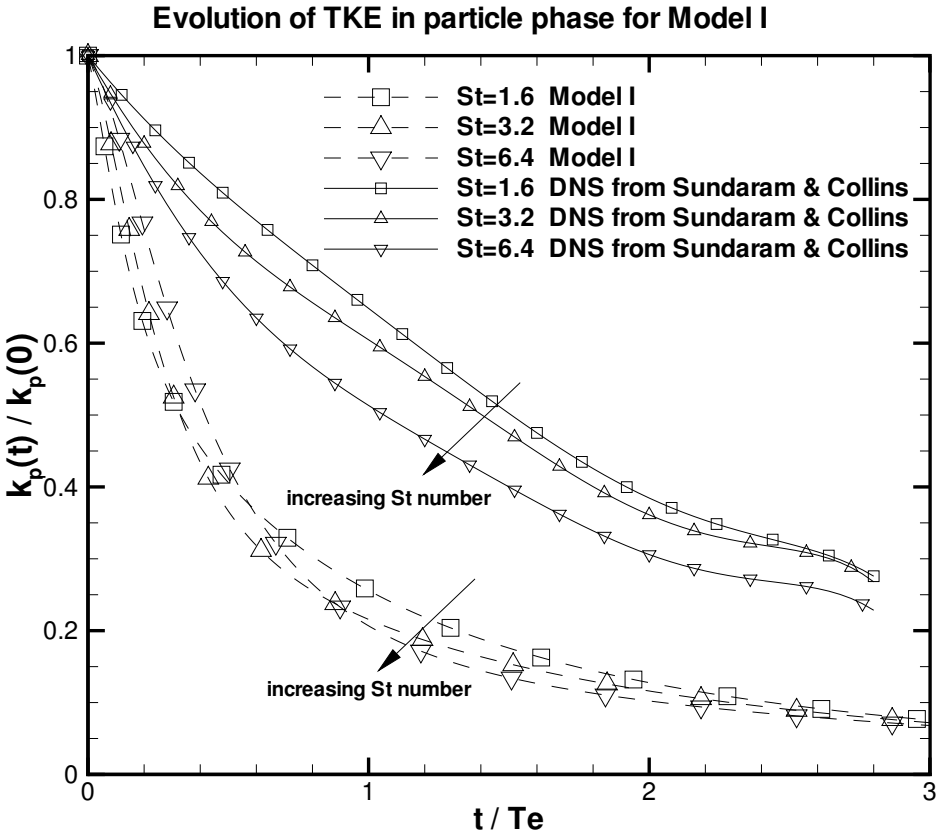

Figure 3.2 Evolution of TKE in particle phase from Model I for decaying homogeneous particle–laden turbulent flow.

3.1.1 Model I — Simonin's Model: Model Description and Results

For decaying homogeneous particle–laden turbulent flow, the simplified model equations for TKE and dissipation rate in the fluid phase from Model I [Simonin (1996b,a)] are:

$$\alpha_f \rho_f \frac{dk_f}{dt} = \Pi_{k_f} - \alpha_f \rho_f \varepsilon_f, \tag{3.1}$$

$$\alpha_f \rho_f \frac{d\varepsilon_f}{dt} = C_{\varepsilon,3} \frac{\varepsilon_f}{k_f} \Pi_{k_f} - \alpha_f \rho_f C_{\varepsilon,2} \frac{\varepsilon_f^2}{k_f}, \tag{3.2}$$

where $C_{\varepsilon,2} = 1.92$ and $C_{\varepsilon,3} = 1.2$. The particle phase influences the fluid phase TKE through the interphase TKE transfer term $\Pi_{k_f} = \alpha_p \rho_f F_D \left[k_{fp} - 2k_f\right]$, where F_D plays the role of an effective particle response frequency.

The model transport equation for TKE in particle phase simplifies to

$$\alpha_p \rho_p \frac{dk_p}{dt} = \Pi_{k_p} = -\alpha_p \rho_p \frac{1}{\tau_{12}^F}[2k_p - k_{fp}], \tag{3.3}$$

$$\alpha_p \rho_p \frac{dk_{fp}}{dt} = \Pi_{k_{fp}} - \alpha_p \rho_p \varepsilon_{fp}, \tag{3.4}$$

where k_{fp} is the covariance of fluid–particle velocity. The dissipation of particle energy in Eq. 3.3 is neglected because of the assumption of elastic collisions in the DNS study. The interphase TKE transfer term Π_{k_p} accounts for the influence of fluid phase turbulence on k_p. The time scale τ_{12}^F is the particle response time.

In the equation for fluid–particle covariance k_{fp}, the interphase $\Pi_{k_{fp}}$ transfer is modeled as

$$\Pi_{k_{fp}} = -\alpha_p \rho_p \frac{1}{\tau_{12}^F}[(1+\phi)k_{fp} - 2k_f - 2\phi k_p]$$

where $\phi = \alpha_p \rho_p / \alpha_f \rho_f$, is the mass loading. The term ε_{fp} accounts for the dissipation of k_{fp} due to viscous effects in the fluid phase and the loss of correlation by crossing–trajectory effects. This dissipation rate is modeled as $\varepsilon_{fp} = k_{fp}/\tau_{12}^t$, where τ_{12}^t is the time scale of the fluid turbulent motion viewed by the particles. The model specification for this time scale is

$$\tau_{12}^t = \tau_1^t \left[1 + c_\beta \xi_r^2\right]^{-1/2} \quad \text{where} \quad \xi_r = \frac{|\bar{V}_r|}{\sqrt{\frac{2}{3}k_f}}$$

where c_β varies with the angle between the mean particle velocity and the mean relative velocity. This angle is taken to be zero in the homogeneous turbulence case, resulting in $c_\beta = 0.45$. The time scale of the energetic turbulent eddies τ_1^t is

$$\tau_1^t = \frac{3}{2} C_\mu \frac{k_f}{\varepsilon_f}$$

where $C_\mu = 0.09$.

The effective particle response frequency F_D is given in terms of local mean particle Reynolds number Re_p:

$$F_D = \frac{3}{4}\frac{C_D}{\overline{d}}\langle|\overline{v}_r|\rangle_2, \quad \langle|\overline{v}_r|\rangle_2 = \sqrt{V_{r,i}V_{r,i} + \langle v'_{r,i}v'_{r,i}\rangle_2}$$

$$C_D = \frac{24}{Re_p}\left[1 + 0.15 {Re_p}^{0.687}\right]\alpha_f^{-1.7}, \quad \text{for} \quad Re_p < 1000$$

where the particle Reynolds number Re_p is defined as

$$Re_p = \frac{\alpha_f \langle |\overline{v}_r| \rangle_2 \overline{d}}{\nu_f}. \tag{3.5}$$

The averaging method $\langle \cdot \rangle_2$ is defined as the dispersed phase mass average in Model I. The average value of the local relative velocity between each particle and the surrounding fluid flow $V_{r,i}$ can be expressed as

$$V_{r,i} = [U_{p,i} - U_{f,i}] - V_{d,i} \qquad V_{d,i} = \langle \tilde{u}_{f,i} \rangle_2 - U_{f,i} = \langle u'_{f,i} \rangle_2 \tag{3.6}$$

where $U_{p,i}$ and $U_{f,i}$ are the mean velocity of each phase; the drifting velocity $V_{d,i}$ represents the correlation between the instantaneous distribution of particles and turbulent fluid motion on characteristic length scales which are large compared to the particle diameter. To apply Model I in this simple test case, some quantities need to be specified. One is $\langle |v|_r \rangle_2$, the magnitude of the averaged value of the local relative velocity between particles and the surrounding fluid flow. In Model I, $\langle |v_r| \rangle_2$ is defined as

$$\langle |v_r| \rangle_2 = \sqrt{V_{r,i} V_{r,i} + \langle v'_{r,i} v'_{r,i} \rangle_2}$$

where $V_{r,i}$ is the mean relative or slip velocity, which is zero in the homogeneous particle–laden decaying turbulent flow, and $v'_{r,i}$ needs to be modeled. In this study, the following approximation is used

$$v'_{r,i} \equiv \alpha_f \alpha_p \left(u'_f + u'_p \right)$$

where $u'_f = \sqrt{\frac{2}{3} k_f}$, $u'_p = \sqrt{\frac{2}{3} k_p}$.

Also in Model I, the fluid–particle velocity covariance k_{fp} needs to be initialized. If the fluid–particle velocity covariance is expressed as

$$k_{fp}(t) = \rho_{fp}(t) \cdot k_f^{1/2}(t) \cdot k_p^{1/2}(t) \tag{3.7}$$

then $\rho_{fp}(t)$ is a "fluid–particle" correlation coefficient, which should be bounded by 0 and 1 (based on the Cauchy-Schwarz inequality[3]). Using this definition, we can determine $k_{fp}(0)$ by

[3]Implementations of this model [Sofiane (2002)] do not impose the bounds on ρ_{fp}, and recommend specification of values up to 2 so as to improve the model predictions. In this work also, $\rho_{fp}(0) = 2.0$ is used.

setting $\rho_{fp}(0)$ values. The role of the quantity k_{fp}, which is really a single–point surrogate for the fluid–particle velocity covariance, is discussed in detail elsewhere [Xu (2004)]. It is argued that k_{fp} is not an independent flow variable in single–point closures of two-phase turbulent flows. This conclusion is consistent with the theoretical analysis presented in Sundaram and Collins (cf. Eq. 29 (c,d) on p. 113 in Sundaram and Collins (1999)).

The principal time scale in the model is τ_{12}^F, the particle response time, which is related to the inertial effects acting on the particles:

$$\tau_{12}^F = F_D^{-1} \frac{\rho_p}{\rho_f} \tag{3.8}$$

However, this time scale is based on the slip velocity $\langle|\bar{v}_r|\rangle_2$, which is defined on the basis of $u_f' \sim \sqrt{k_f}$ and $u_p' \sim \sqrt{k_p}$. Since the particle Reynolds number Re_p is based on $\langle|\bar{v}|\rangle_2$, and is approximately unity in this flow, the time scale τ_{12}^F can be further simplified as

$$\tau_{12}^F = \frac{4}{3} \frac{\bar{d}}{C_D \langle|\bar{v}_r|\rangle_2} \frac{\rho_p}{\rho_f} = \frac{4}{3} \frac{\bar{d}}{C_D Re_p \nu_f} \frac{\rho_p}{\rho_f} \approx \frac{\alpha_f \bar{d}^2}{18\nu_f} \frac{\rho_p}{\rho_f}.$$

Since $Re_p \approx 1$, the product of C_D and Re_p is approximately equal to 24. Hence, in this homogeneous turbulence, under the condition of all particles having Re_p approximately equal to 1, the particle response time is approximately constant during the TKE evolution.

The prediction from Model I is that TKE in the fluid phase decreases monotonically, but the net effect of particles to reduce fluid energy is found to *decrease* with increasing Stokes numbers, which is *opposite* to the DNS result (see Figure 3.1). The model predictions for fluid energy evolution also show a much steeper decay at the beginning than the DNS result. The same steep decay is also observed in the particle energy evolution, which is shown in Figure 3.2. The particle energy decays monotonically. The decay of particle energy is observed to increase with increasing particle Stokes numbers after $t/T_e = 0.8$, which is consistent with DNS data, but there is some cross–over at the beginning of evolution, as seen in Figure 3.2.

3.1.2 Model II — Ahmadi's Model: Model Description and Results

The evolution equations of TKE in fluid and particle phase from Model II [Ahmadi and Ma (1990); Ma and Ahmadi (1990)], simplified for decaying homogeneous particle–laden turbulent

flow are[4]:

$$\rho_f \alpha_f \frac{dk_f}{dt} = 2D_0 \left(k_p - ck_f\right) - \rho_f \alpha_f \varepsilon_f \tag{3.9}$$

$$\rho_p \alpha_p \frac{dk_p}{dt} = 2D_0 \left(ck_f - k_p\right). \tag{3.10}$$

The transport equation for the dissipation rate in the fluid phase is given by Ahmadi (1989), which is essentially the same as that in the standard k–ε model for single phase turbulence. For decaying homogeneous turbulence, the evolution equation for ε_f is:

$$\alpha_f \rho_f \frac{d\varepsilon_f}{dt} = -C_{\varepsilon,2} \frac{\varepsilon_f^2}{k_f}, \tag{3.11}$$

where $C_{\varepsilon,2} = 1.92$. Since particle collisions are elastic in the DNS test case, the dissipation rate of particle energy is taken to be zero in Model II.

The coefficient c is related to the ratio of the particle time scale $\rho_p \alpha_p / D_0$ to the macroscale Lagrangian turbulence time scale T_L,

$$c = \frac{1}{1 + \dfrac{\rho_p \alpha_p}{D_0 T_L}}, \quad T_L = \frac{0.165 k_f}{\varepsilon_f}.$$

The drag coefficient D_0 is given as

$$D_0 = \frac{18 \mu_f \alpha_p}{\bar{d}^2} \frac{\left[1 + 0.1 \left(Re_p\right)^{0.75}\right]}{\left(1 - \dfrac{\alpha_p}{\nu_m}\right)^{0.25\nu_m}} \tag{3.12}$$

where $\bar{d}$ is the mean particle diameter and model coefficient $\nu_m = 0.64356$. The particle Reynolds number Re_p is defined as

$$Re_p = \frac{\rho_f \bar{d} |U_{f,i} - U_{p,i}|}{\mu_f}.$$

where $U_{f,i}$ and $U_{p,i}$ are the i^{th} components of the mean velocity in the fluid and particle phase respectively.

In Model II the term $D_0/(\alpha_p \rho_p)$ represents a particle response frequency. The expression for this particle response frequency (cf. Eq. 3.12) can be further simplified because the particle

[4]In Model II [Ahmadi and Ma (1990); Ma and Ahmadi (1990)], the notation used to represent fluid and particle phase variables, and volume fraction is slightly different.

Reynolds number Re_p based on the mean slip velocity is zero in this case. In the limit of volumetrically dilute flow ($\alpha_p \ll 1$), the resulting simplified expression for the particle response frequency tends to its limiting value of the reciprocal of the particle response time:

$$\frac{D_0}{\alpha_p \rho_p} = \frac{18\nu_f}{d^2}\frac{\rho_f}{\rho_p}\frac{1}{\left(1-\frac{\alpha_p}{\nu_m}\right)^{0.25\nu_m}} \approx \frac{18\nu_f}{d^2}\frac{\rho_f}{\rho_p} \quad \text{for } \alpha_p \ll 1 \quad .$$

Figure 3.3 shows that the prediction from Model II shows satisfactory agreement with DNS results for the evolution of fluid energy, except for some quantitative difference after $t/T_e = 1.5$. The decay of k_f is not enough after $t/T_e = 1.5$. This is probably because the single phase turbulence model is used for the dissipation rate of fluid energy. The incorrect variation of fluid energy evolution with increasing particle Stokes numbers that was observed in Model I is not found in Model II. Model II predicts a very steep decay of particle energy at early time, and the quantitative discrepancy between model predictions and DNS data is quite large, as seen in Figure 3.4.

3.1.3 Summary of Model Results

It is obvious that the definition of the particle response time in Model I is almost the same as that in Model II under conditions of particle Reynolds number close to unity, and particle volume fraction far less than one. The particle response time is used as the timescale for interphase TKE transfer term in both these models, and the interphase TKE transfer plays the dominant role in the equation system of both models. We arrived at this conclusion based on the budget study of the equation systems of the two multiphase turbulence models, and the detailed budget analysis is shown in Xu (2004). Given the significant discrepancy between the TKE decay rate predicted by the models and that predicted by the DNS for different Stokes numbers, it is hypothesized that the particle response time is not the appropriate time scale for interphase TKE transfer.

The physical reason behind the incorrect behavior of k_f evolution with increasing particle Stokes number in Model I, and the anomalous steep decay of k_p at early time lies in the fact that the particle response time is the appropriate time scale for only a limited range of

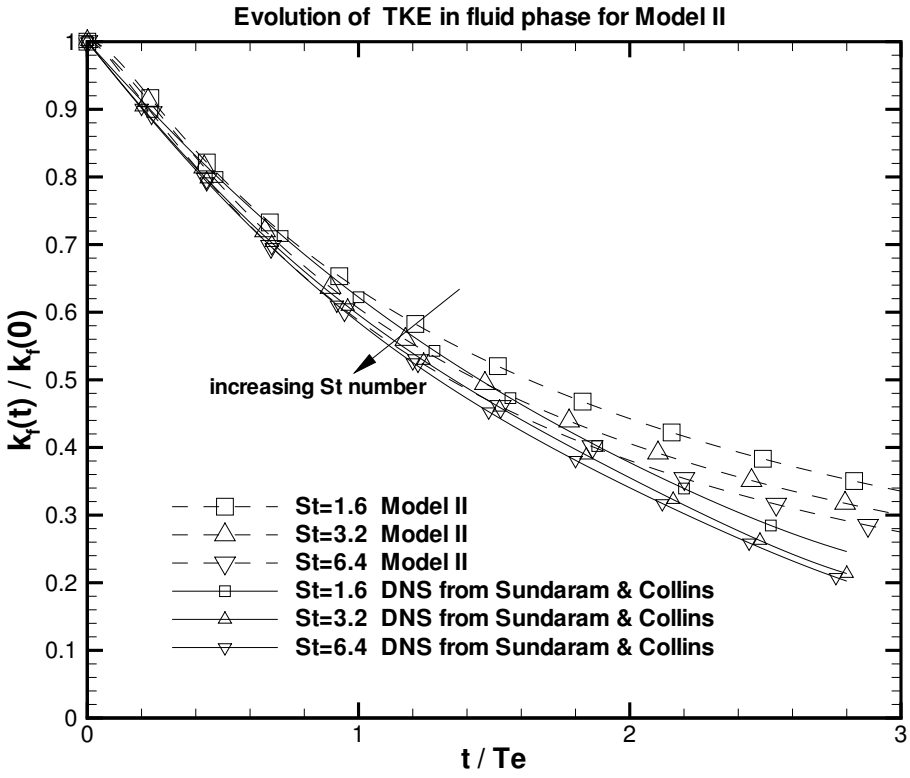

Figure 3.3 Evolution of TKE in fluid phase from Model II for decaying homogeneous particle–laden turbulent flow.

particle–eddy interactions. In reality, particle–turbulence interaction is a complex multiscale process. Even for a monodisperse gas–solid two–phase flow, particles interact with a range of eddies with different length and time scales. Furthermore, the particle response time and the Stokes number for each particle is different, since each particle has a different instantaneous velocity. The particle response time defined here can only represent the characteristic time scale of particles interacting with the eddies in the dissipation range.

In Eulerian–Eulerian models, all the quantities in the governing equations are averaged. Since the interphase TKE transfer represents the average interaction of all particles with the entire range of turbulent scales, the model for this term should somehow account for this complex multiscale interaction.

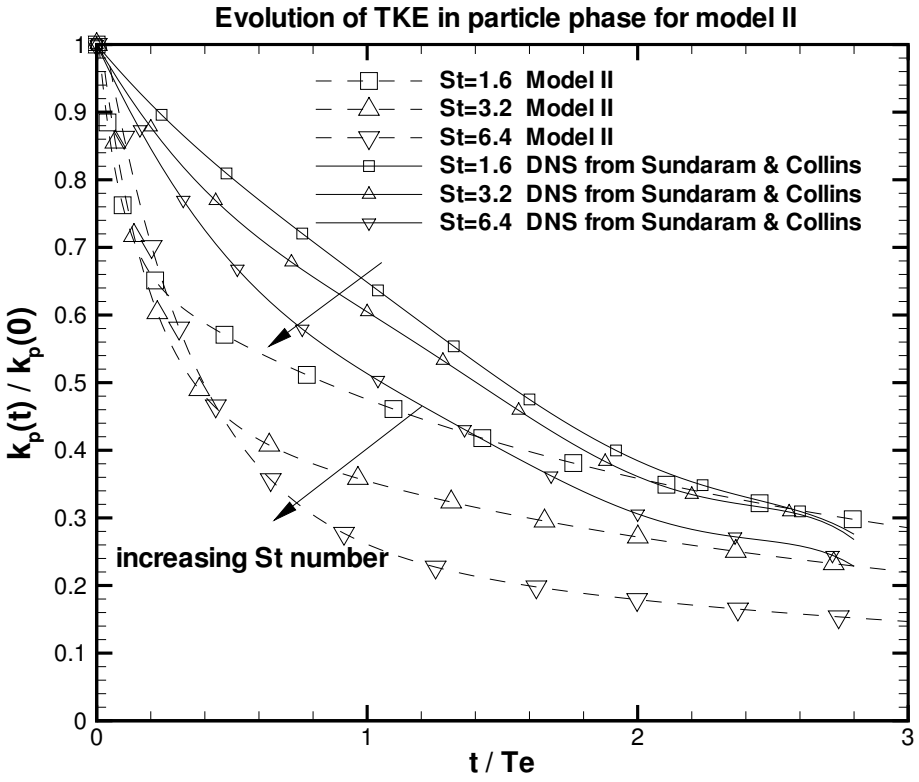

Figure 3.4 Evolution of TKE in particle phase from Model II for decaying homogeneous particle–laden turbulent flow.

3.2 Multiscale Interaction Model for Interphase TKE Transfer

Based on the discussion in the previous section, a new time scale is proposed to model the interphase TKE transfer. This new time scale is implemented in Model I and Model II, and it improves the performance of both models in decaying homogeneous particle–laden turbulent flow.

From the model testing in the previous section, it was noted that the incorrect variation of k_f with increasing particle Stokes numbers, and the steep decay of k_p that are found in the model results, need to be improved. In Model I and Model II, the complex particle–fluid interaction represented by the interphase TKE transfer terms is characterized by a single time scale, the particle response time τ_p, which needs further improvement. A multiscale interaction model was first proposed by Pai and Subramaniam (2004), to improve the multiphase turbulence model in KIVA [Amsden et al. (1989)], which is based on the Lagrangian–Eulerian

approach. An equivalent form of this multiscale interaction model is implemented in the Eulerian–Eulerian models discussed in this work, and this timescale improves the predictions from Model I and Model II.

One can define a particle Stokes number based on τ_l, a characteristic time scale for an eddy in the inertial sub–range of turbulence, as

$$St_l = \frac{\tau_p}{\tau_l}$$

where

$$\tau_l = \frac{l}{|\mathbf{u}_g'|} = \frac{|\mathbf{u}_g'|^2}{\varepsilon_f},$$

such that l is the characteristic length scale of the eddy, and $|\mathbf{u}_g'|$ is the characteristic eddy velocity in inertial subrange. Therefore, the particle Stokes number based on τ_l scales as

$$St_l \sim \frac{1}{|\mathbf{u}_g'|^2}.$$

For the EE implementation, the distribution of $\mathbf{u}_g'$ is assumed to be joint–normal for homogeneous turbulence. This means that energetic eddies can be associated with a small Stokes number and small fluctuations can be associated with a large Stokes number. Thus, there are different particle Stokes numbers St_l that correspond to eddy of different sizes l.

The hypothesis is that for $St_l < 1$, particles respond immediately to the flow. When particles are entrained in the eddies with $St_l < 1$, particles will basically follow the characteristic time scale of the eddies. As St_l approaches zero, particles follow the eddy turnover time τ.

For $St_l > 1$, the particle responds slowly to the flow. In this case, the characteristic size of the eddies is small and $|\mathbf{u}_g'|^2$ is also very small. Particles will not be entrained in these small eddies. The inertia of the particle plays an important role when particle interacts with small size eddies. Since the particle response time is a measure of the particle inertia, which depends on the density and the size of the particles, the particle follows its response time when $St_l > 1$.

For the case of zero–gravity homogeneous particle–laden turbulent flow, the fluctuating velocity in the fluid phase is assumed to be isotropic and joint–normal, and the probability density function for $Z = |\mathbf{u}_g'|$ is

$$f_Z(z) = \sqrt{\frac{2}{\pi}} \frac{1}{\sigma_f^3} z^2 e^{-z^2/2\sigma_f^2}$$

where z is the corresponding sample space variable of random variable Z, and σ_f is the standard deviation of $\mathbf{u}'_g$, which is $\sqrt{\frac{2}{3}k_f}$ for isotropic homogeneous turbulent flows. Figure 3.5 is a sketch of the probability density function of Z. The value of Z where $St_l = \tau_p/\tau_l = 1$ is of special significance, and it is denoted $|\mathbf{u}'_g|^*$. This transition value of $|\mathbf{u}'_g|^*$ divides the z-axis into two regions: $St_l < 1$ and $St_l > 1$.

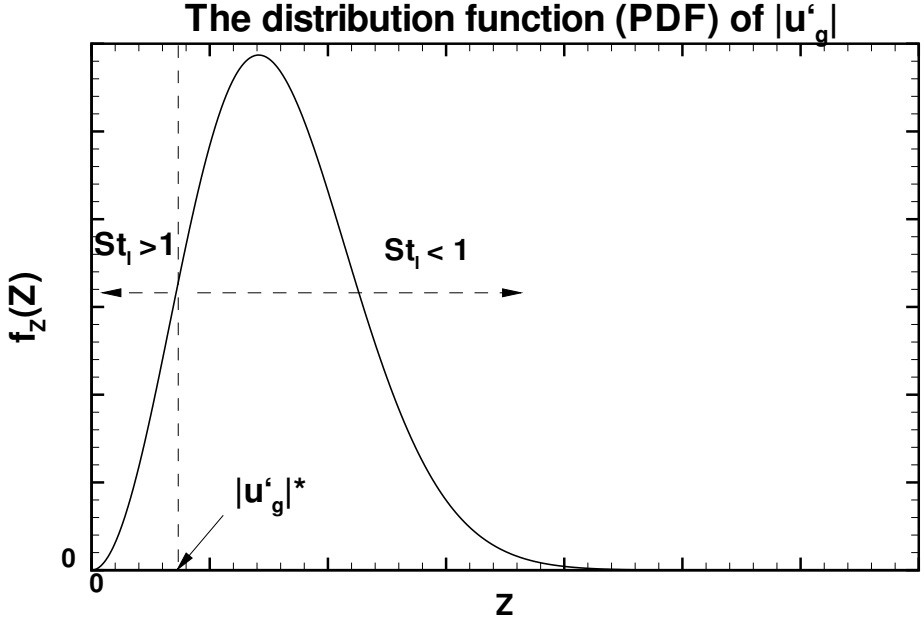

Figure 3.5 Sketch of the probability density function $Z = |\mathbf{u}'_g|$.

The interaction time τ_i is assumed to be a random variable, which is a prescribed function of $Z = |\mathbf{u}'_g|$. The mean interaction time $\langle \tau_i \rangle$ is obtained from the conditional mean $\langle \tau_i | Z = |\mathbf{u}'_g| \rangle$ by:

$$\langle \tau_i \rangle = \int_0^\infty \langle \tau_i | z \rangle \, f_Z(z) dz.$$

The conditional mean of τ_i is assumed to be of the following form:

$$\langle \tau_i | Z \rangle = \tau_p \qquad 0 < |\mathbf{u}'_g| < |\mathbf{u}'_g|^* \tag{3.13}$$

$$\langle \tau_i | Z \rangle = St_l \cdot (\tau_p - \tau) + \tau \qquad |\mathbf{u}'_g|^* < |\mathbf{u}'_g| < \infty. \tag{3.14}$$

The conditional mean $\langle \tau_i | Z \rangle$ in the range $|\mathbf{u}'_g|^* < |\mathbf{u}'_g| < \infty$ is simply modeled as a linear function of St_l. As $St_l \to 0$, $\langle \tau_i | Z \rangle$ is equal to the eddy turnover time τ and particles just

move with the eddies. When $St_l \geq 1$, particles respond slowly to the flow, and the particle response time τ_p is dominant here.

One can retrieve Model I and Model II from the expression of $\langle \tau_i \rangle$ by considering the limit of $|\mathbf{u}'_g|^* \to \infty$ and $\langle \tau_i \rangle_{|\mathbf{u}'_g|^* \to \infty} = \tau_p$, where τ_p is the particle response time. This means that particles respond to the flow at the particle response time scale for the entire range of $|\mathbf{u}'_g|$.

The mean of τ_i is defined as

$$\langle \tau_i \rangle = \int_0^{|\mathbf{u}'_g|^*} \tau_p f_Z(z) dz + \int_{|\mathbf{u}'_g|^*}^{\infty} [St_l \cdot (\tau_p - \tau) + \tau] \cdot f_Z(z) dz \tag{3.15}$$

where $f_Z(z)$ is the probability density function of $|\mathbf{u}'_g|$.

This new multiscale interaction time scale is implemented in both multiphase turbulence models investigated in this study. For Model I, Eqs. (3.1–3.4) are solved with τ_{12}^F replaced by $\langle \tau_i \rangle$. With the implementation of $\langle \tau_i \rangle$ in Model I, the steep decay at the beginning of k_f and k_p evolution is improved, and the incorrect trend of k_f decay with increasing particle Stokes numbers is also corrected, as seen in Figure 3.6. For Model II, Eqs. (3.9–3.11) are solved with $\alpha_p \rho_p / D_0$ replaced by $\langle \tau_i \rangle$. The fast decay of particle energy at the beginning of the evolution is eliminated after the implementation of $\langle \tau_i \rangle$ (see Figure 3.7). The incorporation of the multiscale interaction time scale improves the performance of both models tested in this study.

3.3 The Equilibration of Energy Model

Turbulence models for particle–laden flows reviewed in this study use the particle response time τ_p as the timescale for interphase TKE transfer, which results in a very steep decay of particle phase TKE compared with DNS results. In Model I, the decay of k_f with increasing particle Stokes numbers is incorrect. Model I requires an equation for the fluid–particle velocity covariance k_{fp}, which is a pseudo–flow quantity, and it is unclear how this quantity should be initialized and how its boundary values should be specified. Model II uses the single-phase dissipation rate model for turbulent two–phase flows. For all of these reasons, both models are deemed unsatisfactory for general applications.

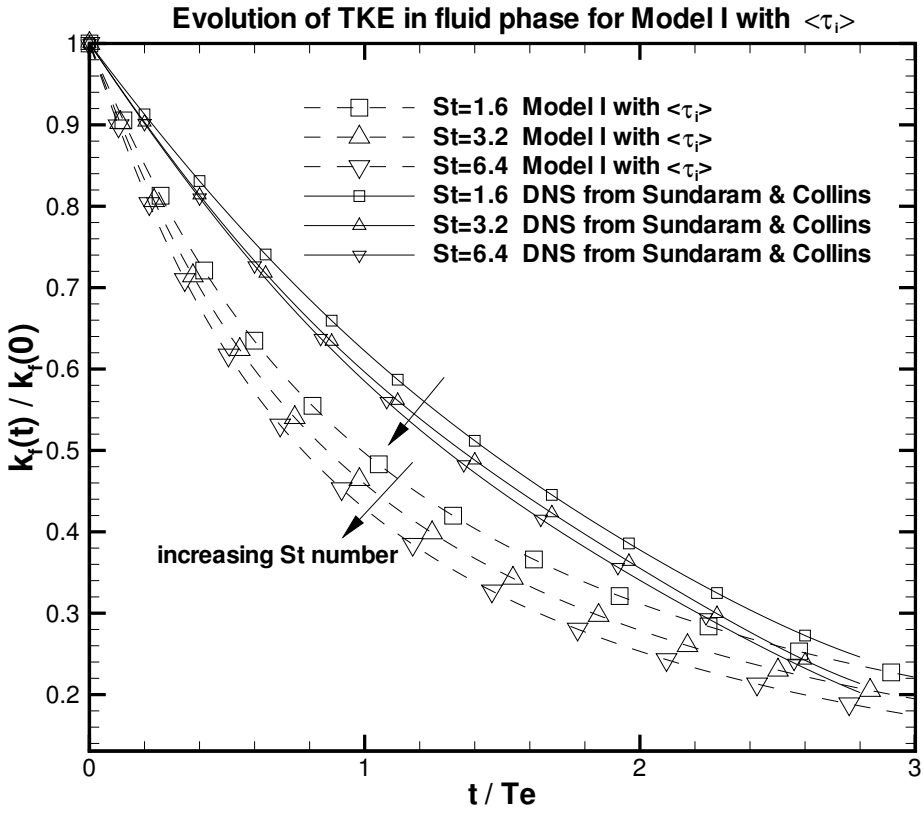

Figure 3.6 Evolution of TKE in fluid phase from Model I with the multi-scale interaction time scale $\langle \tau_i \rangle$.

A new model is proposed in this study that incorporates the mean multiscale interaction timescale $\langle \tau_i \rangle$, and seeks to address some of the difficulties encountered in Model I and Model II. This model is formulated by considering the behavior of a two–phase flow system in the limit of stationary turbulence. In this limit, the mixture TKE is kept constant by artificially forcing the fluid turbulence in a homogeneous particle-laden turbulent flow. The particle phase TKE k_p and fluid energy k_f evolve to their respective equilibrium values k_f^e and k_p^e, over a TKE transfer time scale τ_π, where the superscript e denotes the quantity at the equilibrium state. At the equilibrium state, the ratio of specific fluid energy e_f^e to the specific mixture TKE e_m is a constant, which may depend on mass loading ϕ, particle Stokes number St, particle Reynolds number Re_p and other non-dimensional parameters.

In Section 3.3.2, transport equations for the Reynolds stress tensor in the fluid and particle phases are derived based on the equilibration of energy concept. For simplicity of exposition,

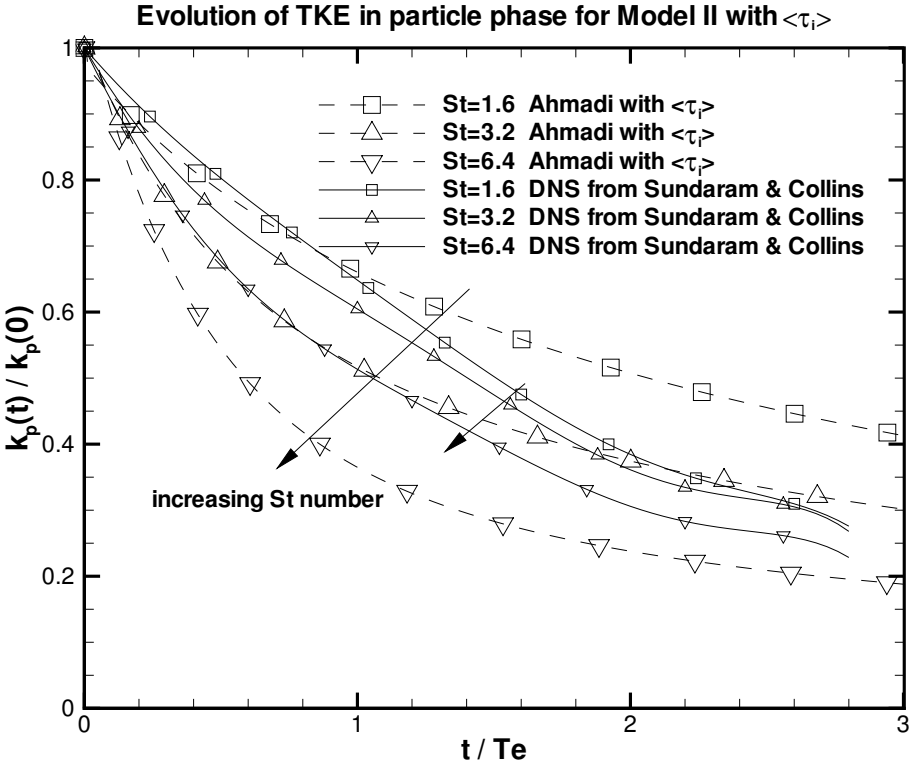

Figure 3.7 Evolution of TKE in particle phase from Model II with the multiscale interaction time scale $\langle \tau_i \rangle$.

we first present the EEM model in the simple case of decaying homogeneous turbulence. The k–ε equation implied by the EEM Reynolds stress model is used to simulate the test case discussed in Section 3.1.

3.3.1 Description of EEM

The model equations are written in terms of specific energy $e_f = \rho_f \alpha_f k_f$ and $e_p = \rho_p \alpha_p k_p$, which are the contributions to the total mixture energy $e_m = \rho_m k_m$ from both phases, where $\rho_m = \rho_f \alpha_f + \rho_p \alpha_p$ is the mixture density. For the decaying homogeneous turbulence, the following equation system holds:

$$\frac{de_f}{dt} = -\frac{(e_f - e_f^e)}{\tau_\pi} - \rho_f \alpha_f \varepsilon_f, \tag{3.16}$$

$$\frac{de_p}{dt} = -\frac{(e_p - e_p^e)}{\tau_\pi}. \tag{3.17}$$

For the test case considered in this study, elastic collisions are assumed in the particle phase, and there is no dissipation of particle energy. However the dissipation of particle energy arising from inelastic collisions can be easily incorporated in Eq. 3.17 if necessary.

Adding Eq. 3.16 and 3.17, the evolution equation for e_m is obtained

$$\frac{de_m}{dt} = -\rho_f \alpha_f \varepsilon_f$$

where the specific mixture energy e_m decays by dissipation in the fluid phase. It is assumed that the interphase TKE transfer term is conservative, in the sense that: $\Pi_{k_f} = -\Pi_{k_p}$. In Model II, the interphase TKE transfer terms are conservative, while the interphase TKE transfer terms in Model I are not conservative.

The equilibrium values of fluid and particle–phase specific energy, $e_f^e = \rho_f \alpha_f k_f$ and $e_p^e = \rho_p \alpha_p k_p$, are determined by a model constant C_2 which is defined as

$$\frac{e_p^e}{e_m} = C_2, \quad \frac{e_f^e}{e_m} = 1 - C_2, \tag{3.18}$$

where C_2 must be bounded by 0 and 1. The model parameter C_2 is the fraction of the specific mixture energy present in the particle phase at equilibrium. The definition of C_2 can be rewritten as:

$$C_2 = \frac{\rho_p \alpha_p k_p^e}{\rho_m k_m} = \frac{\rho_p \alpha_p k_p^e}{\rho_f \alpha_f k_f^e + \rho_p \alpha_p k_p^e} = \frac{\phi \frac{k_p^e}{k_f^e}}{1 + \phi \frac{k_p^e}{k_f^e}} \tag{3.19}$$

Based on dimensional analysis, C_2 can be a function of mass loading ϕ, particle volume fraction α_p, particle Stokes number $St_\eta = \tau_p/\tau_\eta$, particle Reynolds number Re_p, and the initial k_f/k_p ratio. Recall that τ_η is the Kolmogorov timescale and τ_p is the particle response time, which is defined as

$$\tau_p = \frac{\rho_p \bar{d}^2}{\rho_f 18 \nu}$$

where $\bar{d}$ is the mean particle diameter. As the particle response time τ_p increases, it takes longer for the particles to respond to the instantaneous turbulent fluctuations in the fluid phase. For two–phase turbulent flows with constant mass loading ϕ, smaller particle response time τ_p will drive the particle phase equilibrium energy k_p^e closer to the fluid phase equilibrium

energy k_f^e. In the limit of zero Stokes number, the energy in fluid and particle phases is equal and $C_2 = \phi/(1+\phi)$. For a constant particle Stokes number, increasing mass loading would increase the fraction of specific mixture energy in the particle phase at equilibrium.

A model for the fluid–phase dissipation rate is needed to close the equation system Eqs. 3.16–3.17. The fluid phase dissipation rate ε_f in EEM is modeled similar to Simonin's proposal (cf. Eq. 3.2), as

$$\alpha_f \rho_f \frac{d\varepsilon_f}{dt} = -C_{\varepsilon,3} \frac{\varepsilon_f}{k_f} \frac{(e_f - e_f^e)}{\tau_\pi} - C_{\varepsilon,2} \frac{\varepsilon_f^2}{k_f}. \tag{3.20}$$

where the first term represents the influence from interphase TKE transfer (and is modeled as $C_{\varepsilon,3} \frac{\varepsilon_f}{k_f} \Pi_{k_f}$), and the second term represents the dissipation of dissipation rate. Although the EEM dissipation equation is similar to Simonin's proposal, the dissipation rate predicted by EEM is different from Model I. This is because the interphase TKE transfer term is modeled differently: EEM has no k_{fp} variable, and the interphase TKE transfer timescale is τ_π, whereas in Model I it is proportional to the particle response time.

The concept of the equilibration of energy, and the multiscale interaction timescale $\langle \tau_i \rangle$ discussed in Section 3.2, are easily extended to formulate the corresponding transport equations for the Reynolds stress in gas–solid two–phase turbulent flows.

3.3.2 Transport Equation for Reynolds Stress

The Reynolds stress in phase β in a two-phase flow is defined as [Drew (1983); Kataoka et al. (1989); Drew and Passman (1999)] and [Subramaniam (2003)],

$$R_{\beta,ij} \equiv \frac{\left\langle I_\beta \rho u'_{\beta,i} u'_{\beta,j} \right\rangle}{\langle I_\beta \rho \rangle}, \tag{3.21}$$

where $\beta = f$ denotes the fluid phase; and $\beta = p$ represents the particle phase; $\langle \cdot \rangle$ denotes the ensemble average; and I_β is the indicator function for phase β. For constant thermodynamic density, $\langle I_\beta \rho \rangle$ simplifies to $\alpha_\beta \rho_\beta$, where α_β is the volume fraction and ρ_β is the density in β^{th} phase. The fluctuating velocity in phase β is denoted $u'_{\beta,i}$.

A general transport equation for two-phase turbulent flows is derived in [Kataoka et al. (1989); Subramaniam (2003)]. For gas-solid two-phase flows with the constant thermodynamic

density in both phases and with no interphase mass transfer, the transport equation for the Reynolds stress in phase β simplifies to

$$\begin{aligned}
&\langle I_\beta \rho_\beta \rangle \left[\frac{\partial}{\partial t} + U_{\beta,k} \frac{\partial}{\partial x_k} \right] R_{\beta,ij} + \frac{\partial}{\partial x_k} \left\langle I_\beta \rho u'_{\beta,i} u'_{\beta,j} u'_{\beta,k} \right\rangle = \\
&- \left\langle I_\beta \rho u'_{\beta,i} u'_{\beta,k} \right\rangle \frac{\partial U_{\beta,j}}{\partial x_k} - \left\langle I_\beta \rho u'_{\beta,j} u'_{\beta,k} \right\rangle \frac{\partial U_{\beta,i}}{\partial x_k} \\
&+ \left\langle u'_{\beta,i} \frac{\partial (I_\beta \tau_{kj})}{\partial x_k} \right\rangle + \left\langle u'_{\beta,j} \frac{\partial (I_\beta \tau_{ki})}{\partial x_k} \right\rangle + \left\langle u'_{\beta,i} S_{\beta,Mj} \right\rangle + \left\langle u'_{\beta,j} S_{\beta,Mi} \right\rangle
\end{aligned} \tag{3.22}$$

The terms on the the first line from left to right are: the material derivative of the Reynolds stress in phase β following $U_{\beta,k}$ (the mean velocity in phase β); the triple velocity correlation term. The terms on the second line are the production of Reynolds stress due to the mean velocity gradients. The terms on the third line from left to right are: fluctuating velocity-stress gradient correlation (first two terms) and fluctuating velocity-interfacial momentum transfer correlation (last two terms). In Eq. 3.22, $S_{\beta,Mj}$ is the interphase momentum transfer source term in phase β. In the above equation, the production terms and the material derivative of Reynolds stress are in closed form. The triple velocity correlation term, and the fluctuating velocity-interfacial momentum transfer correlation terms need model closures.

Triple Velocity Correlation term

The triple velocity correlation term in fluid phase is modeled using the gradient-diffusion concept,

$$\frac{\partial}{\partial x_k} \left\langle I_f \rho u'_{f,i} u'_{f,j} u'_{f,k} \right\rangle = \frac{\partial}{\partial x_k} \left[\alpha_f \rho_f C_s \frac{k_f^2}{\varepsilon_f} \frac{\partial}{\partial x_k} \left\langle u'_{f,i} u'_{f,j} \right\rangle \right], \tag{3.23}$$

where C_s is a model constant.

In the particle–phase Reynolds stress equation, the triple velocity correlation term is also modeled using the gradient-diffusion concept as,

$$\frac{\partial}{\partial x_k} \left\langle I_p \rho u'_{p,i} u'_{p,j} u'_{p,k} \right\rangle = \frac{\partial}{\partial x_k} \left[\alpha_p \rho_p C_{s,p} \left\langle \tau_i \right\rangle k_p \frac{\partial}{\partial x_k} \left\langle u'_{p,i} u'_{p,j} \right\rangle \right], \tag{3.24}$$

where $\langle \tau_i \rangle$ is the multiscale interaction timescale discussed in Section 3.2 and $C_{s,p}$ is a model constant. The model constants C_s and $C_{s,p}$ need to be determined based on experimental data or DNS results.

Interphase Energy Transfer Terms

The fluctuating velocity-interfacial momentum transfer correlation terms in the last line of Eq. 3.22 are modeled using the Equilibration of Energy concept. For the fluid phase, the interphase energy transfer term is modeled as

$$\left\langle u'_{f,i} S_{f,Mj} \right\rangle + \left\langle u'_{f,j} S_{f,Mi} \right\rangle = -\alpha_f \rho_f \frac{\left(\left\langle u'_{f,i} u'_{f,j} \right\rangle - \delta_{ij} \frac{2}{3} k_f^e \right)}{\tau_\pi}, \tag{3.25}$$

where k_f^e is the fluid phase TKE at the equilibrium state. For the particle phase, the interphase energy transfer term is modeled as

$$\left\langle u'_{p,i} S_{p,Mj} \right\rangle + \left\langle u'_{p,j} S_{p,Mi} \right\rangle = -\alpha_p \rho_p \frac{\left(\left\langle u'_{p,i} u'_{p,j} \right\rangle - \delta_{ij} \frac{2}{3} k_p^e \right)}{\tau_\pi}, \tag{3.26}$$

where k_p^e is the particle phase TKE at the equilibrium state. Contracting indices of Eqs. 3.25–3.26 results in twice the interphase TKE transfer terms in Eqs. 3.16–3.17.

Model Equation for Dissipation rate in Fluid Phase ε_f

The fluctuating velocity-stress gradient correlation terms in the fluid phase include the dissipation of fluid energy due to the viscous effects in the flow field, and are modeled by $\varepsilon_{f,ij} = \delta_{ij} \varepsilon_f$ as a consequence of local isotropy. The modeled evolution equation for ε_f is

$$\begin{aligned} \alpha_f \rho_f \frac{\partial \varepsilon_f}{\partial t} + \alpha_f \rho_f U_{f,i} \frac{\partial \varepsilon_f}{\partial x_i} &= \alpha_f \rho_f \frac{\partial}{\partial x_i} \left(C_\varepsilon \frac{k_f}{\varepsilon_f} \left\langle u'_{f,i} u'_{f,j} \right\rangle \frac{\partial \varepsilon_f}{\partial x_i} \right) - \alpha_f \rho_f C_{\varepsilon,1} \frac{\varepsilon_f}{k_f} \cdot \left\langle u'_{f,i} u'_{f,j} \right\rangle \frac{\partial U_{f,i}}{\partial x_j} \\ &\quad - \alpha_f \rho_f C_{\varepsilon,2} \frac{\varepsilon_f^2}{k_f} + \alpha_f \rho_f C_{\varepsilon,3} \frac{\varepsilon_f}{k_f} \cdot \frac{\left(k_f^e - k_f \right)}{\tau_\pi}, \end{aligned} \tag{3.27}$$

where τ_π is the interphase TKE transfer timescale. The model constants are chosen to be $C_{\varepsilon,1} = 1.44$, $C_{\varepsilon,2} = 1.92$, $C_{\varepsilon,3} = 1.2$ and $C_\varepsilon = 0.15$. The model constants $C_{\varepsilon,1}$, $C_{\varepsilon,2}$ and C_ε are chosen after the dissipation model for single phase turbulence [Launder (1996)]. The value of $C_{\varepsilon,3}$ is taken to be 1.2 as suggested by Simonin (1996b).

Since elastic collisions are assumed in particle phase in this study, the dissipation rate in particle energy k_p is zero in the particle phase Reynolds stress transport equation. However, the dissipation of particle Reynolds stress due to inelastic collisions can be easily incorporated in the modeled evolution equation for the particle Reynolds stress tensor.

3.3.3 The k–ε Equations for Particle-laden Turbulent Flow

The k–ε equations for gas-solid two-phase turbulent flows can be obtained by contracting the indices of the transport equation for the Reynolds stress tensor. In the k–ε formulation, the fluid velocity covariance $\left\langle u'_{f,i}u'_{f,j}\right\rangle$ appearing in the production of Reynolds stress (cf. Eq. 3.22) needs a closure model. It is modeled using a turbulent eddy viscosity ν_f^T as

$$\left\langle u'_{f,i}u'_{f,j}\right\rangle = -\nu_f^T\left[\frac{\partial U_{f,i}}{\partial x_j}+\frac{\partial U_{f,i}}{\partial x_j}\right]+\frac{2}{3}\delta_{ij}\left[k_f+\nu_f^T\frac{\partial U_{f,k}}{\partial x_k}\right]. \tag{3.28}$$

The turbulent eddy viscosity ν_f^T in fluid phase is modeled as

$$\nu_f^T = C_\mu\frac{k_f^2}{\varepsilon_f}.$$

The model constant C_μ could be a function of particle Stokes number St_η, and mass loading ϕ. Since there is no DNS data to validate the turbulent eddy viscosity hypothesis in turbulent particle–laden flows, the model constant C_μ is chosen to be 0.09, which is the value in single–phase turbulence models.

For relatively dense collision-dominated mixtures, the turbulent eddy viscosity in particle phase is modeled as $\mu_p^T = C_{\mu 2}\alpha_p\rho_p\bar{d}(k_p)^{1/2}$ in Ahmadi's work [Ahmadi and Ma (1990); Ma and Ahmadi (1990)], where $C_{\mu 2}$ is a function of particle volume fraction and $\bar{d}$ is the mean diameter of particle phase. For dilute mixtures, fluid turbulence is dominant and particles are transported by the fluid motion. It is suggested in [Besnard and Harlow (1985); Ahmadi and Ma (1990)] that the fluid length scale should be the relevant scale in μ_p^T. The multiscale interaction time $\langle\tau_i\rangle$ is a function of k_f, which is the appropriate scale to model the dilute mixture. So for particle phase, the particle velocity covariance tensor is modeled as

$$\left\langle u'_{p,i}u'_{p,j}\right\rangle = -\nu_p^T\left[\frac{\partial U_{p,i}}{\partial x_j}+\frac{\partial U_{p,j}}{\partial x_i}\right]+\frac{2}{3}\delta_{ij}\left[k_p+\nu_p^T\frac{\partial U_{f,k}}{\partial x_k}\right], \tag{3.29}$$

where

$$\nu_p^T = C_{\mu 2}k_p\left\langle\tau_i\right\rangle,$$

and $C_{\mu 2}$ is the model constant that can be obtained by comparing with experimental data or DNS results. This corresponds to specifying $\mu_p^T = C_{\mu 2}\alpha_p\rho_p\left\langle\tau_i\right\rangle k_p$. In this study $C_{\mu 2}$ is chosen to be 0.001.

Based on the transport equation for the Reynolds stress tensor, the k–ε model corresponding to the EEM Reynolds stress model for fluid and particle–phase is

$$\begin{aligned}
\alpha_f\rho_f\frac{\partial k_f}{\partial t}+\alpha_f\rho_f U_{f,i}\frac{\partial k_f}{\partial x_i} &= \frac{\partial}{\partial x_j}\left(\alpha_f\rho_f\frac{\nu_f^T}{\sigma_{k_f}}\frac{\partial k_f}{\partial x_j}\right)-\alpha_f\rho_f\left\langle u'_{f,i}u'_{f,j}\right\rangle\frac{\partial U_{f,i}}{\partial x_j}-\alpha_f\rho_f\varepsilon_f \\
&\quad -\alpha_f\rho_f\frac{(C_2k_f-(1-C_2)\phi k_p)}{\tau_\pi}, \qquad (3.30)\\
\alpha_f\rho_f\frac{\partial \varepsilon_f}{\partial t}+\alpha_f\rho_f U_{f,i}\frac{\partial \varepsilon_f}{\partial x_i} &= \frac{\partial}{\partial x_j}\left(\alpha_f\rho_f\frac{\nu_f^T}{\sigma_\varepsilon}\frac{\partial \varepsilon_f}{\partial x_j}\right)-C_{\varepsilon,1}\alpha_f\rho_f\frac{\varepsilon_f}{k_f}\left\langle u'_{f,i}u'_{f,j}\right\rangle\frac{\partial U_{f,i}}{\partial x_j} \\
&\quad -C_{\varepsilon,2}\alpha_f\rho_f\frac{\varepsilon_f^2}{k_f}-\alpha_f\rho_f C_{\varepsilon,3}\frac{\varepsilon_f}{k_f}\frac{(C_2k_f-(1-C_2)\phi k_p)}{\tau_\pi}, \qquad (3.31)\\
\alpha_p\rho_p\frac{\partial k_p}{\partial t}+\alpha_p\rho_p U_{p,i}\frac{\partial k_p}{\partial x_i} &= \frac{\partial}{\partial x_j}\left(\alpha_p\rho_p\nu_p^T\frac{\partial k_p}{\partial x_j}\right)-\alpha_p\rho_p\left\langle u'_{p,i}u'_{p,j}\right\rangle\frac{\partial U_{p,i}}{\partial x_j} \\
&\quad -\alpha_p\rho_p\frac{\left((1-C_2)k_p-\frac{C_2}{\phi}k_f\right)}{\tau_\pi}, \qquad (3.32)
\end{aligned}$$

where $\sigma_{k_f}=1.0$ and $\sigma_\varepsilon=1.3$.

3.3.4 Model Results for Decaying Homogeneous Turbulence

In this section the simplified equations for decaying homogeneous turbulence are described. The predictions from EEM for decaying homogeneous particle–laden turbulent flows are compared with DNS results.

The EEM equation system for decaying homogeneous turbulence is

$$\begin{aligned}
\frac{dk_f}{dt} &= -\frac{1}{\tau_\pi}\left[C_2k_f-(1-C_2)\phi k_p\right]-\varepsilon_f, \qquad (3.33)\\
\frac{d\varepsilon_f}{dt} &= -C_{\varepsilon,3}\frac{\varepsilon_f}{k_f}\frac{\left[C_2k_f-(1-C_2)\phi k_p\right]}{\tau_\pi}-C_{\varepsilon,2}\frac{\varepsilon_f^2}{k_f}, \qquad (3.34)\\
\frac{dk_p}{dt} &= -\frac{1}{\tau_\pi}\left[(1-C_2)k_p-\frac{C_2}{\phi}k_f\right]. \qquad (3.35)
\end{aligned}$$

The interphase TKE transfer time scale τ_π is related to the multiscale interaction timescale $\langle\tau_i\rangle$ (which was introduced in Section 3.2) by the expression,

$$\tau_\pi=\frac{\langle\tau_i\rangle}{C_\pi} \quad \text{or} \quad C_\pi=\frac{\langle\tau_i\rangle}{\tau_\pi}, \qquad (3.36)$$

where C_π is chosen to be 2.5 in this model.

As discussed in Section 3.3.1, in general C_2 is a function of mass loading ϕ, particle volume fraction α_p, particle Stokes number St_η, particle Reynolds number Re_p, and initial k_f/k_p ratio. In the absence of relevant data from DNS of stationary turbulence, it is hypothesized that the mass loading ϕ of the system strongly affects C_2, whereas it is likely that C_2 depends very little on particle Stokes number St_η. The dependence on the particle volume fraction α_p is neglected for dilute flows. For particle Reynolds number in Stokes regime $Re_p \sim 1$, the dependence of C_2 on the particle Reynolds number Re_p is also neglected. For simplicity, C_2 is also assumed to be independent of initial k_f/k_p ratio, but this assumption may not be justified for initial k_f/k_p ratio far from one. Under these assumptions, C_2 is modeled as a linear function of mass loading ϕ,

$$C_2 = 0.6\phi. \tag{3.37}$$

This specification is chosen such that the model predictions from EEM match well with DNS results. It is natural to require the model for C_2 to reproduce the correct limiting value $\phi/(1+\phi)$ as $St_\eta \to 0$. With the current specification of $C_2 = 0.6\phi$, the value of C_2 in the limit $St_\eta \to 0$ differs from $\phi/(1+\phi)$ by approximately 10%. The model constants used in EEM are listed in Table 3.1.

Table 3.1 The coefficients for EEM.

C_μ	$C_{\varepsilon,2}$	$C_{\varepsilon,1}$	σ_{k_f}	σ_ε	$C_{\varepsilon,3}$	$C_{\mu 2}$	C_π
0.09	1.92	1.44	1.0	1.3	1.2	0.001	2.5

The predictions from EEM are shown in Figures 3.8 and 3.9. The model results match the DNS results for fluid–phase TKE evolution quite well at early time (see Figure 3.8), but a small quantitative discrepancy is observed after $t/T_e > 1.5$. The decay rate in particle energy shows larger separation with increasing particle Stokes number than the DNS (see Figure 3.9), but the overall trend is satisfactory.

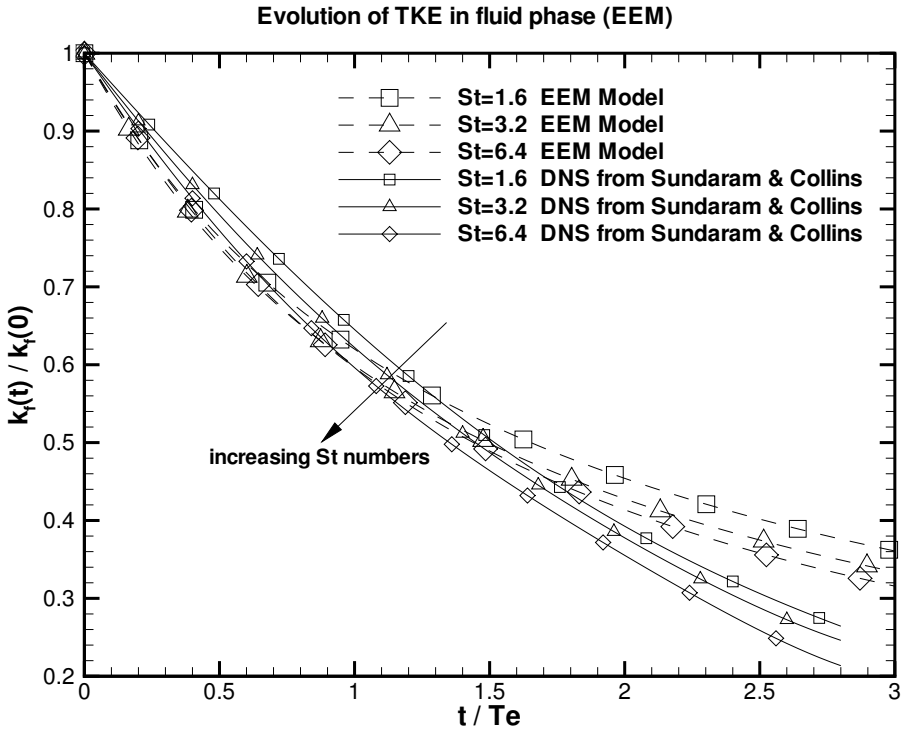

Figure 3.8 Evolution of TKE in fluid phase for EEM compared with DNS data.

3.4 Particle-laden Turbulent Homogeneous Shear Flow

In this section the test case of particle-laden homogeneous shear flow is described, and major results from the DNS study by Ahmed and Elghobashi (2000) are discussed. The predictions from Model I and EEM are then compared with DNS data.

3.4.1 Description of Test Case

In the DNS study of particle-laden homogeneous shear flow by Ahmed and Elghobashi (2000), the flow field has an identical imposed mean velocity for both phases. In the fluid phase, the x_1 component of mean velocity U varies linearly in x_3 ($U = Sx_3$), where S is the mean velocity gradient taken to be $S = 1$ in the simulation. The x_1 component of particle phase mean velocity is also imposed with unit mean velocity gradient. The mean velocity in x_2 and x_3 direction is zero in both fluid and particle phase. A schematic of the flow configuration

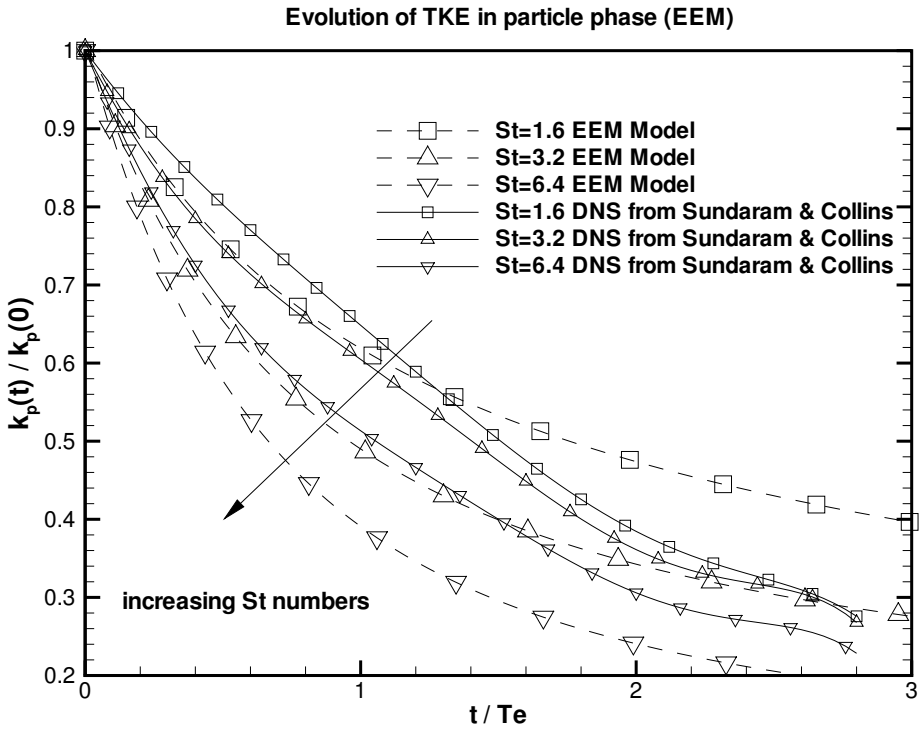

Figure 3.9 Evolution of TKE in particle phase for EEM compared with DNS data.

is shown in Figure 3.10. The solid particles are rigid spheres (ρ_p is constant), and there is no interphase mass transfer. The particle volume fraction is small ($\alpha_p < 10^{-3}$), and the effect of the presence of particles on the fluid mass conservation equation is neglected. The particle size is in the sub-Kolmogorov range. The point-particle approximation is also used in this DNS study, so a linear drag law is assumed for each particle.

The major results from the particle–laden homogeneous shear flow DNS are:

(i) The evolution of the fluid velocity covariance $\left\langle u'_{f,1} u'_{f,3} \right\rangle$ is reported for $\tau_p = 1.0$ and mass loading $\phi = 1.0$. The fluid velocity covariance is important to validate the assumption of turbulent eddy viscosity in Eq. 3.28.

(ii) The effect of varying the particle inertia ($\tau_p = 0.1, 0.25, 0.5, 1.0$) on the evolution of fluid phase TKE is studied. It is found that as the particle inertia increases, the decay rate of fluid phase TKE increases (for fixed mass loading ϕ).

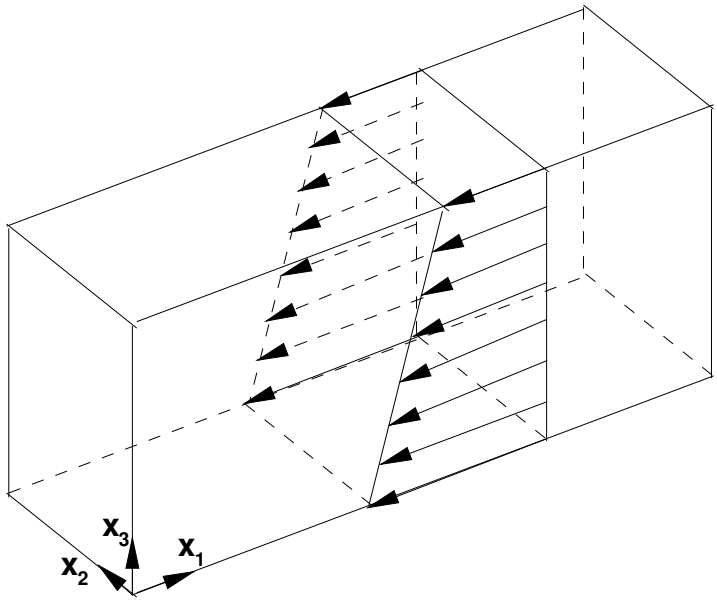

Figure 3.10 Schematic of the flow configuration in the particle-laden homogeneous shear flow.

3.4.2 Comparative Assessment of Model Results

The simplified governing equations for particle–laden homogeneous shear flow from Model I can be found in Xu (2004). Model II results are not presented for the homogeneous shear test case because the volume fraction of particles in this test is well beyond the realm of applicability of Model II's closure for the TKE production in particle phase (see Xu (2004)). The particle phase TKE production term in Model II is modeled using a turbulent eddy viscosity analogy, and is intended for rapid granular flows where the effect of the fluid phase is negligible (or secondary), and the transport of momentum is dominated by particle–particle collisions. The particle TKE production term in the k_p equation has a $1/\alpha_p$ dependence (arising from the model constant $C_{\mu 2}$) that becomes unbounded in the limit $\alpha_p \to 0$. (These details of Model II are given in Xu (2004).) If this closure model is used for volumetrically dilute flows (the particle–laden homogeneous shear flow studied here is quite dilute, with α_p around 10^{-4}), then the particle TKE production term results in an unphysical growth of k_p. Therefore, only predictions from Model I and EEM are compared with DNS results for this case.

For EEM the simplified governing equations for homogeneous shear flow are

$$\frac{dk_f}{dt} = \Pi_{k_f} - \varepsilon_f - \left\langle u'_{f,1}u'_{f,3}\right\rangle \frac{\partial U_{f,1}}{\partial x_3}, \tag{3.38}$$

$$\frac{d\varepsilon_f}{dt} = \Pi_{\varepsilon_f} - \frac{\varepsilon_f}{k_f}\left[C_{\varepsilon,1}\left\langle u'_{f,1}u'_{f,3}\right\rangle \frac{\partial U_{f,1}}{\partial x_3} + C_{\varepsilon,2}\varepsilon_f\right], \tag{3.39}$$

$$\frac{dk_p}{dt} = \Pi_{k_p} - \left\langle u'_{p,1}u'_{p,3}\right\rangle \frac{\partial U_{p,1}}{\partial x_3}, \tag{3.40}$$

where Π_{k_f}, Π_{ε_f} and Π_{k_p} represent the influence of interphase TKE transfer. The velocity covariance in the fluid phase $\left\langle u'_{f,i}u'_{f,j}\right\rangle$ and the velocity covariance in particle phase $\left\langle u'_{p,i}u'_{p,j}\right\rangle$ are modeled using the turbulent eddy viscosity concept (cf. Eqs. 3.28 and 3.29).

For $\tau_p = 1.0$ and $\phi = 1.0$, the evolution of fluid phase energy is compared in Figure 3.11. It is found that the decay rate of k_f from Model I is much steeper than DNS results, which is up to 70% off at $T = 3$. With the implementation of $\langle\tau_i\rangle$ in Model I by replacing the time scale τ_{12}^F in Eqs. (3.1–3.4) , the steep decay of fluid phase TKE is improved, and the quantitative difference is around 30% at $T = 3$. EEM predicts that the decay rate of k_f quite close to the DNS results at the beginning of evolution $T < 1$. After $T > 1$, the fluid energy starts to increase. In EEM's results, the relative error is 20% off at $T = 3$ compared with DNS results.

For Model I, the budget plot is shown in Figure 3.12, which shows that the interphase TKE transfer term is dominant and contributes most to the fast decay at early time. The budget of the interphase TKE transfer term, dissipation rate and the production in Eq. 3.38 for EEM is plotted in Figure 3.13. It shows that the growth of fluid phase TKE is mainly due to the almost linear increase in the production as time evolves. The budget plot in Figure 3.13 also shows that production and dissipation rate are the two major terms in the fluid energy evolution equation (interphase TKE transfer is very small). The evolution of fluid–phase dissipation rate ε_f is also reported in the DNS study. If the fluid–phase dissipation rate in the EEM model is specified from DNS data, the growth of fluid energy is eliminated, as seen in Figure 3.14. This shows that if the fluid dissipation can be modeled with more accuracy, the predictions from EEM can be further improved.

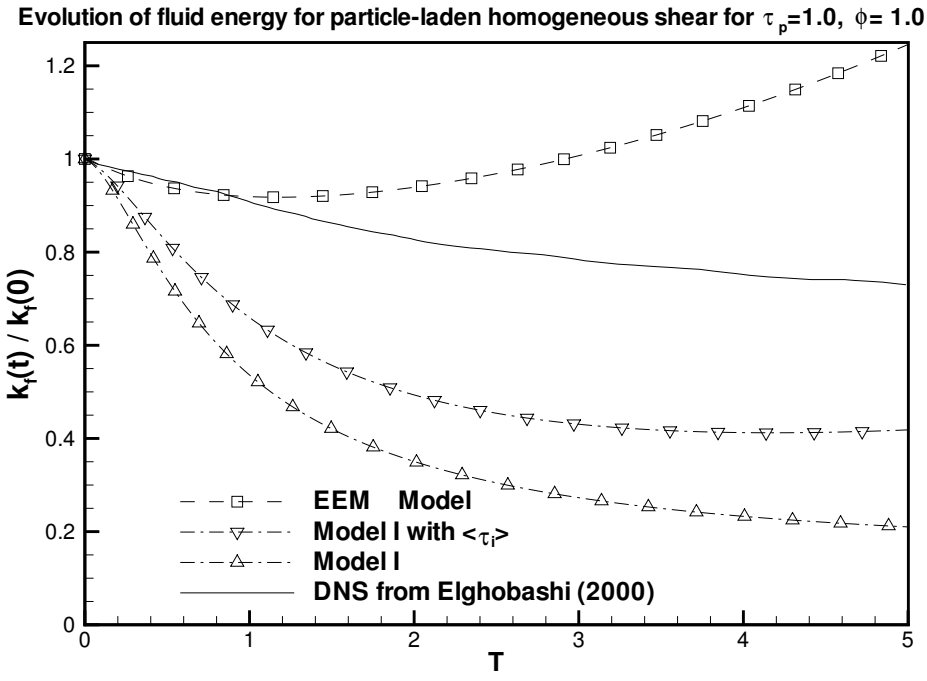

Figure 3.11 Evolution of TKE in fluid phase for Model I, Model I with multiscale interaction time scale $\langle \tau_i \rangle$, and EEM model for homogeneous particle-laden shear flow.

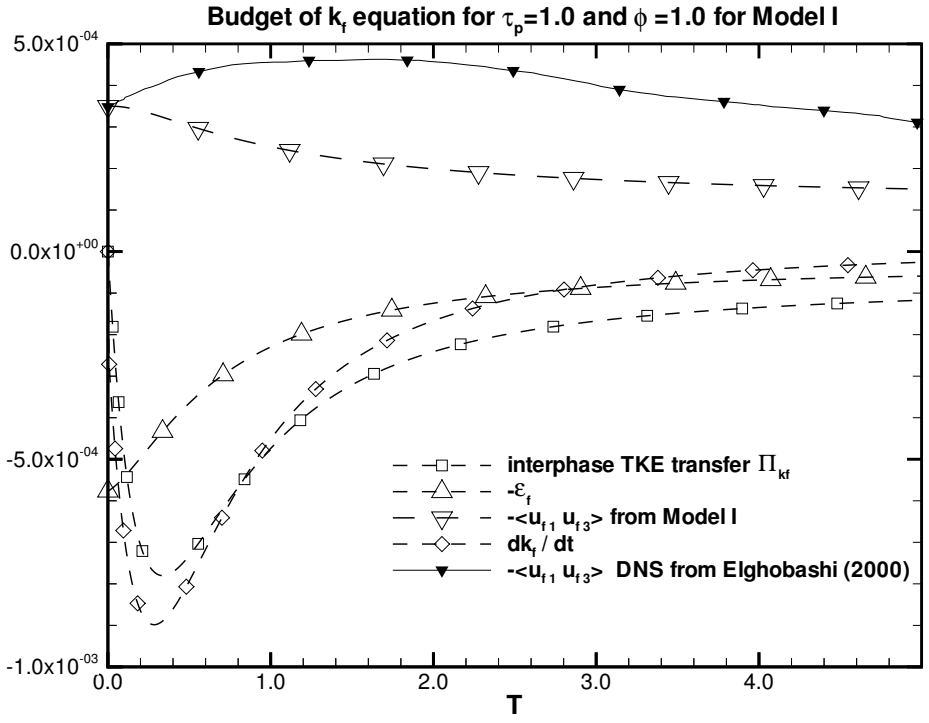

Figure 3.12 Budget plot for fluid–phase TKE equation from Model I for $\phi = 1.0$ and $\tau_p = 1.0$ in homogeneous particle–laden shear flow. Note that the production term equals $-\left\langle u'_{f,1}u'_{f,3}\right\rangle$ since the mean velocity gradient S is one.

The velocity covariance $\left\langle u'_{f,1}u'_{f,3}\right\rangle$ is reported for $\tau_p = 1.0$, $\phi = 1.0$ in the DNS results. Since this term determines the production term in the k–ε equations for fluid phase (cf. Eq. 3.30, 3.31), it is important to model this quantity accurately. In this test case, the velocity covariance $-\left\langle u'_{f,1}u'_{f,3}\right\rangle$ equals to the shear production since the mean velocity gradient S is one. In Figures 3.12 and 3.13 the comparison of $\left\langle u'_{f,1}u'_{f,3}\right\rangle$ shows a large discrepancy between the DNS and model results. However, it is perhaps more appropriate to compare the correlation coefficient ρ_{f13}, which is defined as

$$\rho_{f13} = \frac{\left\langle u'_{f,1}u'_{f,3}\right\rangle}{\sqrt{\left\langle u'_{f,1}u'_{f,1}\right\rangle\left\langle u'_{f,3}u'_{f,3}\right\rangle}}, \tag{3.41}$$

and this comparison is shown in Fig. 3.15. There is a large difference at early time, but after $T = 4$ the difference is small. The discrepancy could be due to the influence of initial

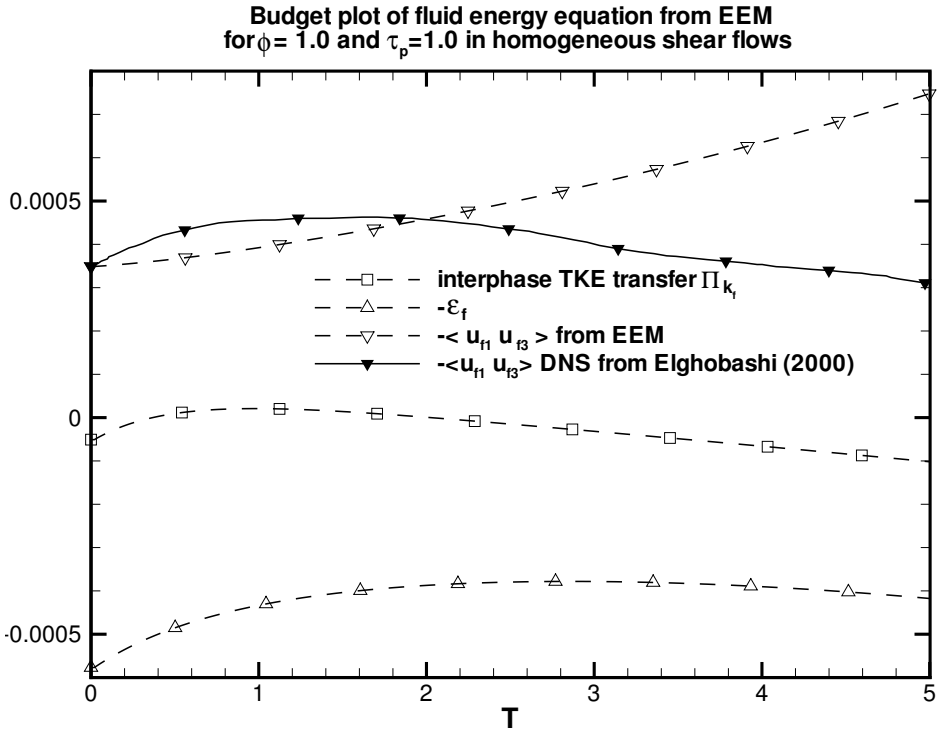

Figure 3.13 Budget plot for fluid TKE equation in EEM model for $\phi = 1.0$ and $\tau_p = 1.0$ in homogeneous particle–laden shear flow. Note that the production term equals $-\left\langle u'_{f,1}u'_{f,3}\right\rangle$ since the mean velocity gradient S is one.

conditions or the interphase TKE transfer term.

The particle inertia study is performed for $\tau_p = 0.1, 0.25, 0.5, 1.0$ with the same mass loading $\phi = 0.1$. DNS data show that with the increasing particle response time, the decay rate of k_f increases. The predictions of Model I is shown in Figure 3.16, where Model I gives the *opposite* trend with increasing particle response time τ_p (or particle inertia). After implementing the multiscale interaction timescale $\langle\tau_i\rangle$ in place of τ_{12}^F in Model I, the incorrect trend of fluid phase TKE decay rate is corrected and the evolution of fluid energy becomes closer to the DNS results, as seen in Figure 3.16.

The model results from EEM for particle inertia study are shown in Figure 3.17. These results are very close to DNS data, and the trend of TKE evolution with increasing particle inertia is correct. However, the difference in the decay rate of fluid energy with increasing

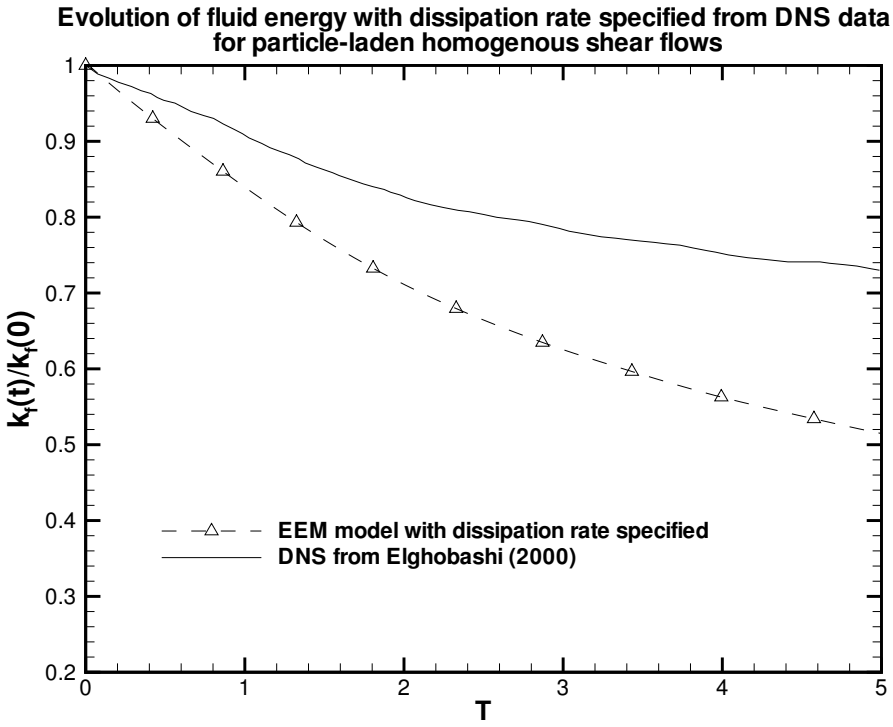

Figure 3.14 Evolution of TKE in fluid phase for EEM model with dissipation rate specified from DNS results for the particle-laden homogeneous shear flow with $\phi = 1.0$ and $\tau_p = 1.0$. Fluid–phase TKE evolution from DNS is also shown for comparison.

particle inertia is too small. A possible reason for this deficiency is that there is no information of particle inertia in the fluid phase production term. One improvement is to use $\langle \tau_i \rangle$ to substitute eddy turnover time in ν_f^T. However, without detailed DNS data for variation of shear production with different particle inertia, the model for fluid and particle shear production terms in EEM cannot be validated.

3.5 Discussion

With the Equilibration of Energy Concept, the evolution of TKE in fluid and particle phase is shown to be improved when compared with the DNS results of decaying homogeneous particle–laden turbulence and homogeneous particle–laden shear flow. Incorporation of the multiscale interaction timescale $\langle \tau_i \rangle$ in Model I and Model II corrects the incorrect trend of

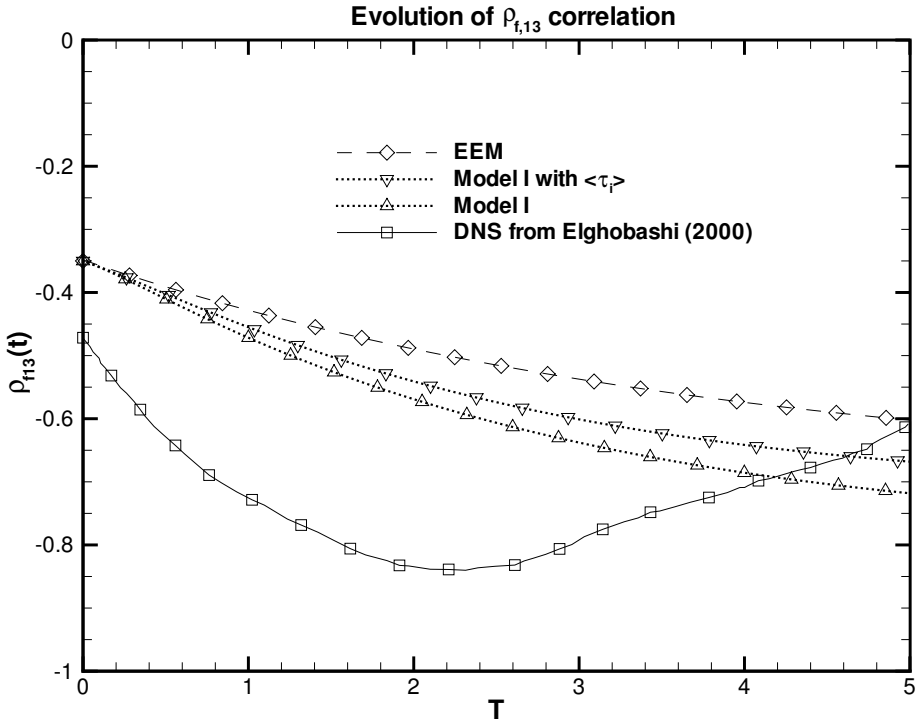

Figure 3.15 Evolution of the velocity correlation ρ_{f13} for Model I, Model I implemented with multiscale interaction time scale $\langle \tau_i \rangle$, and EEM model in homogeneous particle-laden shear flow. DNS result is shown for comparison.

k_f decay rate with increasing particle inertia, and the evolution of TKE in fluid and particle phase is shown to match with DNS results satisfactorily. Implicit in the above statement is the assumption that the DNS is itself an accurate representation of the physics of the particle–laden turbulent flows. The point particle assumption for the *particle drag* in such DNS studies is justified in a limited flow regime where particle Reynolds numbers Re_p are of order one, the density ratio $\rho_p/\rho_f \sim \mathcal{O}(1000)$ and particles are sub-Kolmogorov size with negligible wake effects. Also volume displacement effects are neglected in such DNS studies, and the fluid velocity field is assumed to be solenoidal.

The homogeneous problem that forms the basis of this study, and for which the DNS database exists, corresponds to a flow regime where the aforementioned assumptions are valid. However, a good approximation to the particle drag in the DNS does not necessarily guarantee accurate calculation of the fluid-phase dissipation rate in the presence of particles. Also

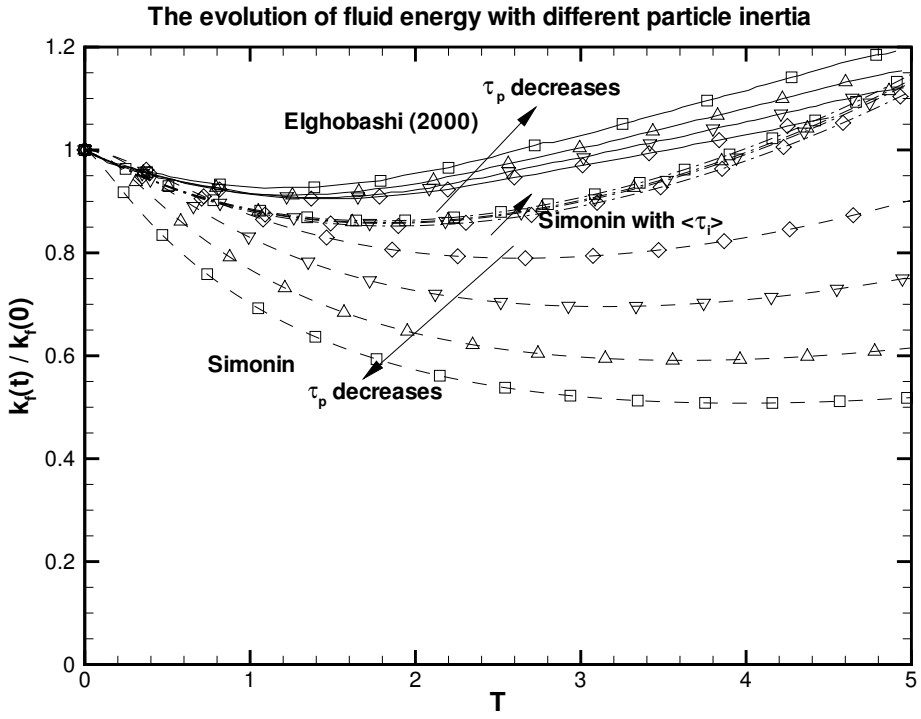

Figure 3.16 Evolution of TKE in fluid phase with increasing particle inertia (constant mass loading) for particle–laden homogeneous shear flow. Solid line represents DNS results; dashline represents the predictions from Model I; dashdot line represents the results from Model I improved with multiscale interaction timescale $\langle \tau_i \rangle$. The symbol $\square$ represents $\tau_p = 0.1$; $\triangle$ represents $\tau_p = 0.25$; $\triangledown$ represents $\tau_p = 0.5$; and $\diamond$ represents $\tau_p = 1.0$.

particle–particle interaction effects are not accounted for in the point-particle approximation, and the effect of the point-particle approximation on the pressure field is not quantified either.

The only way to test these approximations is by performing *true* DNS, where flow field around each particle is fully resolved and exact boundary conditions are imposed on particle surface. Using such *true* DNS calculations the consequence of the point-particle approximation on the solenoidality of the fluid velocity field (which will in turn affect the fluid pressure field), and the neglect of particle–particle interaction effects can be evaluated. Recent studies by Moses and Edwards (2005) seek to assess the consequences of the point-particle approximation. However, their study is in 2–D for considerably large cylinders (particle Reynolds number based on diameter of cylinder $Re_p = 26$), with an emphasis on evaluating the effects of filtering the

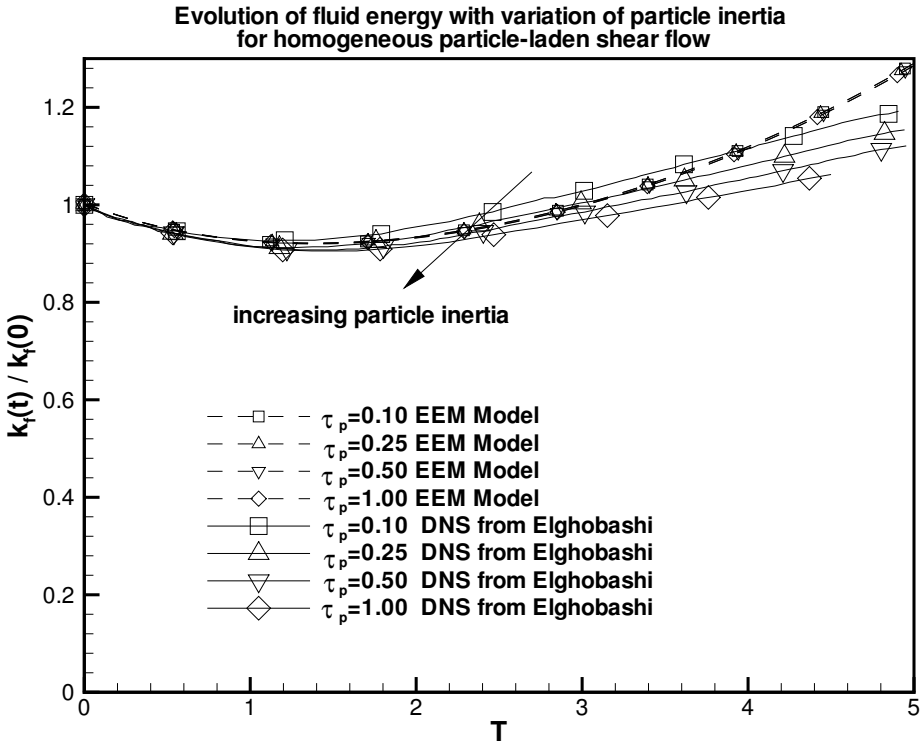

Figure 3.17 Evolution of TKE in fluid phase for increasing particle response time τ_p (constant mass loading $\phi = 0.1$) from EEM. DNS data is shown for comparison.

velocity field. Their study is relevant to the examination of the validity of LES based on the point-particle approximation. Similar studies are necessary for DNS, but such calculations are still limited by computational cost. Therefore, the DNS datasets performed with point-particle approximation that are used in this study are the best data available for model testing and validation.

It appears likely that the existing DNS database *does* capture the major trends of the TKE variation with important non-dimensional parameters like Stokes numbers and mass loading. It is possible that the true DNS might revise the exact quantitative predictions. Since the principal conclusions in this study concern qualitative trends rather than an exact quantitative match between model predictions and DNS results, it is reasonable to assert that incorporation of the new multiscale interaction timescale leads to a better representation of the problem physics.

It is worthwhile to examine whether any experimental data can be used for model validation. Experimental study of nearly isotropic particle–laden turbulence includes work by Fallon and Rogers (2002). This work reports the preferential concentration of particles in microgravity conditions with variation of particle Stokes number, but the turbulence kinetic energy in either phase that is required for model validation is not reported. While this experimental result is useful for models that predict preferential concentration, information of the second moments of fluid and particle fluctuating velocity that is useful for model validation is not reported.

Experimental investigation of homogeneous dilute particle–laden flows includes studies by Parthasarathy and Faeth (1990). This work investigates the settling of uniform flux of monodisperse spherical particles in a stagnant water bath. This study reports the second moments of fluctuating velocity in fluid phase varying with particle volume fraction and particle sizes, but there is no systematic study of TKE evolution with variation of important non-dimensional parameters, such as particle Stokes number. The results of these experiments will be useful for further evaluation of model performance, now that the model constants have been determined based on comparison with DNS of particle–laden turbulence.

3.6 Summary

Two multiphase turbulence models (Model I due to Simonin (1996b,a) and Model II from [Ahmadi and Ma (1990); Ma and Ahmadi (1990); Ahmadi (1989)]) are compared with direct numerical simulations (DNS) of two canonical flows: decaying homogeneous particle-laden turbulence [Sundaram and Collins (1999)], and homogeneous particle-laden shear flow [Ahmed and Elghobashi (2000)]. The principal findings from this comparative assessment of the two models are:

(1) For homogeneous particle–laden turbulent flow, both models predict a faster decay rate of fluctuating energy (in both phases) than found in the DNS. The reason for the faster decay is that the particle response time ($\tau_p = d^2\rho_p/18\mu_f$) is used as the time scale for interphase TKE transfer in both models. For monodisperse particles there is a single particle response time scale. The results indicate that a single particle response time does not adequately

characterize the interaction between the particles and the range of turbulent eddy sizes, which is responsible for interphase TKE transfer.

(2) Anomalous variation of TKE with different particle Stokes numbers is found in the Model I results. The interphase TKE transfer is the dominant term in Model I that causes this anomalous model behavior. A pseudo-flow quantity k_{fp} is introduced in the interphase TKE transfer terms in Model I, and the particle response time is used as the relevant time scale for interphase TKE transfer.

The following areas for model improvement are identified: (i) model for interphase TKE transfer, especially the time scale of interphase TKE transfer, and (ii) correct prediction of TKE evolution with variation of particle Stokes number. In Model I the fluid-particle covariance k_{fp} is introduced, which is not an independent flow variable in single–point closure of two-phase turbulent flows, and it is unclear how the initial and boundary conditions for this term should be specified. These deficiencies in Model I and Model II limit the application of these two models.

A new multiphase turbulence model, Equilibration of Energy Model (EEM), is proposed in this report. A noteworthy feature of EEM is that a multiscale interaction time scale $\langle \tau_i \rangle$ is proposed to account for the interaction of a particle with a range of eddy sizes. As the particle Stokes number approaches zero, $\langle \tau_i \rangle$ approaches the eddy turnover time; and $\langle \tau_i \rangle$ approaches particle response time τ_p in the limit of $St \to \infty$.

This new multiscale interaction timescale $\langle \tau_i \rangle$ is incorporated in the interphase TKE transfer terms of Models I and II. It is found that for particle-laden isotropic turbulence, the predicted steep decay of TKE at the beginning of simulation is improved. The incorrect variation of TKE decay with increasing particle Stokes numbers in Model I is also eliminated by using the time scale $\langle \tau_i \rangle$. The predictions from EEM shows satisfactory agreement with the DNS results for particle-laden isotropic turbulence.

For more complicated flow cases like the homogeneous particle-laden shear flow, the model predictions can be further improved if the dissipation rate in fluid phase is modeled with more accuracy. A difficulty that is encountered in shear flows is that the detailed budget of terms

in the TKE equation is not available from existing DNS studies.

EEM is a simple model, but it has a clear physical interpretation, and it gives reasonable trends with the important non-dimensional parameters of particle–laden turbulent flow such as particle Stokes number. Although many fundamental issues need to be addressed for this class of two–phase turbulence models—including realizability [Schumann (1977)] and the assumption of local isotropy of small scale motions—the EEM model can still be a useful engineering tool for CFD simulation of particle–laden turbulent flows.

CHAPTER 4. CONSISTENT MODELING OF INTERPHASE TURBULENT KINETIC ENERGY TRANSFER IN PARTICLE-LADEN TURBULENT FLOWS

This chapter describes a mathematical constraint that models of particle–laden turbulent flow must obey, so that they can be meaningfully compared with emerging high-fidelity numerical simulation [Yusof (1996); Bagchi and Balachandar (2004, 2003); Ten Cate et al. (2004); Legendre et al. (2006)] and experiments [Hwang and Eaton (2006a,b)] [1]. The constraint associated with the mean momentum equation for a multiphase flow system is that the mean interphase momentum transfer is conservative. This constraint is nothing but Newton's third law reflected in the mean momentum equation. The constraint on mean momentum equation also should be reflected in the second-moment equation for particle–laden turbulence. This chapter derives a constraint on terms in the equation governing the evolution for the second-moments of velocity for particle–laden turbulent flow in the Eulerian–Eulerian approach.

4.1 Introduction

Particle–laden turbulent flows are ubiquitous in nature and industrial processes. The conservation of mass, momentum and energy in the two phases can be described in an average sense using a statistical approach called the two–fluid theory [Drew and Passman (1999)]. Since the resulting equations describe both phases in an Eulerian frame, the approach is also referred to as the Eulerian–Eulerian approach. Transport equations for the second moments of the velocity in both phases have also been derived to describe the fluctuations in the particle and fluid velocities. As in statistical models of single-phase turbulence, these equations contain

[1] This chapter is adapted from Phys. Fluids 19, 085101 (2007).

unclosed terms that need to be modeled. Two important unclosed terms are the interphase transfer of turbulent kinetic energy, and the dissipation rate of turbulent kinetic energy in the fluid phase. This chapter describes a mathematical constraint that models for these terms must obey, so that they can be meaningfully compared with emerging high-fidelity direct numerical simulations [Ten Cate et al. (2004); Bagchi and Balachandar (2003, 2004)] and experiments [Hwang and Eaton (2004, 2006a,b)].

For particle–laden flows with non-negligible mass loading, the interphase transfer of momentum must be accounted for, and it manifests itself as the mean interphase momentum transfer term in the averaged equations of the two–fluid theory. A constraint associated with mean momentum equation for particle–laden flows is that the mean interphase momentum transfer is conservative, i.e., equal and opposite in both phases. This constraint is nothing but Newton's third law reflected in the mean momentum equation. It turns out that a similar constraint appears in the velocity second-moment equations for particle–laden turbulence. In this chapter we derive this constraint and explore its implications for some existing models.

An important limiting case of turbulent multiphase flows is statistically homogeneous isothermal particle–laden turbulent flow evolving in a zero–gravity environment. If gravity is absent and the mean velocity fields are homogeneous, the mean pressure gradient is zero and the mean momentum equation system results in the trivial solution of zero mean velocity in each phase, which implies a zero mean slip velocity [Drew and Passman (1999); Subramaniam (2002); Xu and Subramaniam (2006)]. Collisions are assumed to be elastic and therefore there is no energy loss through collisions. In this case, the evolution of second–moments of fluctuating velocity is solely influenced by interphase turbulent kinetic energy (TKE) transfer and viscous dissipation in the fluid phase (without the additional terms arising from mean velocity gradients). The governing equations for this limiting case in the Eulerian–Eulerian approach are [Subramaniam (2003); Xu and Subramaniam (2006)]:

$$\alpha_f \rho_f \frac{dk_f}{dt} = \left\langle u_i''^{(f)} M_i^{(f)} \right\rangle + \left\langle u_i''^{(f)} \frac{\partial \left(I_f \tau_{ki} \right)}{\partial x_k} \right\rangle, \tag{4.1}$$

$$\alpha_p \rho_p \frac{dk_p}{dt} = \left\langle u_i''^{(p)} M_i^{(p)} \right\rangle \tag{4.2}$$

where the turbulent kinetic energy (TKE) in the fluid and particle phase are denoted k_f and

k_p, respectively. The volume fraction of the fluid phase and particle phase are denoted α_f and α_p, respectively, with $\alpha_p = 1 - \alpha_f$. The thermodynamic density in each phase is constant, with ρ_f denoting the fluid phase density, and ρ_p denoting the particle phase density.

The first term on the right hand side of Eq. 4.1, $\left\langle u_i''^{(f)} M_i^{(f)} \right\rangle$ is the interphase TKE transfer term and the second term $\left\langle u_i''^{(f)} \frac{\partial \left(I_f \tau_{ki} \right)}{\partial x_k} \right\rangle$ is the covariance of fluctuating velocity in the fluid phase $u_i''^{(f)}$ with the gradient of the stress in the fluid phase (where $I_f(\mathbf{x}, t)$ is the indicator function of fluid phase at $(\mathbf{x}, t)$).

The fluctuating velocity in phase β ($\beta = f, p$) is defined as the difference between the velocity field at that point and the mass-averaged mean velocity in the β^{th} phase:

$$u_i''^{(\beta)} \equiv U_i - \left\langle \tilde{U}_i^{(\beta)} \right\rangle, \tag{4.3}$$

where the mass-averaged mean velocity in the β^{th} phase is defined as

$$\left\langle \tilde{U}_i^{(\beta)} \right\rangle \equiv \frac{\langle \rho I_\beta U_i \rangle}{\langle \rho I_\beta \rangle}. \tag{4.4}$$

The term $\left\langle u_i''^{(f)} \frac{\partial \left(I_f \tau_{ki} \right)}{\partial x_k} \right\rangle$ is usually modeled as the dissipation rate of TKE in the fluid phase. The corresponding term in the solid phase is neglected since collisions between particles are assumed to be elastic.

The interphase momentum transfer terms are denoted as $M_i^{(f)}$ and $M_i^{(p)}$ in the fluid and particle phase, respectively. For flows with no interphase mass transfer, the interphase momentum transfer term $M_j^{(\beta)}$ in phase β is given by

$$M_i^{(\beta)} \equiv -\tau_{ji} \frac{\partial I_\beta}{\partial x_j}. \tag{4.5}$$

The interphase momentum transfer term can be simplified by using the following expression for the gradient of the particle indicator function [Drew and Passman (1999)]

$$\frac{\partial I_\beta}{\partial x_j} = -n_j^{(\beta)} \delta(\mathbf{x} - \mathbf{x}_I), \tag{4.6}$$

where $\mathbf{n}^{(\beta)}$ is the unit normal at the interface that points outward with respect to phase β, and $\delta(\mathbf{x} - \mathbf{x}_I)$ is the Dirac delta function located at the interface. Substituting Eq. 4.6 into Eq. 4.5 results in the following expression for the interphase momentum transfer term

$$M_i^{(\beta)} = \tau_{ji} n_j^{(\beta)} \delta \left(\mathbf{x} - \mathbf{x}_I \right), \tag{4.7}$$

which shows that it represents the contribution to momentum transfer arising from the fact that the interface located at $\mathbf{x}_I$ can support a stress difference. It is clear from Eq. 4.7 that the interphase momentum transfer term is non-zero only at the interface. Now using Eq. 4.7 the interphase TKE transfer term can be represented as

$$\langle u_i''^{(\beta)} M_i^{(\beta)} \rangle = \langle u_i''^{(\beta)} \tau_{ji} n_j^{(\beta)} \delta\left(\mathbf{x} - \mathbf{x}_I\right) \rangle, \tag{4.8}$$

which reveals that the interphase TKE transfer term is also non-zero only at the interface.

In this report, we show that in the limiting case of zero mean velocity, the interphase TKE transfer between fluid and particle phase is conservative, i.e., equal in magnitude and opposite in sign. This constraint arises because of the interface boundary condition requiring the velocities in both phases to be the same at the interface, and because the instantaneous momentum transfer between the phases is equal and opposite in sign. It follows from this constraint that the *mixture* turbulent kinetic energy is solely determined by the dissipation rate of fluid phase under the condition of zero mean velocity and elastic (non-dissipative) particle collisions.

For the limiting case of homogeneous particle–laden turbulent flow, models of particle–laden turbulent flows have the following general form:

$$\alpha_f \rho_f \frac{dk_f}{dt} = \Pi_{k_f} - \varepsilon_f \tag{4.9}$$

$$\alpha_p \rho_p \frac{dk_p}{dt} = \Pi_{k_p} \tag{4.10}$$

where Π_{k_f} is the model for the interphase TKE transfer in fluid phase $\left\langle u_i''^{(f)} M_i^{(f)} \right\rangle$, and Π_{k_p} is the model for $\left\langle u_i''^{(p)} M_i^{(p)} \right\rangle$. Typically multiphase turbulence models are validated by comparing model predictions with experimental results or direct numerical simulation (DNS) data. The advantage in using DNS data for model validation is that a term–by–term comparison is possible by examining the budgets of the TKE equations. A meaningful term–by–term comparison of multiphase model predictions with DNS data requires a consistent definition of the interphase TKE transfer terms and the dissipation rate, in the model and DNS. This becomes even more important in light of the fact that there is more than one approach to performing DNS of particle–laden turbulent flows.

Most DNS of particle–laden turbulent flow [Elghobashi and Truesdell (1993); Boivin et al. (1998); Sundaram and Collins (1999); Ahmed and Elghobashi (2000, 2001); Mashayek and Taulbee, (2001); Mashayek and Taulbee (2002); Ferrante and Elghobashi (2003)] use the point–particle approximation on the basis that the size of particles simulated is usually smaller than the Kolmogorov scale of turbulence. This approximation is convenient is because a true direct simulation of particle–laden turbulent flow that imposes the exact boundary conditions at each particle's surface, and resolves the boundary layer around each particle, is computationally expensive. In the point–particle approximation the momentum transfer between the fluid and particle is modeled as a point source. In a two-way coupled DNS of particle-laden turbulent flow using the point–particle approximation, the force exerted by a particle on surrounding flow field needs to be interpolated as the interphase momentum transfer to the fluid momentum equation using kernel averaging. This instantaneous interphase momentum transfer term results in an implied interphase TKE transfer that appears in the evolution equations for the second moments of fluctuating velocity (cf. Eqs. 4.1–4.2). The dissipation rate in the fluid is calculated in these DNS based on the gradients of the fluid velocity field that solves the fluid momentum equation augmented by the interphase momentum transfer term [Sundaram and Collins (1999)]. We denote the fluid phase dissipation rate in DNS studies that employ the point particle approximation as ε_f^{pp}. This dissipation rate differs from the single–phase turbulence dissipation rate ε_f^1 due to the modification of the turbulent flow field arising from the momentum transfer from the point–particles. When validating particle–laden turbulent flow models with point–particle DNS data, it is important to interpret the comparison of model to DNS keeping in mind the definition of the interphase TKE transfer and dissipation terms in both approaches. The choice of initial dissipation rate can dramatically affect model predictions [Xu (2004)], so it is important to compare the appropriate dissipation.

Direct numerical simulations of particle–laden turbulent flow with no-penetration and no-slip boundary conditions imposed at the surface of each particle are emerging [Ten Cate et al. (2004); Bagchi and Balachandar (2003, 2004)], With increasing computational power, using these DNS the boundary layer around each particle can be resolved. We denote these sim-

ulations "true" DNS. Clearly it is desirable that definition of interphase TKE transfer and dissipation rate in the models be consistent with true DNS. The dissipation rate in true DNS will be different from that obtained from point-particle DNS, since the high velocity gradients found in the boundary layer around each particle can be fully resolved in true DNS. In this study, the dissipation rate from true DNS is denoted ε_f^t.

Recent highly–resolved particle image velocimetry (PIV) measurements of homogeneous turbulence [Hwang and Eaton (2004, 2006a,b)] laden with small particles $d_p \sim \eta$ (Kolmogorov length scale), reveal higher turbulent kinetic energy reduction (up to 40%) at the mass loading of 0.3. The earlier experiments [Parthasarathy and Faeth (1990); Mizukami et al. (1992); Chen et al. (2000)] investigating the stationary homogeneous turbulence self–induced by settling particles in stagnant water and air, reported small dissipation rate and relative lower turbulence generation in term of turbulence intensities. These studies reveal that resolving the boundary layers around the particles has a significant impact on the dissipation rate, which in turn directly affects the TKE evolution in both phases. The earlier direct numerical simulations with point–particle approximation [Boivin et al. (1998); Sundaram and Collins (1999); Elghobashi and Truesdell (1993)] had considerably underestimated the reduction rate in turbulent kinetic energy for homogeneous turbulence comparing with the PIV measurements results [Hwang and Eaton (2006b)]. These PIV results suggest that the quantitative prediction of true DNS could be different from DNS with point-particle approximations, although it appears likely that the trends of the dissipation rate and TKE with non-dimensional parameters such as Stokes number and mass loading are still reasonably predicted using point-particle DNS.

As true DNS becomes commonplace due to rapid increase in computational power, and with more high-resolution PIV results for particle–laden turbulence, detailed budgets for particle–laden turbulence will soon be readily available. Hence, multiphase turbulence models will be required to satisfy more stringent tests arising from comparison of budgets with true DNS and high-resolution PIV. Those models that obey the inherent mathematical constraints arising from the exact equations will compare more favorably with true DNS or high–resolution experimental data.

This chapter derives one such mathematical constraint, the conservation of interphase TKE transfer in homogeneous particle–laden turbulence. In the following section, the conservation principle is derived using the Eulerian–Eulerian approach. In Section III the implications of this principle for multiphase turbulence models are examined. Section IV addresses the issue of comparing the interphase TKE transfer and dissipation rate terms in models to DNS. The principal conclusions of the study are summarized in the final section.

4.2 The Principle of Conservative Interphase TKE Transfer

The evolution of TKE in the fluid and particle phase for the limiting case of statistically homogeneous, particle–laden turbulent flow in zero gravity is given by Eqs. 4.1–4.2 in Section 4.1. The terms representing interphase TKE transfer in the evolution equation for k_β in Eqs. 4.1– 4.2 are $\left\langle u_i''^{(\beta)} M_i^{(\beta)} \right\rangle$, which are unclosed and must be modeled. The interphase TKE transfer term is the expectation of $u_i''^{(\beta)}$, the fluctuating velocity in phase β, times the interphase momentum transfer term $M_i^{(\beta)}$ (cf. Eq. 4.5). Since $M_i^{(\beta)}$ is non-zero only at the interface, so is Π_{k_β}.

The TKE of the two-phase mixture e_m is defined as

$$e_m \equiv \alpha_f \rho_f k_f + \alpha_p \rho_p k_p. \tag{4.11}$$

For constant–density homogeneous particle–laden turbulence, the mixture TKE e_m evolution is obtained by adding Eqs. 4.1 and 4.2 to obtain:

$$\frac{de_m}{dt} = \left\langle u_i''^{(f)} \frac{\partial \left(I_f \tau_{ki} \right)}{\partial x_k} \right\rangle + \left\langle \left(u_i''^{(p)} - u_i''^{(f)} \right) M_i^{(p)} \right\rangle \tag{4.12}$$

where the fact that the instantaneous interphase momentum source in each phase is equal and opposite $M_i^{(f)} = -M_i^{(p)}$ has been used. At the fluid-solid interface the instantaneous velocity in each phase is equal because of the boundary conditions of no-slip and zero normal relative velocity.

For the zero mean slip velocity case considered here, the difference in the fluctuating velocity in each phase is the same as the difference in the instantaneous velocity $\mathbf{U}$,

$$u_i''^{(p)} - u_i''^{(f)} = \left(U_i - \left\langle \tilde{U}_i^{(p)} \right\rangle \right) - \left(U_i - \left\langle \tilde{U}_i^{(f)} \right\rangle \right) = 0 \tag{4.13}$$

which is zero at the interface. Hence, it follows that the interphase TKE transfer terms should be conservative:

$$\left\langle u_i''^{(p)} M_i^{(p)} \right\rangle + \left\langle u_i''^{(f)} M_i^{(f)} \right\rangle = \left\langle \left(u_i''^{(p)} - u_i''^{(f)} \right) M_i^{(p)} \right\rangle = \left\langle (U_i - U_i) M_i^{(p)} \right\rangle = 0. \tag{4.14}$$

From this principle of conservative interphase TKE transfer it follows that if there is zero dissipation in the particle phase, then the evolution of the mixture TKE is determined by the fluid phase dissipation rate only:

$$\frac{de_m}{dt} = \left\langle u_i''^{(f)} \frac{\partial \left(I_f \tau_{ki} \right)}{\partial x_k} \right\rangle. \tag{4.15}$$

Although Eq. 4.13 is intuitive and essentially correct, the simple derivation presented above does not reveal certain assumptions that are needed to establish the conservation principle in Eq. 4.14. A detailed derivation is presented in the following subsection for completeness, but the reader may proceed to the following section without loss of continuity.

4.2.1 Detailed Derivation of the Conservation Principle

There are two important aspects of this problem that the simple derivation in Eqs. 4.13-4.14 does not explicitly account for. The first is that the instantaneous velocity U_i and the fluctuating velocities in each phase $u_i''^{(f)}$ and $u_i''^{(p)}$ are *random fields* that are parametrized in space $\mathbf{x}$ and time t. Yet the equality in Eq. 4.13 holds only at the boundary surfaces of the fluid-solid interface. Secondly, the expectation symbol $\langle \cdot \rangle$ needs to be interpreted properly depending on whether the quantity within the angle brackets is surface–measurable or volume–measurable. As noted earlier, the interphase TKE transfer terms $\left\langle u_i''^{(\beta)} M_i^{(\beta)} \right\rangle = \left\langle u_i''^{(\beta)} \tau_{ji} n_j \delta \left(\mathbf{x} - \mathbf{x}_I \right) \right\rangle$ are nonzero only at the fluid-solid interface. As we shall see, such terms are only surface–measurable, and they have zero volume measure.

We now present a more rigorous derivation of the conservation principle that fully accounts for these important aspects of the problem. This derivation reveals the assumptions inherent in the simple derivation presented earlier in the section. Since dimensionality of the parameter space is not important, we consider random fields indexed by only one variable x, i.e., we

consider random processes for simplicity. Also we consider only one component of the vector velocity field for simplicity.

Let $U(x)$ be a random process that represents the 1-component of the instantaneous velocity field U_i in the fluid phase, as depicted in Fig. 4.1. Solid particles are located randomly in space x, with their indicator function $I_p(x)$ as shown in Fig. 4.1. The presence of the particles defines the interface locations $\delta(x - x_I)$ that induce a surface process $U_\sigma(x_I)$, which is a new random process defined by the values the $U(x)$ takes at the interface locations $x = x_I$.

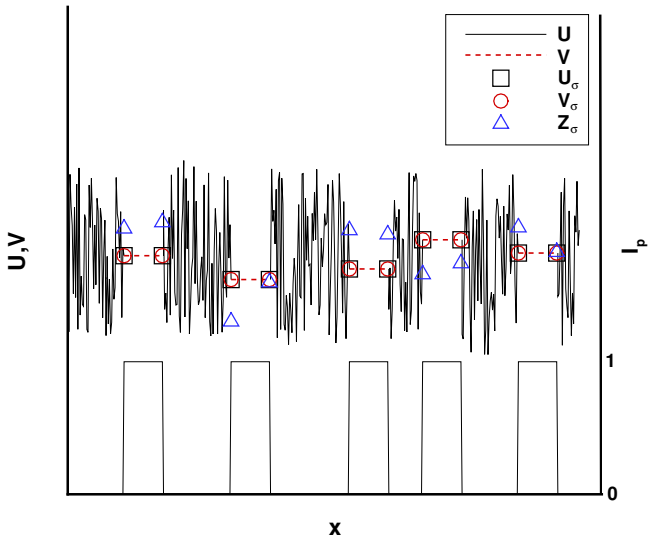

Figure 4.1 Sketch showing a realization of random processes corresponding to the 1–component of fluid velocity U, and the 1–component of particle velocity V in a one–dimensional parameter space x. There are five solid particles in this realization, whose boundaries define the ten fluid-solid interface locations. These interfaces induce the surface processes U_σ and V_σ. The interphase momentum transfer term is a pure surface process denoted Z_σ.

Similarly the instantaneous velocity field in the particle phase is denoted $V(x)$. Again the interface locations induce a surface process $V_\sigma(x_I)$, which is defined by the values $V(x)$ takes at the interface locations $x = x_I$. Because the particles are rigid, it follows that V and V_σ are

identical, and so are their probability distributions, which we write as:

$$V \stackrel{D}{=} V_\sigma. \tag{4.16}$$

Note that in general U and U_σ will not be identically distributed. The interphase momentum transfer term $M_i^{(p)}$ is a pure surface process (i.e., it is not defined anywhere else on x other than x_I), and its 1-component is denoted $Z_\sigma(x_I)$.

We distinguish between the two types of expectation that appear in the Eulerian–Eulerian averaged equations for two–phase flow. Details concerning the definitions of these measures and expectations are given in Section 4.6. For any volume–measurable flow quantity Q in phase β, we define its phase–volume mean as

$$\langle Q_\beta \rangle_v (x) \equiv \frac{\left\langle Q_\beta^v(x) \right\rangle}{\alpha_\beta(x)}. \tag{4.17}$$

Similarly for any surface–measurable flow quantity Q in phase β we define its phase–surface mean as

$$\langle Q_\beta \rangle_s (x) \equiv \frac{\left\langle Q_\beta^s(x) \right\rangle}{\sigma_\beta(x)}. \tag{4.18}$$

Clearly U_σ, V_σ and Z_σ are not volume–measurable. We first consider statistically homogeneous flows where both phase–volume means, as well as phase–surface means are independent of x. Note that this is a stronger requirement than simply requiring α_p to be independent of x. Specifically, this stronger homogeneity requires both the particle number density, as well as the particle size distribution to be homogeneous in physical space.

The interphase TKE transfer term is the covariance of fluctuating velocity with the interphase momentum transfer term, and the latter is nonzero only at the fluid-solid interface. We define the velocity fluctuation in fluid phase U' with respect to the phase–volume mean velocity as

$$U'(x) \equiv U(x) - \langle U \rangle_v (x). \tag{4.19}$$

For the limiting case of zero mean velocity in both phases considered in this study, we have $\langle U \rangle_v = 0$, and hence $U'(x) = U(x)$. We now evaluate the term corresponding to Π_{k_f} as

$$-\langle U' Z_\sigma \rangle_s = -\langle U Z_\sigma \rangle_s = -\langle U_\sigma Z_\sigma \rangle_s, \tag{4.20}$$

where we have used $M_1^{(f)} = -M_1^{(p)} = -Z_\sigma$, and the definition that at $U = U_\sigma$ at $x = x_I$.

The fluctuating particle velocity at the interface V'_σ is identical to the instantaneous particle velocity at the interface V_σ, if the mean particle velocity $\langle V \rangle_v = 0$ is zero. In order to establish

$$\Pi_{k_f} = -\Pi_{k_p}$$

we evaluate the term corresponding to Π_{k_p} as

$$\langle V' Z_\sigma \rangle_s = \langle V Z_\sigma \rangle_s = \langle V_\sigma Z_\sigma \rangle_s. \tag{4.21}$$

Since at the interface the velocity boundary condition requires instantaneous velocities to be equal, we have

$$U_\sigma = V_\sigma, \tag{4.22}$$

which establishes

$$\Pi_{k_f} = -\langle U_\sigma Z_\sigma \rangle_s = -\langle V_\sigma Z_\sigma \rangle_s = -\Pi_{k_p}. \tag{4.23}$$

The interphase TKE terms for this limiting case are equal in magnitude, and opposite in sign. Thus, the principle of conservative interphase TKE transfer in Eq. 4.14 is rigorously established here.

4.2.1.1 Extensions

This derivation shows that the result holds for statistically homogeneous flows (where both phase–volume means and phase–surface means are homogeneous) with zero mean velocity in both phases. The result holds for both monodisperse as well as polydispersed particle–laden turbulent flows, provided they satisfy the statistical homogeneity requirement on the number density and size distribution. If there is nonzero mean slip, then the conservation principle is modified to read

$$\left\langle u_i''^{(f)} M_i^{(f)} \right\rangle + \left\langle u_i''^{(p)} M_i^{(p)} \right\rangle = \left(\langle U \rangle_v - \langle V \rangle_v \right) \langle Z_\sigma \rangle_s, \tag{4.24}$$

which holds provided

$$\langle \langle U \rangle_v \rangle_s = \langle U \rangle_v, \tag{4.25}$$

$$\langle \langle V \rangle_v \rangle_s = \langle V \rangle_v. \tag{4.26}$$

These relationships hold if the phase–volume means $\langle U \rangle_v (x)$ and $\langle V \rangle_v (x)$ are statistically homogeneous in x, and if the phase–surface measure $\sigma_\beta(x)$ is also statistically homogeneous in x. The result can be extended to general inhomogeneous flows provided the velocity statistics are locally homogeneous on the scale of the particle size.

4.3 Implications for Multiphase Turbulence Models

The implications of conservative interphase TKE transfer for some multiphase turbulence models are now examined. The multiphase turbulence models considered are: (i) Ahmadi and Ma (1990); Ma and Ahmadi (1990), (ii) Equilibration of Energy Model (EEM) [Xu and Subramaniam (2006)], and (iii) Simonin (1996b).

In Ahmadi's model, the governing equations for k_f and k_p in homogeneous particle–laden turbulent flows simplify to

$$\alpha_f \rho_f \frac{dk_f}{dt} = 2D_0 (k_p - ck_f) - \alpha_f \rho_f \varepsilon_f, \tag{4.27}$$

$$\alpha_p \rho_p \frac{dk_p}{dt} = 2D_0 (ck_f - k_p). \tag{4.28}$$

The evolution equation for mixture energy results from adding Eqs. 4.27 and 4.28

$$\frac{de_m}{dt} = 2D_0 (ck_f - k_p) + 2D_0 (k_p - ck_f) - \alpha_f \rho_f \varepsilon_f = -\alpha_f \rho_f \varepsilon_f \tag{4.29}$$

This shows that Ahmadi's model satisfies the principle of conservative interphase TKE transfer.

For the Equilibration of Energy Model (EEM) [Xu and Subramaniam (2006)], the simplified equations for homogeneous particle–laden turbulent flow are:

$$\frac{dk_f}{dt} = -\frac{1}{\tau_\pi} [C_2 k_f - (1 - C_2)\phi k_p] - \varepsilon_f, \tag{4.30}$$

$$\frac{dk_p}{dt} = -\frac{1}{\tau_\pi} \left[(1 - C_2) k_p - \frac{C_2}{\phi} k_f \right]. \tag{4.31}$$

The time scale τ_π is the interphase TKE transfer time scale and C_2 is a model constant. Adding Eqs. 4.30 and 4.31, the governing equation for the specific mixture energy e_m is obtained:

$$\frac{de_m}{dt} = -\alpha_f \rho_f \varepsilon_f. \tag{4.32}$$

The model for interphase TKE transfer in EEM also obeys the principle of conservative interphase TKE transfer.

Simonin's model for k_f and k_p evolution in homogeneous particle–laden turbulence is

$$\alpha_f \rho_f \frac{dk_f}{dt} = \alpha_p \rho_p \frac{1}{\tau_{12}^F} (k_{fp} - 2k_f) - \alpha_f \rho_f \varepsilon_f \tag{4.33}$$

$$\alpha_p \rho_p \frac{dk_p}{dt} = -\alpha_p \rho_p \frac{1}{\tau_{12}^F} (2k_p - k_{fp}) \tag{4.34}$$

The resulting evolution equation for the specific mixture energy e_m is

$$\frac{de_m}{dt} = 2\alpha_p \rho_p \frac{1}{\tau_{12}^F} (k_{fp} - k_f - k_p) - \alpha_f \rho_f \varepsilon_f. \tag{4.35}$$

Here the interphase TKE transfer terms in fluid and particle phase are not conservative. Of the three multiphase turbulence models considered here, Ahmadi's model and EEM respect the principle of conservative interphase TKE transfer, whereas Simonin's model does not. We now examine the consequence of this observation in terms of meaningful comparison of these models to DNS.

4.4 Comparison of Models to DNS

Since Ahmadi's model and EEM satisfy the principle of conservative interphase TKE transfer, their model expressions for Π_{k_β} can be directly compared with true DNS data for interphase TKE transfer. It is also consistent to then compare the Ahmadi and EEM models for $\alpha_f \rho_f \varepsilon_f$, as they appear in Eqs. 4.29 and 4.32, with true DNS data for the exact evolution of e_m (Eq. 4.15). Since Simonin's model does not satisfy the principle of conservative interphase TKE transfer, its model expression for Π_{k_β} cannot legitimately be compared with true DNS data for interphase TKE transfer. It is also not clear what true DNS quantity is modeled by Simonin's expression for ε_f, as it appears in Eq. 4.35.

Most of the DNS data available for particle–laden turbulent flow is based on simulations that use the point-particle approximation, and these are widely used for model validation. Since the exact velocity boundary condition at each particle surface is not imposed in the point–particle approximation, it is useful to check if the implied DNS model for interphase

TKE transfer satisfies the conservation principle. Note that true DNS satisfies the principle of conservative interphase TKE transfer automatically, since the exact velocity boundary condition is imposed at each particle surface.

Here we use the governing equations from Sundaram and Collins (1999) for homogeneous particle–laden turbulence (with zero mean velocity in both phases) as an example of a DNS that uses the point particle approximation. The governing equations for total TKE in fluid phase T_f, particle phase T_p and mixture energy T_t are:

$$\frac{dT_f}{dt} = -\sum_{n=1}^{N_p} \frac{m_p \mathbf{u}(\mathbf{x}^n) \cdot [\mathbf{u}(\mathbf{x}^n) - \mathbf{v}^n]}{\tau_p} - \phi_v, \tag{4.36}$$

$$\frac{dT_p}{dt} = \sum_{n=1}^{N_p} \frac{m_p \mathbf{v}^n \cdot [\mathbf{u}(\mathbf{x}^n) - \mathbf{v}^n]}{\tau_p}, \tag{4.37}$$

$$\frac{dT_t}{dt} = -\phi_v - \phi_p, \tag{4.38}$$

where ϕ_v and ϕ_p are defined as

$$\phi_v = \int_{\mathcal{V}} \rho_f \varepsilon_f dV, \tag{4.39}$$

$$\phi_p = \sum_{n=1}^{N_p} \frac{m_p \left[\mathbf{u}(\mathbf{x}^n) - \mathbf{v}^n\right]^2}{\tau_p}. \tag{4.40}$$

In the above equations the total energy (T_p, T_f, T_t) is an extensive property since it is integrated over the entire flow domain $\mathcal{V}$. Here $\mathbf{x^n}$ and $\mathbf{v}^n$ denote the instantaneous position and velocity of the n^{th} particle center, and $\mathbf{u}(\mathbf{x}^n)$ represents the fluid velocity at position $\mathbf{x}^n$. The total number of particles is N_p, and τ_p is the particle momentum response time.

The first terms on right-hand-side of Eqs. 4.36 and 4.37, which represent the interphase TKE transfer between fluid and particle phase, do not sum to zero. Therefore, the interphase TKE transfer terms in point particle DNS are not conservative. The two terms that contribute to the evolution of the mixture energy T_t are: (i) the fluid phase dissipation rate ϕ_v, where $\varepsilon_f = 2\nu \langle s_{ij} s_{ji} \rangle$ is obtained from the gradients of the fluid velocity field, and (ii) the energy losses due to drag at the particle interfaces, ϕ_p. The dissipation rate ε_f in ϕ_v is the same as ε_f^{pp} introduced in Section I. The dissipation rate in true DNS ε_f^t, which determines the evolution of mixture energy, is different from ε_f^{pp}, and this difference is presumably accounted

for in point–particle DNS by the quantity ϕ_p, which scales as the square of the instantaneous relative velocity between the two phases.in Eq. 4.40. Therefore, comparing Eq. 4.38 with Eq. 4.15 reveals that $-(\phi_v + \phi_p)$ is a model for the right hand side of Eq. 4.15 integrated over the flow domain. Whether the point particle DNS model for evolution of mixture energy that is described by Eq. 4.38 is accurate has yet to be verified by true DNS.

Clearly it is not meaningful to compare conservative models of interphase TKE transfer, such as Ahmadi's or EEM, with point–particle DNS data for the interphase TKE transfer term. Also in light of Eqs. 4.29 and 4.32, the Ahmadi and EEM models for ε_f should not be compared directly with the point–particle DNS dissipation rate ε_f^{pp}. Instead, the integrated modeled mixture energy evolution equations (Eqs. 4.29 and 4.32) should be directly compared to Eq. 4.38. In other words, the EEM and Ahmadi ε_f are models for the sum of ε_f^{pp} and the dissipation due to the relative velocity difference at the location of each particle (that appears in ϕ_p, which is defined in Eq. 4.40). One plausible identification of the terms in Simonin's model for comparison with point–particle DNS is ε_f should be compared with ε_f^{pp}, and the Simonin model for $\Pi_{k_f} - \Pi_{k_p}$ corresponds to the term in Eq. 4.39 that scales as the square of the instantaneous relative velocity difference.

4.5 Summary and Conclusion

This study shows that for the limiting case of statistically homogeneous particle–laden turbulent flow with zero mean velocity in both phases, the interphase TKE transfer terms in the evolution of TKE in fluid and particle phases are equal and opposite in sign. The result holds under the following conditions:

1. the particle phase consists of rigid particles with constant thermodynamic density,

2. the flow is statistically homogeneous and the phase–volume mean and phase–surface mean of all flow quantities are statistically homogeneous,

3. the mean velocity in both phases is zero.

This conservative nature of the interphase TKE transfer term implies that the *exact* evolution equation for the mixture TKE does not depend on the interphase TKE transfer terms (cf. Eq. 4.15). The result can be extended in a slightly modified form to flows with nonzero mean slip velocity if the additional conditions expressed in Eqs. 4.25 and 4.26 hold. The result can also be extended to general inhomogeneous flows provided the velocity statistics are locally homogeneous on the scale of particle size.

This principle of conservative interphase TKE transfer has implications for single-point Eulerian second–moment closure models of particle–laden turbulent flow. Three models—Simonin (1996b), Ahmadi and Ma (1990), and the Equilibrium of Energy model [Xu and Subramaniam (2006)]—are examined to see if they obey this principle. Ahmadi's model and EEM satisfy the principle of conservative interphase TKE transfer, but Simonin's model does not.

The significance of the constraint expressed by the principle of conservative interphase TKE transfer manifests itself when performing term–by–term comparison of models with DNS data. We distinguish between true DNS, where the exact boundary conditions on velocity are imposed at each particle's surface, and point–particle DNS where the particles are point sources of momentum. Models for the interphase TKE transfer term that obey the conservation principle can be legitimately compared with data from true DNS. For these models, the modeled fluid dissipation rate solely determines the mixture TKE evolution (cf. Eqs. 4.29, 4.32), and it can be consistently compared with true DNS data for the exact mixture TKE evolution equation (Eq. 4.15). It is found that point–particle DNS do not satisfy the principle of conservative interphase TKE transfer. Therefore, it is not meaningful to compare conservative models for the interphase TKE transfer term with point–particle DNS data. Rather, when comparing predictions of a multiphase turbulence model that satisfies conservative interphase TKE transfer with point–particle DNS data, the mixture TKE equations should be matched. In other words, the term $\alpha_f \rho_f \varepsilon_f$ in Eqs. 4.29 and 4.32 that contains the modeled dissipation rate should be compared (after integration over the flow domain) with $-(\phi_v + \phi_p)$ in Eq. 4.38, which represents the sum of ε_f^{pp} and the additional dissipation which is assumed to scale as

the square of the relative velocity between fluid and particle phases.

4.6 Measures for Two–phase Flows

As discussed in Section 4.2, there are two types of expectations that arise when deriving averaged equations in the Eulerian–Eulerian approach: the phase–volume mean and the phase–surface mean. This is because quantities like the interphase momentum transfer are not volume–measurable because they are defined only on the particle surface and have zero volume measure. In other words, because these interface quantities have zero volume measure one cannot construct their expectation with respect to Lebesgue measure in $\mathbb{R}^3$. On the other hand it is clear that the mean interphase momentum transfer is not zero. The resolution lies in the fact that the measure and expected value of interface quantities is different from those flow quantities defined in each phase, and this phase–surface measure and expectation needs to be unambiguously defined. Having identified the need to clearly define and distinguish between the phase–volume and phase–surface measure and expectation, we now describe the mathematical foundations needed to define these quantities.

We define a probability triple $(\Omega, \mathcal{F}, P)$ [Billingsley (1995)] where Ω is the set of all events, $\mathcal{F}$ is a σ–field and P is a probability measure that is defined on this σ–field. Define a mapping from Ω space to a flow domain $\mathcal{D}$ in Euclidean space–time $\mathcal{D} \subset \mathbb{R}^4$ which takes every event $\omega \in \Omega$ to a realization of a two–phase flow in space–time that is described by the phase indicator function $I_\beta(\mathbf{x}, t)$ and any flow property $Q(\mathbf{x}, t)$ (for example Q could be the velocity field). This unambiguously defines the ensemble of realizations.

4.6.1 Phase–volume Measure

Consider a set A in the flow domain $\mathcal{D}$. The phase volume measure of phase β denoted as $\mu_\beta(A;\omega)$, is defined as

$$\mu_\beta(A;\omega) \equiv \int_A I_\beta(\mathbf{x}, t;\omega)\, dA. \tag{4.41}$$

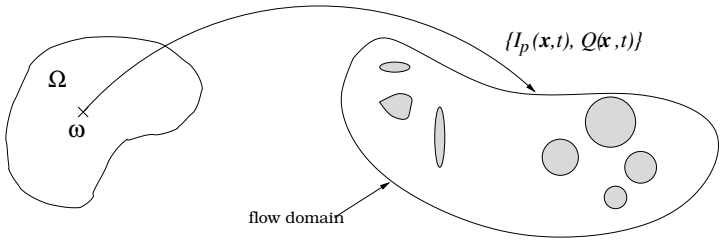

Figure 4.2 The ensemble of realizations is defined by the event space Ω. Each realization of the two–phase flow corresponds to a the mapping of an element ω in the sample space Ω to the phase indicator function $I_\beta(\mathbf{x},t)$ and flow property $Q(\mathbf{x},t)$, which are defined in the flow domain $\mathcal{D}$.

Note that this is a random measure because it depends on the realization of the two-phase flow corresponding to ω. The expected value of this random measure is

$$\langle \mu_\beta(A) \rangle = \int_\Omega \mu_\beta(A;\omega)\, dP_\omega = \int_\Omega \int_A I_\beta(\mathbf{x},t;\omega)\, dA\, dP_\omega, \tag{4.42}$$

which is obtained by integrating with respect to the probability measure defined on Ω.

Because the integrations commute:

$$\begin{aligned} \langle \mu_\beta(A) \rangle &= \int_A \int_\Omega I_\beta(\mathbf{x},t;\omega)\, dP_\omega\, dA \\ &= \int_A \langle I_\beta \rangle\, dA, \end{aligned} \tag{4.43}$$

where $\langle I_\beta \rangle$ is the expected value of the indicator function that is defined as

$$\langle I_\beta \rangle (\mathbf{x},t) \equiv \int_\Omega I_\beta(\mathbf{x},t)\, dP_\omega. \tag{4.44}$$

If $\langle I_\beta \rangle (\mathbf{x},t)$ exists then $\langle \mu_\beta(A) \rangle$ is absolutely continuous with respect to Lebesgue measure[2], and it can be written as the integral of a density over the set A. This density is nothing but the volume fraction $\alpha_\beta(\mathbf{x},t)$ of phase β. If the volume occupied by the phase β is denoted by V_β, and is given by

$$V_\beta \equiv \int_{\mathcal{D}} I_\beta(\mathbf{x},t)\, d\mathbf{x},$$

then it follows that its expected value is

$$\langle V_\beta(t) \rangle = \int_{\mathcal{D}} \langle I_\beta \rangle (\mathbf{x},t) d\mathbf{x} = \int_{\mathcal{D}} \alpha_\beta(\mathbf{x},t)\, d\mathbf{x},$$

[2]This is reasonable for particle two–phase flows where this measure is non-atomic except in pathological cases.

where $\alpha_\beta(\mathbf{x}, t)$ is the volume fraction occupied by phase β at location $\mathbf{x}$ and time t.

The phase–volume measure of flow quantity Q in phase β is denoted as

$$Q_\beta^v(A;\omega) \equiv \int_A I_\beta Q \, dA. \tag{4.45}$$

Just as μ_β is a random measure, so is $Q_\beta^v(A;\omega)$. Its expectation is simply:

$$\left\langle Q_\beta^v(A) \right\rangle = \int_\Omega Q_\beta^v(A;\omega) \, dP_\omega = \int_\Omega \int_A I_\beta Q \, dA \, dP_\omega. \tag{4.46}$$

Again, because the integrations commute we have

$$\begin{aligned} \left\langle Q_\beta^v(A) \right\rangle &= \int_A \int_\Omega I_\beta Q \, dP_\omega \, dA \\ &= \int_A \left\langle I_\beta Q \right\rangle \, dA. \end{aligned} \tag{4.47}$$

If we assume that $\left\langle Q_\beta^v(A) \right\rangle$ is absolutely continuous with respect to Lebesgue measure then it can be written as the integral of a density function over the set A as:

$$\left\langle Q_\beta^v(A) \right\rangle = \int_A \left\langle Q_\beta^v \right\rangle (\mathbf{x}, t) \, d\mathbf{x} \, dt. \tag{4.48}$$

Rewriting this density of the phase–volume measure of Q as a conditional density with respect to the density of expected phase–volume measure leads to the usual "phase average" in two–fluid theory:

$$\left\langle Q_\beta \right\rangle_v (\mathbf{x}, t) = \frac{\left\langle Q_\beta^v(\mathbf{x}, t) \right\rangle}{\alpha_\beta(\mathbf{x}, t)}. \tag{4.49}$$

4.6.2 Phase–surface Measure

Consider a set A in the flow domain $\mathcal{D}$ and let S_β be the phase–surface indicator function

$$S_\beta(\mathbf{x}, t) = \delta(\mathbf{x} - \mathbf{x}_I),$$

such that $S_\beta(A)$ selects the boundary of all I_β surfaces contained within set A. The phase–surface measure of phase β is denoted $\Sigma_\beta(A;\omega)$, and is defined as:

$$\Sigma_\beta(A;\omega) \equiv \int_A S_\beta(\mathbf{x}, t) \, dA. \tag{4.50}$$

This quantity also is a random measure since it depends on the realization of the two–phase flow corresponding to ω. The expected value of this random measure is

$$\langle \Sigma_\beta(A) \rangle = \int_\Omega \Sigma_\beta(A;\omega)\, dP_\omega = \int_\Omega \int_A S_\beta(\mathbf{x},t)\, dA\, dP_\omega, \tag{4.51}$$

which is obtained by integrating with respect to the probability measure defined on Ω.

Since the integrations commute,

$$\begin{aligned} \langle \Sigma_\beta(A) \rangle &= \int_A \int_\Omega S_\beta\, dP_\omega\, dA \\ &= \int_A \langle S_\beta \rangle\, dA, \end{aligned}$$

where $\langle S_\beta \rangle$ is the expected value of the phase–surface indicator that is defined as

$$\langle S_\beta \rangle (\mathbf{x},t) \equiv \int_\Omega S_\beta(\mathbf{x},t)\, dP_\omega. \tag{4.52}$$

If $\langle S_\beta \rangle (\mathbf{x},t)$ exists then $\langle \Sigma_\beta(A) \rangle$ is absolutely continuous with respect to Lebesgue measure and it can be written as the integral of a density over the set A. This density is nothing but the interfacial area density of phase β introduced in Drew and Passman (1999), which is denoted as $\sigma_\beta(\mathbf{x},t)$ in this work.

The phase–surface measure of flow quantity Q in phase β is denoted $Q^s_\beta(A)$, and is defined as:

$$Q^s_\beta(A;\omega) \equiv \int_A S_\beta Q\, dA. \tag{4.53}$$

Note that this random measure picks out the value of Q on the β side of the interface. For example, a flow variable Q that are discontinuous on the surface, will have different values of $Q^s_\beta(A;\omega)$ for either phase on the different sides of the interface. Its expectation is simply:

$$\left\langle Q^s_\beta(A) \right\rangle = \int_\Omega Q^s_\beta(A;\omega) dP_\omega = \int_\Omega \int_A S_\beta Q\, dA\, dP_\omega. \tag{4.54}$$

Again, because the integrations commute we have

$$\begin{aligned} \left\langle Q^s_\beta(A) \right\rangle &= \int_A \int_\Omega S_\beta Q\, dP_\omega\, dA \\ &= \int_A \langle S_\beta Q \rangle\, dA. \end{aligned} \tag{4.55}$$

If $\left\langle Q_\beta^s(A)\right\rangle$ is absolutely continuous with respect to Lebesgue measure, then it can be written as the integral of a density which can be defined over the set A as:

$$\left\langle Q_\beta^s(A)\right\rangle = \int_A \left\langle Q_\beta^s\right\rangle (\mathbf{x},t)d\mathbf{x}\,dt. \tag{4.56}$$

Rewriting this density of the phase–surface measure of Q as a conditional density with respect to the density of expected phase–surface measure leads to the correct definition of the phase–surface mean:

$$\langle Q_\beta\rangle_s (\mathbf{x},t) = \frac{\left\langle Q_\beta^s(\mathbf{x},t)\right\rangle}{\sigma_\beta(\mathbf{x},t)} \tag{4.57}$$

CHAPTER 5. DIRECT NUMERICAL SIMULATION OF GAS-SOLID FLOW USING THE IMMERSED BOUNDARY METHOD

In this chapter, the formulation of the discrete-time immersed boundary method is introduced. The immersed boundary method has the advantage of simulating many spheres with low computational cost, and the pseudo-spectral scheme used here can provide high accuracy which is suitable to simulate turbulence. The ultimate goal of the direct numerical simulation using the immersed boundary method is to simulate gas-solid turbulent flows.

Even non-turbulent gas-solid suspensions that are initially homogeneous distributed, become unstable after evolving in time. The instability happens even at very low particle Reynolds number Re_p and low particle Stokes number St [Tsao and Koch (1995); Sangani et al. (1996)]. The instability associated with gas-solid suspensions makes it difficult to extract statistics from the numerical simulation results. Furthermore, the computational cost of the DNS with the immersed boundary method is prohibitively expensive. Hill et al. (2001a,b), Wylie et al. (2003), Van der Hoef et al. (2005) and other researchers studied the finite-Reynolds-number flows in a fixed bed of spheres. The drag force on the spheres and the permeability of arrays are studied.

Following these researchers, we investigate a fixed bed of spheres interacting with homogeneous turbulence. The objective of this DNS work is to develop the immersed boundary method to simulate the upstream turbulence past a fixed bed of spheres, where the effects of the sphere random configuration on the turbulence can be studied. In this work, Chapter 5 and 6 describe the development and the validation of the immersed boundary method. The results of the turbulence past a fixed bed of spheres and the implication on gas-solid turbulence models are discussed in Chapter 7.

The discrete-time immersed boundary method developed by Yusof (1996) was applied for upstream turbulence past a single stationary sphere. The numerical resolution is $132 \times 32 \times 32$; the diameter of the sphere is 10 grid points and $\kappa_{max}\eta > 1.5$. In this work, several other restrictions are considered. For example, at least one grid point should be used to resolve the boundary layer around the sphere; the fluid domain $\mathcal{L}$ should be large enough to contain the spatial correlation of fluid phase turbulence. This DNS work satisfies all the numerical requirements mentioned above, but the computational cost of this DNS work becomes much more expensive. Even for the simulation of upstream turbulence past a single sphere with the same parameters, $Re_\lambda = 20$, $Re_p = 100$ and $u'/U = 20\%$, as that reported in Yusof's work, the grid points required are at least $200 \times 200 \times 400$. With 8 bytes representation of floating point variables, the minimum memory requirement is 6.4 GB. The cluster computers generally have 4GB or 8GB memory on one computer node, therefore the parallelization of the immersed boundary solver is a necessity, and the parallelization is not for the purpose of speed-up, but to solve a problem size with the reasonable physical parameter range and also satisfy the resolution requirements. The detail of the parallelization is presented in Chapter 6.

In Chapter 5, the DNS works of gas-solid turbulent flows in the literature are reviewed in Section 5.1. The equations from Yusof (1996) are first recapitulated in Section 5.2. The numerical results from our implementation of Yusof's numerical scheme is validated with the standard drag correlation [Clift et al. (1978)] in Section 5.3. Furthermore, the grid convergence study for the steady flow past a single stationary sphere is presented to gain confidence of our implementation.

5.1 Introduction

Turbulence modulation in the particle–laden turbulent flows has been studied extensively in both numerical simulations [Elghobashi and Truesdell (1993); Sundaram and Collins (1999); Ahmed and Elghobashi (2000); Boivin et al. (2000)] and experiments [Parthasarathy and Faeth (1990); Mizukami et al. (1992); Chen et al. (2000); Yang and Shy (2005); Hwang and Eaton (2006a,b)]. It is well established that the presence of particles can increase or decrease the level

of fluid phase turbulence. In the dilute particle–laden turbulence, there are several mechanisms that contribute to the turbulence modulation, for example, the enhanced dissipation due to the presence of particles, and interphase TKE transfer between fluid and particle phases, the formation of wakes and vortices shedding behind particles [Bagchi and Balachandar (2004)]. The understanding and implication to multiphase turbulence modeling of first two effects have been discussed in details in Chapter 4. The relative importance of the these mechanisms depends on the parameter ranges of the problem, such as the particle Stokes number, particle Reynolds number, solid volume fraction, mass loading ratio and particle size d_p to turbulence length scale ratio. When the particle size is smaller than Kolmogorov length scale η, and the Reynolds number less than unity, the effects of interphase TKE transfer and the enhanced fluid dissipation rate due to presence of particles are important. For particle with moderate particle Reynolds number, the third mechanism becomes important.

Yusof (1996) used the discrete-time immersed boundary method to simulate the effects of free stream homogeneous turbulence on the drag force, wake structure, the modulation of TKE, Reynolds stress, and other fluid phase turbulence statistics. This study shows a clear picture of wake structure destabilization as upstream turbulent intensity increases, and the vorticity shedding from the particle results in a substantial increase in the turbulence level in the wake. This is also one of the first steps toward examining the hydrodynamic interaction of finite-size particles in turbulent velocity field [Koch and Hill (2001)], which is also a *true* DNS with the exact no-slip, no-penetration boundary conditions imposed on the surface of particle.

There are several true direct numerical studies [Bagchi and Balachandar (2004, 2003); Ten Cate et al. (2004); Legendre et al. (2006)] emerging recently. The direct numerical simulations by Bagchi and Balachandar (2003, 2004) study the effect of a free stream isotropic turbulence on a single particle with moderate Reynolds number using body–fitted grids. The effects of upstream turbulence and the variation of turbulence intensity on the structure of wake vortices, the wake oscillation and vortex shedding are reported with the range of particle Reynolds numbers up to 400 [Bagchi and Balachandar (2004)]. Lattice Boltzmann simulation of turbulent solid-liquid suspensions is studied by Ten Cate et al. (2004). To the author's

knowledge, this is the first true DNS with multiple particles laden in a homogeneous turbulent flow field.

The interactions between particles in a turbulent flow field, and the attenuation to fluid turbulence can be studied in a fixed bed of spheres. The effects of fluid inertia at moderate-Reynolds numbers on flows in ordered and random arrays of spheres are studied by Hill et al. (2001b), which are designed to understand the effects of fluid inertia on the sediment suspensions and fluidized beds. The study of the fixed beds of spheres with the solid volume fraction smaller than the packed bed limit is motivated by an analogy between fixed beds and high-Stokes-number suspensions. If the particle Stokes number is large, then particles will not follow small fluctuations in the surround flow field, and only have small changes to its velocity in response to the drag caused by the slip velocity. Under these conditions, the hydrodynamic interactions between particles are similar to the fixed bed of spheres [Koch and Hill (2001)]. The case of upstream homogeneous turbulence past fixed beds of spheres provides a situation in which one can study the combined effects of upstream turbulence on wake structures and vortex shedding of particles, interactions between particles and the modulation to fluid turbulence without complications of the temporal evolution of particle configuration and particle-particle collisions.

Immersed boundary method has the ability to handle moving or deforming bodies with complex surface geometry without body fitted meshes. Peskin (1977, 2002) first introduced the method to simulate blood flow inside a heart with flexible valves, where the forcing was computed by Hooke's law. Goldstein et al. (1993) applied the concept of feedback control to compute the force on the rigid immersed surface. One drawback with the method from Goldstein et al. (1993) is that spring constants in the feedback scheme need to be determined empirically. Moreover, the time step restriction imposed by the derivation of forcing severely limits the applicability of the method. The discrete-time immersed boundary method first proposed by Yusof (1996) removed the time step restriction by the use of a discrete-time derivation of forcing without any feedback control process. In this work, we use the discrete-time immersed boundary method to study the upstream turbulence past a stationary sphere.

5.2 Discrete-time Immersed Boundary Method

In this section, the governing equations and numerical scheme employed in the DNS with the discrete-time immersed boundary method are described in Yusof (1996).

5.2.1 Governing Equations

The incompressible Navier-Stokes equations in the vector form are solved in this problem,

$$\frac{\partial \mathbf{u}}{\partial t} + (\mathbf{u} \cdot \nabla)\mathbf{u} = -\frac{1}{\rho}\nabla P + \nu \nabla^2 \mathbf{u}, \tag{5.1}$$

and the pressure Poisson equation is

$$\frac{1}{\rho}\nabla^2 P = -\nabla \cdot ((\mathbf{u} \cdot \nabla)\mathbf{u}), \tag{5.2}$$

where $\mathbf{u}$ is the instantaneous velocity vector. A primitive variable, pseudo-spectral method, using Fourier transform in the y-z directions and the central finite difference in the streamwise direction, is applied to solve this problem. This also implies that periodic boundary conditions are applied in y and z directions. Either periodic boundary conditions or inflow and outflow boundary conditions can be applied in x direction. The nonlinear terms $((\mathbf{u}\cdot\nabla)\mathbf{u})$ are calculated by transforming the velocities to real space, and then transforming the products to Fourier space. This avoids the expensive convolution operation in Fourier space that would result if the nonlinear terms are calculated in Fourier space. De-aliasing is performed by phase shifting method to avoid the aliasing error in the nonlinear terms.

After performing Fourier transforms in the y-z directions, the Navier-Stokes equations become:

$$\frac{\partial \tilde{u}}{\partial t} + \tilde{S}_x = -\frac{1}{\rho}\frac{\partial \tilde{P}}{\partial x} + \nu \frac{\partial^2 \tilde{u}}{\partial x^2} - \nu(\kappa_y^2 + \kappa_z^2)\tilde{u}, \tag{5.3}$$

$$\frac{\partial \tilde{v}}{\partial t} + \tilde{S}_y = -\frac{1}{\rho}\iota\kappa_y \tilde{P} + \nu \frac{\partial^2 \tilde{v}}{\partial x^2} - \nu(\kappa_y^2 + \kappa_z^2)\tilde{v}, \tag{5.4}$$

$$\frac{\partial \tilde{w}}{\partial t} + \tilde{S}_z = -\frac{1}{\rho}\iota\kappa_z \tilde{P} + \nu \frac{\partial^2 \tilde{w}}{\partial x^2} - \nu(\kappa_y^2 + \kappa_z^2)\tilde{w}, \tag{5.5}$$

where $\tilde{u}$, $\tilde{v}$, $\tilde{w}$ and $\tilde{P}$ are the Fourier transform of the physical space velocity and pressure. The pressure Poisson equation becomes ($\iota = \sqrt{-1}$):

$$-\frac{1}{\rho}\left(\frac{\partial^2 \tilde{P}}{\partial x^2} - (\kappa_y^2 + \kappa_z^2)\tilde{P}\right) = \frac{\partial \tilde{S}_x}{\partial x} + \iota\kappa_y \tilde{S}_y + \iota\kappa_z \tilde{S}_z. \tag{5.6}$$

In Eq. 5.3—5.6, $\tilde{S}_x$, $\tilde{S}_y$ and $\tilde{S}_z$,

$$\tilde{S}_x = \mathcal{F}\left(\frac{\partial uu}{\partial x} + \frac{\partial uv}{\partial y} + \frac{\partial uw}{\partial z}\right), \tag{5.7}$$

$$\tilde{S}_y = \mathcal{F}\left(\frac{\partial vu}{\partial x} + \frac{\partial vv}{\partial y} + \frac{\partial vw}{\partial z}\right), \tag{5.8}$$

$$\tilde{S}_z = \mathcal{F}\left(\frac{\partial wu}{\partial x} + \frac{\partial wv}{\partial y} + \frac{\partial ww}{\partial z}\right), \tag{5.9}$$

are the Fourier transformed convective terms which are evaluated in the physical space. Here $\mathcal{F}$ denotes the forward Fourier transform.

Since the Fourier transform is performed on the y-z directions, the discretization in the y-z directions is to use the discrete Fourier transformed variables replacing the continuous Fourier transformed variables. For the x direction, the second-order central finite difference is used:

$$\left.\frac{\partial f}{\partial x}\right)_i = \frac{f_{i+1} - f_{i-1}}{2\Delta x}, \tag{5.10}$$

$$\left.\frac{\partial^2 f}{\partial x^2}\right)_i = \frac{f_{i+1} - 2f_i + f_{i-1}}{(\Delta x)^2}, \tag{5.11}$$

where $f = \tilde{u}, \tilde{v}, \tilde{w}$. The discretization of pressure is formed on a staggered grid:

$$\left.\frac{\partial \tilde{P}}{\partial x}\right)_i = \frac{\tilde{P}_{i+1/2} - \tilde{P}_{i-1/2}}{\Delta x}. \tag{5.12}$$

In the momentum equations for the y-z directions, the pressure gradient terms are evaluated with the average of their values at the adjacent pressure grid points ($\iota = \sqrt{-1}$),

$$\iota\kappa_y \tilde{P}_i = \iota\kappa_y \frac{\tilde{P}_{i+1/2} + \tilde{P}_{i-1/2}}{2}, \tag{5.13}$$

$$\iota\kappa_z \tilde{P}_i = \iota\kappa_z \frac{\tilde{P}_{i+1/2} + \tilde{P}_{i-1/2}}{2}. \tag{5.14}$$

Hence the discretized momentum equations are:

$$\frac{\partial \tilde{u}}{\partial t} + \tilde{S}_{x,i} = -\frac{1}{\rho}\frac{\tilde{P}_{i+1/2} - \tilde{P}_{i-1/2}}{\Delta x} + \nu\left(\frac{\tilde{u}_{i+1} - 2\tilde{u}_i + \tilde{u}_{i-1}}{(\Delta x)^2} - (\kappa_y^2 + \kappa_x^2)\tilde{u}_i\right), \tag{5.15}$$

$$\frac{\partial \tilde{v}}{\partial t} + \tilde{S}_{y,i} = -\frac{1}{\rho}\iota\kappa_y\frac{\tilde{P}_{i+1/2} + \tilde{P}_{i-1/2}}{2} + \nu\left(\frac{\tilde{v}_{i+1} - 2\tilde{v}_i + \tilde{v}_{i-1}}{(\Delta x)^2} - (\kappa_y^2 + \kappa_x^2)\tilde{v}_i\right), \tag{5.16}$$

$$\frac{\partial \tilde{w}}{\partial t} + \tilde{S}_{z,i} = -\frac{1}{\rho}\iota\kappa_z\frac{\tilde{P}_{i+1/2} + \tilde{P}_{i-1/2}}{2} + \nu\left(\frac{\tilde{w}_{i+1} - 2\tilde{w}_i + \tilde{w}_{i-1}}{(\Delta x)^2} - (\kappa_y^2 + \kappa_x^2)\tilde{w}_i\right). \tag{5.17}$$

The pressure Poisson equation is discretized at $(i + 1/2, j, k)$, and the discretized pressure Poisson equation is given as follows:

$$\begin{aligned}\frac{\tilde{S}_{x,i+1} - \tilde{S}_{x,i}}{\Delta x} + \iota\kappa_y\frac{\tilde{S}_{y,i+1} + \tilde{S}_{y,i}}{2} + \iota\kappa_z\frac{\tilde{S}_{z,i+1} + \tilde{S}_{z,i}}{2} = \\ -\frac{\tilde{P}_{i-1/2} - 2\tilde{P}_{i+1/2} + \tilde{P}_{i+3/2}}{(\Delta x)^2} + (\kappa_y^2 + \kappa_z^2)\frac{\tilde{P}_{i-1/2} + 2\tilde{P}_{i+1/2} + \tilde{P}_{i+3/2}}{4}.\end{aligned} \tag{5.18}$$

The nonlinear term $\tilde{S}_y$ and $\tilde{S}_z$ are evaluated at the grid point by taking the mean of adjacent grid points.

5.2.2 Fractional Stepping Scheme

The fractional stepping scheme proposed by Kim and Moin (1985) is used to advance the velocity in time. The Adams-Bashforth scheme is used for the nonlinear terms in Navier–Stokes equations and Crank–Nicolson scheme is used for the diffusion terms. This scheme has a predictor step, which calculates an intermediate velocity field on the convective and diffusion terms, and a corrector step to satisfy the continuity. Since we only consider the incompressible flow in this study, the absolute pressure is not important since only the pressure gradients are important in the governing equations. There is slight difference in the fractional step scheme used here compared with the scheme proposed by Kim and Moin (1985), which does not include pressure gradient in the evaluation of the intermediate velocity.

Pressure estimation step

At time level n, the velocity and pressure field at the current level n, and the convective terms from the level n, $n-1$ are known. An estimation of the pressure (with superscript $*$)

at level $n+1$ is given as:

$$-\frac{1}{\rho}\nabla^2 P^* = \nabla \cdot \left(2\mathbf{S}^n - \mathbf{S}^{n-1}\right) \tag{5.19}$$

with zero pressure gradient as boundary conditions. With the discretization for pressure Poisson equation in Eq. 5.18, a tri-diagonal matrix is formed:

$$\begin{aligned}
&\frac{1}{\rho}\left[\tilde{P}^*_{i-1/2}\left(-\frac{1}{(\Delta x)^2}+\frac{\kappa_y^2+\kappa_z^2}{4}\right)+\tilde{P}^*_{i+1/2}\left(\frac{2}{(\Delta x)^2}+\frac{\kappa_y^2+\kappa_z^2}{4}\right)+\tilde{P}^*_{i+3/2}\left(-\frac{1}{(\Delta x)^2}+\frac{\kappa_y^2+\kappa_z^2}{4}\right)\right] \\
&= 2\left(\frac{\tilde{S}_{x,i+1}-\tilde{S}_{x,i}}{\Delta x}+\iota\kappa_y\frac{\tilde{S}_{y,i+1}+\tilde{S}_{y,i}}{2}+\iota\kappa_z\frac{\tilde{S}_{z,i+1}+\tilde{S}_{z,i}}{2}\right)^n \\
&-\left(\frac{\tilde{S}_{x,i+1}-\tilde{S}_{x,i}}{\Delta x}+\iota\kappa_y\frac{\tilde{S}_{y,i+1}+\tilde{S}_{y,i}}{2}+\iota\kappa_z\frac{\tilde{S}_{z,i+1}+\tilde{S}_{z,i}}{2}\right)^{n-1}.
\end{aligned} \tag{5.20}$$

With zero pressure gradients imposed at $i=1$ and $i=N$, the tri-diagonal form for the matrix still holds.

Predictor step

Using the estimated pressure $\tilde{P}^*$, an intermediate velocity field is evaluated as,

$$\frac{\mathbf{u}^* - \mathbf{u}^n}{\Delta t} = \left[-\left(\frac{3}{2}\mathbf{S}^n - \frac{1}{2}\mathbf{S}^{n-1}\right) - \frac{1}{\rho}\nabla P^* + \frac{\nu}{2}\nabla^2\left(\mathbf{u}^n + \mathbf{u}^*\right)\right]. \tag{5.21}$$

Using a second order accurate central difference stencil for the x direction diffusion terms, Fourier derivatives for the y and z direction diffusion terms, and a second order accurate central difference for the pressure gradients, results in,

$$\begin{aligned}
\tilde{u}^*_i - \tilde{u}^n_i = &-\Delta t\left[\frac{3}{2}S^n_{x,i} - \frac{1}{2}S^{n-1}_{x,i}\right] - \frac{\Delta t}{\rho}\left(\frac{\tilde{P}^*_{i+1/2}-\tilde{P}^*_{i-1/2}}{\Delta x}\right) \\
&+\frac{\nu\Delta t}{2(\Delta x)^2}\left[\tilde{u}^*_{i+1}-2\tilde{u}^*_i+\tilde{u}^*_{i-1}\right] - \frac{\nu\Delta t}{2}(\kappa_y^2+\kappa_z^2)\tilde{u}^*_i \\
&+\frac{\nu\Delta t}{2(\Delta x)^2}\left[\tilde{u}^n_{i+1}-2\tilde{u}^n_i+\tilde{u}^n_{i-1}\right] - \frac{\nu\Delta t}{2}(\kappa_y^2+\kappa_z^2)\tilde{u}^n_i.
\end{aligned} \tag{5.22}$$

rearranging the unknown u^* to the left hand side, a tri-diagonal system of equations can be obtained. For the velocity field, the Dirichlet boundary conditions are imposed at the inlet and outlet, with values $\mathbf{u}_{in}$ and $\mathbf{u}_{out}$.

Corrector step

In the corrector step, the intermediate velocity $\mathbf{u}^*$ obtained by the predictor step is corrected, so the velocity and pressure field satisfy the continuity equation. The velocity correction step can be written as,

$$\tilde{\mathbf{u}}^{n+1} - \tilde{\mathbf{u}}^* = -\frac{\Delta t}{\rho}\nabla\tilde{\phi}, \tag{5.23}$$

where $\tilde{\phi}$ is the correction to pressure, and $\tilde{\phi}$ will have to satisfy the Poisson equation,

$$\frac{\Delta t}{\rho}\nabla^2\tilde{\phi} = \nabla\cdot\mathbf{u}^*\,. \tag{5.24}$$

Following a similar scheme developed for the pressure estimate equations, a second order finite difference approximation for the x-direction derivatives and the Fourier approximation for the y and z direction derivatives, the following discretized equation is obtained

$$\begin{aligned}&\frac{\Delta t}{\rho}\left[\frac{\tilde{\phi}_{i-1/2} - 2\tilde{\phi}_{i+1/2} + \tilde{\phi}_{i+3/2}}{(\Delta x)^2} - (\kappa_x^2+\kappa_y^2)\left(\frac{\tilde{\phi}_{i-1/2} + 2\tilde{\phi}_{i+1/2} + \tilde{\phi}_{i+3/2}}{4}\right)\right]\\ &= \left(\frac{\tilde{u}^*_{i+1} - \tilde{u}^*_i}{\Delta x} + \frac{1}{2}\iota(\kappa_y+\kappa_z)(\tilde{u}^*_{i+1} + \tilde{u}^*_i)\right).\end{aligned} \tag{5.25}$$

The pressure correction $\tilde{\phi}$ has the same boundary conditions as those in the pressure estimate equation described earlier.

The velocity at the step $n+1$ is evaluated as

$$\tilde{u}_i^{n+1} = \tilde{u}_i^* - \Delta t\frac{\tilde{\phi}_i - \tilde{\phi}_{i-1}}{\Delta x}, \tag{5.26}$$

$$\tilde{v}_i^{n+1} = \tilde{v}_i^* - \frac{\Delta t}{\rho}\iota\kappa_y\frac{1}{2}(\tilde{\phi}_{i-1/2} + \tilde{\phi}_{i+1/2}), \tag{5.27}$$

$$\tilde{w}_i^{n+1} = \tilde{w}_i^* - \frac{\Delta t}{\rho}\iota\kappa_z\frac{1}{2}(\tilde{\phi}_{i-1/2} + \tilde{\phi}_{i+1/2}). \tag{5.28}$$

The pressure is updated as follows,

$$\tilde{P}_i^{n+1} = \tilde{P}_i^* + \tilde{\phi}_i. \tag{5.29}$$

Formulation of the force

The full Navier-Stokes equations admit the inclusion of an external body force, denoted as $\mathbf{f}$, which is allowed to be a function of both time and space. The divergence of the force may be

non-zero and must be included in the Poisson equation for pressure.

$$\frac{\partial \mathbf{u}}{\partial t} + (\mathbf{u} \cdot \nabla)\mathbf{u} = -\frac{1}{\rho}\nabla P + \nu \nabla^2 \mathbf{u} + \mathbf{f}, \tag{5.30}$$

and the pressure Poisson equation is modified as

$$-\frac{1}{\rho}\nabla^2 P = \nabla \cdot ((\mathbf{u} \cdot \nabla)\mathbf{u} - \mathbf{f}). \tag{5.31}$$

In the immersed boundary method, the forcing term is specified in a way to simulate the presence of a solid boundary within the computational domain, with no additional computational grid restructuring, which is an obvious advantage of this method. Furthermore, multiple objects can be simulated easily, and the relative motion of the immersed bodies may be accomplished at some reasonable computational cost.

The form of the forcing function can be derived from the discrete-time Navier-Stokes equations,

$$\frac{\mathbf{v} - \mathbf{u}^n}{\Delta t} = -(\mathbf{u} \cdot \nabla)\mathbf{u} - \frac{1}{\rho}\nabla P + \nu \nabla^2 \mathbf{u} + \mathbf{f}. \tag{5.32}$$

If on some surface Ω, a desired velocity $\mathbf{v}(\Omega)$ is needed, then Eq. 5.32 becomes,

$$\mathbf{f} = \frac{\mathbf{v} - \mathbf{u}^n}{\Delta t} + (\mathbf{u} \cdot \nabla)\mathbf{u} + \frac{1}{\rho}\nabla P - \nu \nabla^2 \mathbf{u}. \tag{5.33}$$

The fractional step method including evaluation of the forcing is given as follows:

$$\mathbf{f}^n = \frac{\mathbf{v} - \mathbf{u}^n}{\Delta t} + \left(\frac{3}{2}\mathbf{S}^n - \frac{1}{2}\mathbf{S}^{n-1}\right) + \nabla P^n - \nu \nabla^2 \mathbf{u}^n, \tag{5.34a}$$

$$-\frac{1}{\rho}\nabla^2 P^* = \nabla \cdot \left(\frac{3}{2}\mathbf{S}^n - \frac{1}{2}\mathbf{S}^{n-1} - \mathbf{f}^n\right), \tag{5.34b}$$

$$\mathbf{u}^* = \mathbf{u}^n + \Delta t \left[-\left(\frac{3}{2}\mathbf{S}^n - \frac{1}{2}\mathbf{S}^{n-1}\right) - \frac{1}{\rho}\nabla P^* + \frac{\nu}{2}\nabla^2 \left(\mathbf{u}^n + \mathbf{u}^*\right) + \mathbf{f}^n \right], \tag{5.34c}$$

$$\frac{\Delta t}{\rho}\nabla^2 \tilde{\phi} = \nabla \cdot \mathbf{u}^*, \tag{5.34d}$$

$$\tilde{\mathbf{u}}^{n+1} = \tilde{\mathbf{u}}^* - \frac{\Delta t}{\rho}\nabla \tilde{\phi}, \tag{5.34e}$$

$$\tilde{P}^{n+1} = \tilde{P}^* + \tilde{\phi}. \tag{5.34f}$$

The forcing formed in Eq. 5.34a is forcing the intermediate velocity $\mathbf{v}^*$. Since $\mathbf{v}^*$ is corrected by ϕ to satisfy continuity, the forcing $\mathbf{f}^n$ may have some errors and hence the no-slip boundary condition is not satisfied exactly at the boundary points.

5.3 Results

In this section, the numerical results from the immersed boundary method is validated with the laminar flow past a single sphere. In this validation study, $128\times64\times64$, $256\times128\times128$ and $512\times256\times256$ uniform Cartesian grid points are used to study the laminar flow past a single sphere, with $L_y = L_z = 2\pi$ and $L_x = 4\pi$. Let the number of the grid points used to represent the sphere as D, and the ratio between D and N_Y is fixed to be 6.4. For $Re_p = 20, 50, 100$, the drag coefficient is compared with the standard drag curve from Schiller and Nauman [Clift et al. (1978)]. When compared with standard drag curve, the drag coefficient from the immersed

Table 5.1 Comparison of the drag coefficient from present simulations with the standard drag curve from Schiller and Nauman [Clift et al. (1978)]

Re_p	C_D $128\times64\times64$	C_D $256\times128\times128$	C_D $512\times256\times256$	C_D from Schiller and Nauman
20	2.07	2.36	2.62	2.52
50	1.28	1.41	1.60	1.54
100	0.94	0.98	1.13	1.09

boundary method is quite close to the correlation from Schiller and Nauman [Clift et al. (1978)]. As the resolution of the flow field and the sphere increases, the drag coefficient becomes closer to the standard drag. For the highest resolution tested, the relative error is less than 3% for all the three particle Reynolds number $Re_p = 20, 50, 100$. The drag coefficient in Table 5.1 is also plotted in Figure 5.1 .

For particle Reynolds number range $20 < Re < 130$, the separation ring moves forward, so that the attached recirculation wake widens and lengthens. The correlation for the recirculation bubble length is given in Pruppacher et al. (1970)

$$L_w/d = 1.50\log(Re) - 2.07, \tag{5.35}$$

and the numerical results from the immersed boundary method are compared with this correlation.

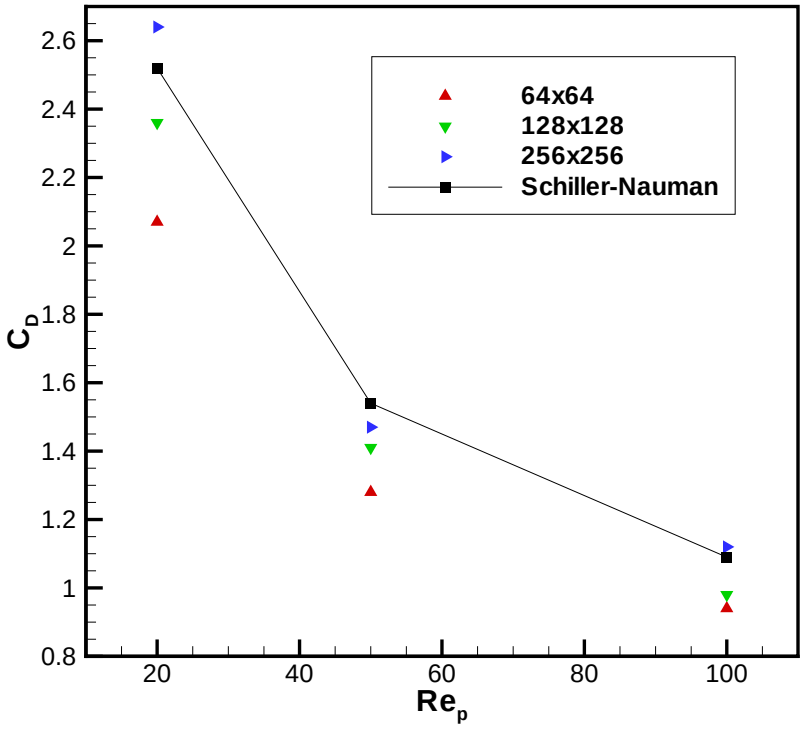

Figure 5.1 Variation of drag coefficient C_D with particle Reynolds number. The standard drag in square symbols is from Table 5.2 in Clift et al. (1978).

Table 5.2 Comparison of the non-dimensional wake length from present simulations with correlation from Pruppacher et al. (1970).

Re_p	numerical results L_w/d	L_w/d from Pruppacher et al. (1970)
50	0.45	0.478
100	0.91	0.93

CHAPTER 6. PARALLELIZATION OF THE IMMERSED BOUNDARY METHOD

6.1 Introduction

This chapter presents the parallelization of the immersed boundary method for the particle-laden flows described in chapter 5. Parallelization is necessary for this application because of the very large CPU and memory requirements. This parallelization is accomplished by parallelizing the basic three steps in the serial algorithm using domain decomposition [Snir et al. (1998)] and a parallel tri-diagonal linear equation solver [Povitsky (1998); Badia and Vidal (1993)]. The performance of the parallel algorithm is evaluated for turbulent flow with 200 stationary particles. The parallel algorithm is then validated for a single stationary sphere in a homogeneous turbulent flow using published data from Bagchi and Balachandar (2003).

We were not able to find any published papers that discuss the parallelization of the immersed boundary method for structured grids. However, the following gives references for the parallel DNS studies on structured grids for single phase turbulence. For homogeneous turbulence on structured grids, many researchers use pseudo-spectral methods [Orszag and Patterson (1972); Rogallo (1981); Pope (1999)]. For these methods, typically more than 90% of the CPU time is spent in the serial execution of the three-dimensional FFT (3D FFT). Therefore, recent parallel DNS studies focus on the efficiency of the parallel 3D FFT [Kaneda and Yakokawa (2005)]. Turbulent flows which are statistically inhomogeneous in one direction are studied by Garg et al. (1997). He used the hybrid spectral finite difference method to study stratified turbulent flows for distributed memory parallel computers. Parallelization was done using domain decomposition and parallel 2D FFTs.

6.2 Serial Algorithm for the Immersed Boundary Method

The following flow chart gives an overview of the serial algorithm. As one can see from the

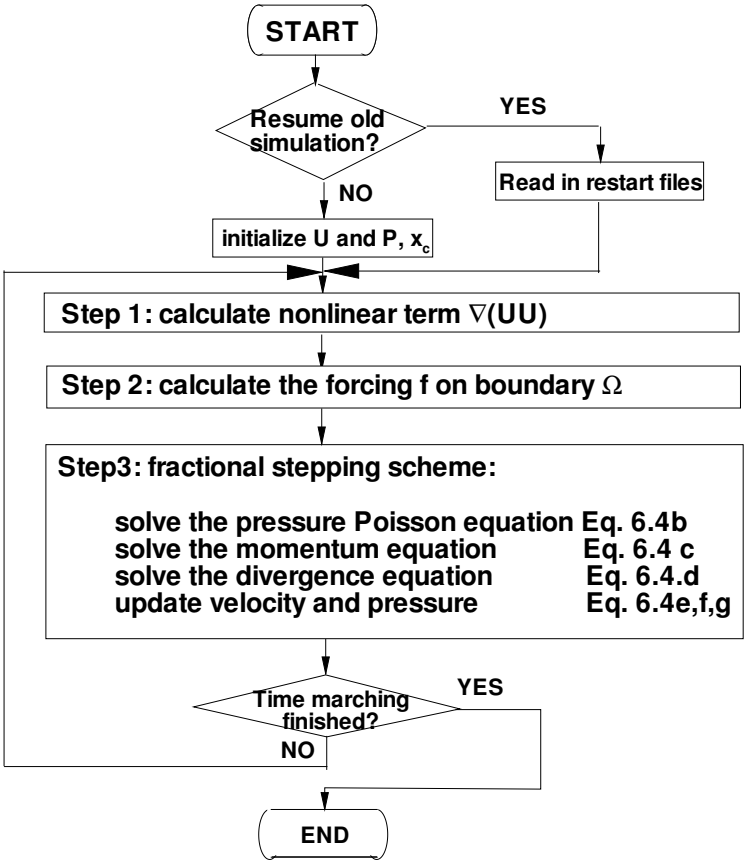

Figure 6.1 Flow chart of the serial immersed boundary method.

flow chart, there are three major steps for the serial algorithm for each time step:

Step 1: the calculation of nonlinear terms $\nabla(\mathbf{uu})$ on the flow domain;

Step 2: the calculation of the external forcing function on particle surfaces;

Step 3: solving Navier-Stokes equation on the flow domain using the fractional stepping scheme.

An examination of these steps shows that there are data dependencies between these steps: step 2 cannot be calculated until step 1 has completed and step 3 cannot be calculated until step 2 has completed. The serial algorithm for the immersed boundary method is presented

in Appendix A.

The memory requirement of the serial algorithm can be estimated as follows: the memory occupied by one 3D array with the size $\mathrm{NX} \cdot \mathrm{NY} \cdot \mathrm{NZ}$ is $8 \cdot \mathrm{NX} \cdot \mathrm{NY} \cdot \mathrm{NZ}$ bytes assuming that each array element requires 8 bytes of storage. NX represents the number of grid points in the x direction. NY is the number of grid points in the y direction and NZ is the number of grid points in the z direction. NX, NY and NZ can be any positive integers. There are 33 such arrays used in the serial immersed boundary method. Hence, the total memory requirement for problem size is at least $264 \cdot \mathrm{NX} \cdot \mathrm{NY} \cdot \mathrm{NZ}$ bytes. For example, if $\mathrm{NY} = \mathrm{NZ} = 256$ and $\mathrm{NZ} = 512$, the memory required is at least 8.25GB.

The CPU time required can be estimated by counting the number of floating point operations. In step 1 there are $9 \cdot \mathrm{NX}$ two dimensional FFTs performed. Each 2D FFT requires $\mathcal{O}(\mathrm{N} \cdot \log(\mathrm{N}))$ operations where $\mathrm{N} = \mathrm{NY} \cdot \mathrm{NZ}$. Therefore, the floating point operation count for step 1 is of order

$$9 \cdot \mathrm{NX} \cdot \mathcal{O}\left(\mathrm{NY} \cdot \mathrm{NZ} \cdot \log\left(\mathrm{NY} \cdot \mathrm{NZ}\right)\right).$$

In Step 2, let N_p be the number of particles in the flow and let N_s be the number of surface points on each sphere. Since there are N_s operations for each particle, the floating point operation count for step 2 is of order

$$\mathcal{O}\left(N_p \cdot N_s\right).$$

In Step 3, there are $5 \cdot \mathrm{NY} \cdot \mathrm{NZ}$ tri-diagonal linear systems of size NX. The Thomas algorithm is used to solve each tri-diagonal linear system, and this requires $(4 \cdot \mathrm{NX} - 3)$ floating point operations. Therefore, the floating point operation count for step 3 is

$$5 \cdot \mathrm{NY} \cdot \mathrm{NZ} \cdot (4 \cdot \mathrm{NX} - 3).$$

From the above analysis, the time to execute step 1 will dominate for large NX, NY and NZ. For example, suppose $\mathrm{NX} = 384$, $\mathrm{NY} = \mathrm{NZ} = 192$, $N_p = 100$, and $N_s = 1800$, Table 6.1 shows the percentage of time for each step.

Table 6.1 The list for the serial execution time for Step 1, 2 and 3 as percentages of the total serial execution time T for one iteration in the flow chart Figure 6.1.

Step 1	Step 2	Step 3
80%	5%	15%

6.3 Parallelization of the Immersed Boundary Method

Parallelization is accomplished by first decomposing the computational domain into p subdomains where p is the number of MPI processes. This decomposition will be used for all three steps in the serial algorithm.

There are many ways to decompose the computational domain. In this study, the domain decomposition was chosen to be along the x direction, and this is because the 2D-FFT is performed along y and z directions for each x value in the flow domain. If the number of MPI processes, p, is 4 then the decomposed flow domain is sketched in Figure 6.2. In this study, the number of MPI processes p can be any positive integer, and p is not necessary to evenly divide NX.

Parallelization of step 1. The parallelization of Step 1 uses the standard domain decomposition method with ghost cell of depth one on both sides of each subdomain. The nonblocking MPI sends and receives are used for communication between subdomains. The details can be found in Appendix B.

Parallelization of step 2. The first step is to determine which subdomain the center of each particle is in. If particles move, the subdomain that each particle center is associated with changes in time. For the simplified case of multiple stationary particles, this step only needs to run once at the beginning of the simulation. There are two cases to consider:

i) if a particle lies entirely within a subdomain, then the calculation of the forcing function can be done independently of the calculation for all the other particles;

ii) if a particle lies on two or more subdomains, then the portions of particle surfaces can be independently calculated in the subdomain where the surface resides.

The load balancing for step 2 depends upon the distribution of particles among the subdo-

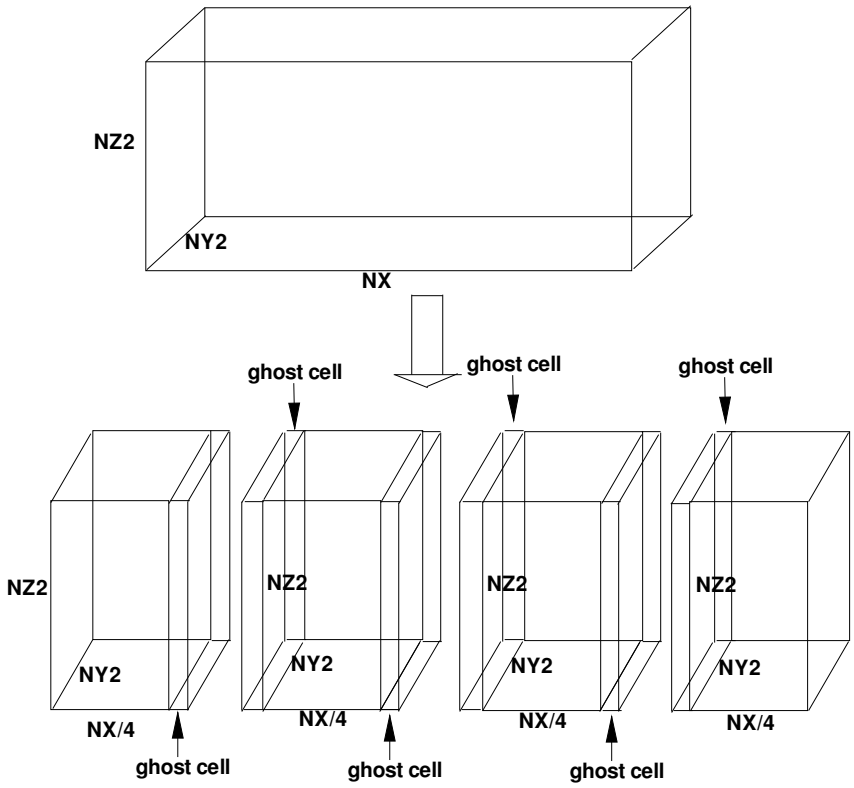

Figure 6.2 Data distribution in 3D array for number of processors $p = 4$.

mains. The worst case occurs when all the particles are entirely contained in one subdomain. In this case, the performance of parallel algorithm for Step 2 would be the same as the serial performance for Step 2. If the particles are evenly distributed on all MPI processes, the load balancing will be good.

If the surface points are at the boundary of one subdomain, then the value of neighboring grid points are required for Step 2 at these surface points. Ghost cells with depth two are used at the both sides of each domain since we approximate second order partial derivatives. To update the values for the ghost cell points, communication between subdomains uses the MPI send-receive routine, which was chosen for ease of programming. Using nonblocking MPI routines may give better performance and this may be investigated in future work.

Parallelization of step 3. The discretization of the serial algorithm for step 3 produces $5 \cdot \text{NY} \cdot \text{NZ}$ tri-diagonal linear systems of size NX by NX to solve. Each system is then solved using a parallel tri-diagonal linear equation solver. Each of these tri-diagonal linear systems can be solved independently of the other. Thus an easy parallelization would be to distribute these equations among the p processes. However, each process would not have enough memory to do this. The two parallel tri-diagonal solvers published in Badia and Vidal (1993) and Povitsky (1998) were implemented and their performance compared. One is the parallel cyclic reduction [Badia and Vidal (1993)], and the other is the parallel Thomas algorithm [Povitsky (1998)]. Table 6.2 shows that for both algorithms, the parallel execution time increases as p increases from 8 to 16 and from 16 to 32. The parallel execution time could not be obtained for $p = 2$ and 4 because of memory limitations. The parallel Thomas algorithm was used for the parallelization of step 3, since it is faster than the parallel cyclic reduction.

Table 6.2 Parallel execution time (seconds) for a tri-diagonal matrix with N=511.

number of processes (p)	$p = 8$	$p = 16$	$p = 32$
Parallel Thomas algorithm	1.780E-4	2.658E-4	4.139E-4
Parallel cyclic reduction	5.052E-4	5.810E-4	6.305E-4

6.4 Example

In this section we study the performance of the parallel code developed for 200 fixed spheres in a turbulent flow using the "lightning" cluster at Iowa State University. Lightning is a 592-processor core (148 node) 2.4 GHz, dual-processor, dual core AMD 280 Opteron cluster with 8 GB of memory per node and uses the InfiniPath HTX interconnect technology. For this example, NX, NY, NZ, N_s and N_p have been chosen to be appropriate for the exposition in chapter 7 for $p = 8$, 16 and 32. NX = 512, NY = NZ = 256. The number of spheres is $N_p = 200$ and the number of surface points is $N_s = 3190$. The locations of the 200 spheres are generated using the Matérn hard-core distribution described in Section 7.3. We do not assume the 200 spheres are entirely within any single subdomain. For this problem, the parallel execution time

for one iteration is listed in Table 6.3. This problem cannot be run on lightning with $p = 2$ and 4 due to insufficient memory.

Table 6.3 Parallel execution time (seconds) for the example in Section 6.4.

number of processes (p)	$p = 8$	$p = 16$	$p = 32$
time for step 1, 2 and 3	35.6	25.9	25.1

Notice that there is a good speedup from $p = 8$ to $p = 16$, but the CPU time for 32 processes was about the same as for 16 processes. The time for step 1 will decrease as p increases because step 1 has good load balancing. The time for step 2 will decrease as the number of processors p increases because we assumed the 200 spheres are uniformly distributed among the subdomains. However, from Table 6.2, we see that the time for step 3 increases as p increases. The poor scalability for this example is caused by the poor scalability of the parallel Thomas algorithm in step 3 for tri-diagonal linear systems of size 512 by 512. Future research should investigate alternative methods for the parallelization of step 3.

6.5 Validation Study of the Parallel Immersed Boundary Method

The accuracy of the parallel program is validated using the data by Bagchi and Balachandar (2003) for a single stationary sphere in a homogeneous turbulent flow. The validation is not dependent on the number of processors used so 16 processors were used since 16 processors gave the best performance in the example in Section 6.4 and there was sufficient memory for each processors to run the validation.

Description of the example in the published paper. In the numerical study by Bagchi and Balachandar (2003), the direct numerical simulation is performed with homogeneous turbulence past a spherical particle. The effects of turbulence on the mean drag are reported for different mean particle Reynolds numbers and turbulence intensity. The isotropic turbulence field is a precomputed frozen isotropic box turbulence which provides a turbulent ambient flow and is characterized by a single parameter, the micro-scale Reynolds number [Pope (1999)]. The box turbulence uses DNS date on a uniform Cartesian grid of size $256 \times 256 \times 256$. The

effect of the turbulent field is as if the isotropic turbulent field sweeps past the stationary sphere at velocity $\mathbf{V}$. Body-fitted grids are used to compute the flow field around the sphere. The numerical results from Bagchi and Balachandar (2003) should be more accurate than the numerical results produced by the authors immersed boundary method since the immersed boundary method does not use body-fitted grids. The parameters in the DNS by Bagchi and Balachandar (2003) are listed in Table 6.4, where η is the Kolmogorov length scale; λ is Taylor

Table 6.4 Physical parameters in the DNS study of Bagchi and Balachandar (2003).

Case	d/η	d/λ	d/Λ	$I = u_{rms}/\lvert\mathbf{V}\rvert$	$\langle Re_r \rangle$
1	1.53	0.061	0.003	0.1	107
2	1.53	0.061	0.003	0.2	58
3	3.84	0.152	0.008	0.1	261
4	3.84	0.152	0.008	0.25	114
5	9.59	0.381	0.019	0.1	609
6	9.59	0.381	0.019	0.25	241

micro-scale and Λ is the integral scale. The parameters are the ratio of the particle diameter d to the Kolmogorov length scale η; the turbulent intensity $I = u_{rms}/|\mathbf{V}|$; the mean particle Reynolds number $\langle Re_r \rangle = |\mathbf{V}_r|d/\nu$, where u_{rms} is the rms of the fluctuations of the free-stream turbulence; $\mathbf{V}_r$ is the instantaneous relative velocity between the particle and the undisturbed ambient flow measured at the center of the particle; and $\langle \mathbf{V}_r \rangle$ is the mean relative velocity obtained by time averaging over time T.

Set-up for the immersed boundary method. Upstream turbulence is introduced from the inlet velocity boundary condition using a uniform Cartesian grid of size $NX = 512$, $NY = NZ = 256$. The isotropic homogeneous box turbulence is generated using the model spectrum [Pope (1999)] in a $256 \times 256 \times 256$ cubic box instead of using DNS data. The velocity and pressure fields are initialized to zero. The turbulence disturbance is introduced into the flow domain instead of introducing the turbulence in the body-fitted grid. Since the turbulence flow field is a (statistically) stationary process, the mean drag coefficient is calculated using time averaging as was done by Bagchi and Balachandar (2003).

In this study, the mean particle Reynolds number Re_p and turbulent intensity, I, match the parameters in Table 6.5. The ratio between particle diameter and free-stream turbulence

length-scale d/η, d/λ, and d/Λ cannot be matched because the immersed boundary method does not use body-fitted grids. The parameters in the immersed boundary simulation for upstream turbulence past a single stationary particle is listed in Table 6.5.

Table 6.5 Physical parameters studied using the immersed boundary method in this work.

Case	$\langle Re_p \rangle$	$I = u_{rms}/\lvert\mathbf{V}_r\rvert$	d/η	λ/d	Re_λ
1	107	10%	5	1.65	18
2	114	25%	10	1.10	31
3	58	20%	5	1.78	21

Comparison of results. Table 6.6 compares the time averaged drag coefficient, C_D, of the immersed boundary (IB) method with the results from Bagchi and Balachandar (2003). Table 6.6 shows that the mean drag coefficient from the immersed boundary method is quite

Table 6.6 Time averaged C_D from the immersed boundary method compared with the drag coefficient by Bagchi and Balachandar (2003).

Case	$\langle Re_p \rangle$	$I = u_{rms}/\lvert\mathbf{V}_r\rvert$	C_D (IB method)	C_D Bagchi and Balachandar (2003)
1	107	10%	1.02	1.07
2	114	25%	1.025	1.03
3	58	20%	1.52	1.53

close to the numerical results from Bagchi and Balachandar (2003) with maximum deviation for case 1 being 4.6%, for case 2 being 0.5%, and for case 3 it is 0.6%.

CHAPTER 7. DIRECT NUMERICAL SIMULATION OF TURBULENT FLOW PAST A FIXED BED OF SPHERES

7.1 Introduction

In this chapter, the immersed boundary method discussed in Chapter 5 is used as a true direct numerical simulation tool to study the effects of particle clusters on fluid phase turbulence. This is motivated by the experimental observations of Moran and Glicksman (2003a). In this experiment, gas phase fluctuations are measured inside a circulating fluidized bed (CFB) with dilute particle concentrations ($\sim$ 1%–5%). The measurements indicate that at larger particle concentrations where clusters usually are formed, gas phase fluctuations increase dramatically. Moran and Glicksman (2003a) suggested that a length scale based on the cluster size, as opposed to the particle size, should be used to estimate the increased levels of gas fluctuations caused by the particle phase.

It is worth noting that this conclusion is made by comparing the results from Glicksman's experiments with the criterion suggested by Gore and Crowe (1989), rather than the direct analysis of experimental data. The principal conclusion from Gore and Crowe (1989) is that the fluid phase turbulence intensity increases dramatically if $d_p/l_e > 0.1$, where d_p is the size of particle and l_e is characteristic length scale of the most energetic eddy in the flow. For d_p/l_e below this critical value 0.1, the turbulence intensity is not found to increase with the addition of particles. The ratio $d_p/l_e = 0.01$ in Glicksman's experiments is an order of magnitude below the cutoff value 0.1 suggested by Gore and Crowe (1989). Therefore, the Gore and Crowe criterion indicates the addition of small particles ($164\mu m$) would decrease the turbulence intensity for Glicksman's experiments. However, the experimental data show 158% increase of turbulence intensity inside the CFB. Moran and Glicksman attribute this

discrepancy to the continuous formation and breakage of particle clusters in CFB. A plausible explanation to describe the apparent increase in gas phase fluctuations is that the dominant structures are particle clusters, with the dominant particle length scale being the cluster size d_c, instead of the particle diameter d_p. If the length scale of the particle cluster d_c is chosen as the particle phase length scale in Gore and Crowe's criterion, then $d_c/l_e = 1.25$, which is an order of magnitude greater than the cutoff value of 0.1. Now Gore and Crowe's criterion applied using d_c instead of d_p, indicates that the fluid phase TKE increases with the addition of small particles in Moran and Glicksman's experiments.

Moran and Glicksman (2003b) also tried to measure the effect a single particle cluster has on the surrounding gas flow. That experimental work focuses on a small riser with the ability to release a single cluster at a time. The single cluster is introduced in the riser by a thimble located at the riser centerline, which is attached to a spring at the top of the riser via a Kevlar line. By extending the Kavler line and then releasing, the thimble halts abruptly and launches the clusters into the riser. There is no direct measurement of gas velocity around particle clusters, and it is difficult to quantitatively characterize the length scale of particle clusters in this experiment.

These experimental studies by Moran and Glicksman (2003a,b) suggest that particle cluster size should also be considered as one of the model parameters in gas-solid turbulence models, but it is difficult to extract data from these experiments for modeling purposes. DNS offers an alternative means of investigating gas-solid turbulent flows. In principle, the dataset from DNS can be used to quantify unclosed terms in the Eulerian–Eulerian models. Using DNS to study the effects of particle clusters on the unclosed terms in EE models can provide valuable insight into fluid-phase TKE modulation by the addition of particle clusters.

The numerical schemes in DNS can be categorized into those that resolve the flow around each particle, or "true" DNS, and those that do not. For the DNS studies that do not resolve the flow around each particle, the point-particle approximation is usually invoked, based on the assumption that the particle size is smaller than the Kolmogorov length scale of fluid-phase turbulence. In this approach, the velocity and location of particles are evolved through

the particle velocity evolution equation proposed by Maxey and Riley (1983), while the fluid phase is solved using Navier–Stokes equations, augmented by addition term, the interphase momentum transfer. The drag force on the particle is usually modeled as the linear drag law under the condition that $d_p \Delta u/\nu < 1$ and $\rho_p/\rho_f \gg 1$, where Δu is the characteristic velocity difference between the particle and the local flow field. Kernel averaging is performed to interpolate the interphase momentum transfer to the fluid momentum equation (also called two–way coupling), provided the velocity statistics are locally homogeneous on the scale of the particle size d_p. Since particles are modeled as point force in the flow field and the boundary layer around each particle is not fully resolved, the interphase momentum and energy transfer are effectively modeled in point–particle DNS [Sundaram and Collins (1999)]. With the numerical scheme such as the immersed boundary method, the exact no-slip and no-penetration boundary conditions are imposed on the surface of each particle. Since all the length and time scales are fully resolved in *true* DNS, the unclosed terms in Eulerian–Eulerian models can be evaluated directly.

The transport equation for fluid phase TKE in the Eulerian–Eulerian approach is given in Eq. 2.16 (Chapter 2):

$$\alpha_f \rho_f \frac{\partial k_f}{\partial t} + \alpha_f \rho_f \left\langle U_k^{(f)} \right\rangle \frac{\partial k_f}{\partial x_k} + \frac{1}{2} \alpha_f \rho_f \frac{\partial}{\partial x_k} \left\langle \rho u_i''^{(f)} \rho u_i''^{(f)} \rho u_k''^{(f)} \right\rangle =$$
$$- \left\{ \left\langle I_f \rho u_i''^{(f)} u_k''^{(f)} \right\rangle \frac{\partial \left\langle U_i^{(f)} \right\rangle}{\partial x_k} \right\} + \left\langle u_i''^{(f)} \frac{\partial (I_f \tau_{ki})}{\partial x_k} \right\rangle + \left\langle u_i''^{(f)} M_i^{(f)} \right\rangle . \qquad (2.16)$$

The terms on the right hand side are

(i) the production of TKE in the fluid phase due to mean velocity gradients;

(ii) the correlation between the fluctuating velocity–stress gradient (this term is usually modeled as the dissipation in the fluid phase);

(iii) the fluctuating velocity–interfacial momentum transfer correlation.

In Eq. 2.16, the Reynolds stress in the production, the dissipation, and the interphase TKE transfer terms are unclosed terms and need modeling. Usually it is difficult to quantify the these unclosed terms from experimental data. For example, in the recent experiments of

particle-laden homogeneous turbulent flows done by Hwang and Eaton (2006a), the viscous dissipation ε is not measured directly from the fluctuating velocity. Instead the measurement of the viscous dissipation is based on LES analogy technique described by Sheng et al. (2000). With DNS datasets, the interphase TKE transfer term and the viscous dissipation can both be quantified directly. We use the parallel immersed boundary method developed in Chapter 5 and Chapter 6 to study the particle clustering effects on fluid phase TKE.

In this study, the upstream turbulence past a fixed bed of spheres is chosen as the test case. The spheres with the same radius are used to model the particles in the riser and CFB. With the positions of spheres fixed, different random point distributions can be applied. Hence particle clusters can be easily generated and the level of clustering can be measured quantitatively using second order statistics. With stationary spheres, we also avoid the modeling of sphere collisions and the lubrication forces when spheres come close to each other. Moreover, once these spheres start moving around, the level of particles clustering cannot be controlled.

The case of laminar flows past fixed bed of spheres is studied by Hill et al. (2001a,b). The periodic boundary conditions are imposed in all three directions in order to study the drag force on the homogeneous suspensions. In this DNS, the zero gradient boundary conditions are applied in the streamwise direction (the x direction), while the periodic boundary conditions are applied in the span-wise directions (the y- and z- directions). We choose to use the inlet/outlet boundary conditions in this study. It is because with the inlet/outlet boundary conditions, the turbulence intensity, the upstream fluid phase correlation length and time scales can be maintained, while these important parameters in fluid phase turbulence are expected to evolve with the periodic boundary conditions.

In this Chapter, the estimation of memory requirements is studied in Section 7.2. The important parameters in the DNS are described in Section 7.3. The numerical results are presented in Section 7.4. The discussions of these results and the summary are shown in Section 7.5 and Section 7.6.

7.2 Estimation of Memory Requirements

Gas–solid turbulent flows are commonly encountered in the industrial environment, such as the free board of circulating fluidized bed (CFB), fluid catalytic cracking (FCC) riser, etc. For an industrial system like CFB and FCC riser, the particle size is mostly around $20 \sim 80$ μm. With this range of particle size d_p, the minimum fluidized velocity u_{mf} corresponds to particle Reynolds number less than 20 [Kunii and Levenspiel (1969)], where the Reynolds number is defined based on the minimum fluidized velocity

$$Re_p = \frac{d_p u_{mf} \rho_f}{\mu_f}. \tag{7.1}$$

The solid volume fraction at the free board of CFB and FCC will be quite small ($1\% \sim 5\%$), and the particle Reynolds number is usually around $20 \sim 50$[1]. In the experimental study by Moran and Glicksman (2003a), the ratio between the fluctuating velocity and the mean gas phase velocity is up to 40%[2]. Hence for an industrial system like CFB and FCC riser, the ranges for the important non-dimensional parameters are:

1. particle Reynolds number $Re_p = 20 \sim 50$,
2. solid volume fraction $\alpha_p = 1\% \sim 5\%$,
3. the turbulent intensity u'/U is up to 40%.

With these physical parameters keeping in mind, we now focus on the numerical requirements for resolving the important length and time scales in the particle–laden turbulent flow. To resolve the single phase isotropic turbulence, the box size $\mathcal{L}$ should be large enough to represent the energy-containing motions; and the grid spacing Δx must be small enough to resolve the dissipative scales. The time step Δt used to advance the solution is limited by the consideration of numerical accuracy.

The resolution of the smallest motions, characterized by the Kolmogorov scale η, demands sufficiently small grid spacing $\Delta x/\eta$, or correspondingly, a sufficiently large maximum

[1] In the experiment study by Moran and Glicksman (2003a) the average Reynolds number is estimated to be around 23.

[2] In that experiment, mean velocity of gas is 2.1m/s, while the fluctuating gas velocity is 0.8m/s.

wavenumber κ_{max} when solving the Navier-Stokes equations in Fourier space. Experience shows that $\kappa_{max}\eta \geq 1.5$ is the criterion for good resolution of the dissipative length scales. The other spatial resolution requirement that the box size $\mathcal{L}$ is large enough to hold the energy–containing motions, can be represented by the relation between $\mathcal{L}$ and the integral length scale L_{11}. This requirement is not easy to use, since L_{11} can be obtained accurately by integrating the two–point correlation function $f_r(x)$. The approximation that L_{11}/L (where $L = k_f^{3/2}/\varepsilon_f$) has asymptotic value 0.43 is only valid at very high turbulent Reynolds number. An alternative constraint for resolving large scale motions in turbulence is that the length scale characterizing the large eddies should be smaller than the box size $\mathcal{L}$. One good candidate for the length scale characterizing the large eddies is $L = k_f^{3/2}/\varepsilon_f$.

The true DNS with the exact no-slip, no-penetration boundary conditions imposed on each particle, puts more constraints on the resolution requirements. One is that there should be sufficient number of grids to resolve the boundary layer around each particle. The scaling for boundary layer states that $\delta/d_p \sim 1/\sqrt{Re_p}$, where δ is length scale for boundary layer and d_p is the diameter for particles. For the uniform grid size, if 5 grid points are used to resolve the boundary layer around each particle, for $Re_p = 50$, then the scaling requires at least 35 grid points for the particle diameter. The resolution requirements for particle–laden turbulent flows can be summarized as:

1. $\kappa_{max}\eta > 1.5$,
2. $\mathcal{L} > L = k^{2/3}/\varepsilon$,
3. $\Delta x/\delta < \frac{1}{2}$.

The important non-dimensional parameters for particle–laden turbulence are Re_p, u'/U and Re_λ, where $Re_\lambda = \dfrac{u'\lambda_g}{\nu}$ is the Taylor micro-scale Reynolds number. If the CFB, or FCC riser is the corresponding physical system for the DNS study, then the particle Reynolds number Re_p, and upstream turbulent intensity should be specified according to these physical systems.

From the physical parameter range and the resolution requirements for particle-laden turbulent flows, the minimum number of grid points N required for the fixed physical parameters

can be found out[3]. For example, Table 7.1 gives the required resolution N for $Re_p = 50$, $u'/U = 40\%$, and $\delta/\Delta x = 3$ with increasing turbulent Reynolds number Re_λ. The last column

Table 7.1 The estimate of N for $Re_p = 50$, $u'/U = 40\%$, $\delta/\Delta x = 3$.

Re_λ	20	50	80
d/η	5.1	2.0	1.3
N	400	16,140	105,800

in Table 7.1 corresponds to the particle-laden turbulent flows in CFB or FCC. Clearly the 3D dimensional simulation with $N = 105,800$ cannot be achieved at this moment. It is worth noting that the estimation of the memory consumption in this study, is based on the assumption that the underlying numerical grids are uniform Cartesian grids. In this work, the resolution with $N = 256$ is used and the physical and numerical parameters is discussed in Section 7.3.

7.3 Parameters of the Simulation

This study is concerned with the particle clustering effects on fluid phase turbulence. Since the immersed boundary method has the ability to handle moving or deforming bodies with complex surface geometry without body fitted meshes, the discrete-time immersed boundary method discussed in Chapter 5 is used to perform the "true" DNS by imposing exact boundary conditions on each particle surface. The sketch in Figure 7.1 shows the setup of this numerical simulation.

The physical parameters that characterize the laminar flow past the fixed bed of monodispersed particles are particle diameter d_p, particle number density n_p, the mean slip velocity $|U|$, particle density ρ_p, fluid density ρ_f and fluid phase viscosity ν_f. Using Buckingham Π theorem, the important non-dimensional parameters are: particle volume fraction $\alpha_p = \pi d^3 n_p/6$, density ratio ρ_p/ρ_f and particle Reynolds number $Re_p = |U|d_p/\nu$. After introducing fluid phase turbulence, the fluid turbulence length scale λ_g (Taylor micro-scale length scale) and TKE k_f are added in the dimensional parameters. Additional non-dimensional parameters are the turbulent Reynolds number $Re_\lambda = \sqrt{2k_f/3}\lambda_g/\nu$ and d_p/λ_g. From the experiments by

[3]The details can be found in Appendix C.

Moran and Glicksman (2003a), it is suggested that the particle configuration should be also considered in the parameters, and the particle cluster size d_c should be introduced into this already very broad parameter spectrum.

For laminar flow past fixed a bed of spheres, the numerical simulation by Hill et al. (2001a,b) studied the drag force coefficient on particles as a function of Re_p and α_p. Van der Hoef et al. (2005) studied the mono- and disperse spheres in the fixed bed , and numerical simulation with the Lattice Boltzmann method is performed to close the drag force relation for polydispersed systems. The particle clustering effects on the drag force coefficient is also studied by Wylie and Koch (1999). Therefore, the wide parameter spectrum for laminar flow past the fixed bed of particles is already studied by these researchers. With upstream turbulence, it is hypothesized that the fluid phase TKE modulates with different particle random configurations, which can be described by the particle cluster size d_c. This is also suggested by Moran and Glicksman (2003a). In this study we focus on the particle clustering effects on the fluid phase TKE.

The position of multiple spheres in the fixed bed is generated using two different random point distributions. One random point distribution has particle homogeneously distributed in a cubic box, and there is minimum particle clustering effects; while the other random arrangement has strong particle clustering effects. We choose the Matérn hard-core point process [Stoyan et al. (1986)] as the candidate for a spatially homogeneous random point field. Matérn hard-core process is a dependent thinning applied to a stationary Poisson process with intensity λ to eliminate the overlapping spheres.

For a random point process with particle clusters, we choose the sphere center locations from the inelastic granular gas. Inelastic particles interact through collisions from a specified initial state, and in the absence of the external forcing, the energy in the system decays according to Haff's cooling law. Beyond the homogeneous cooling state, the system spontaneously develops clusters. The particle positions of the clustering state are used as random arrangements of sphere positions in the fixed bed.

Both of these methods define an underling random point process, but the sphere positions are different from one realization to another. Four multiple independent simulations (MIS)

are performed for Matérn hard-core and the inelastic granular cooling gas respectively. In the following studies, we denote the DNS simulation with the sphere random arrangement from Matérn hard-core distribution as MHC, and the sphere positions from the clustering state of inelastic granular cooling gas are denoted as GCG. The level of the particle clustering can be characterized by the pair correlation function $g(r)$, where r is the spatial separation. The pair correlation functions $g(r)$ from Matérn hard-core and the clustering state from inelastic granular gas are shown in Figure 7.2. The largest value of $g(r)$ in Figure 7.2 is 1.05 for Matérn hard-core, and 2.4 for the clustering state from inelastic granular gas.

The physical parameters that characterize the spheres in the fixed bed are the diameter d_p, and solid volume fraction α_p. Based on the validation study for laminar flow past single sphere, DTIBM has the resolution requirement for spheres, where at least 20 grid points are used to represent the particle diameter d_p. The important parameters in the DNS are listed in Table. 7.2. The turbulence intensity defined as $u'/|\mathbf{V}|$, where $\mathbf{V}$ is the mean slip velocity

Table 7.2 The important parameters for upstream turbulence past fixed bed of spheres.

α_p	$\frac{u'}{\lvert\mathbf{V}\rvert}$	ν	Re_p	$\kappa_{max}\eta$	d/η	Re_λ
5%	20%	0.002	50	14	4.8	23

and $u' = \sqrt{2k_f/3}$. k_f is the turbulent kinetic energy in the frozen isotropic turbulence field, which is generated using Rogallo's algorithm [Rogallo (1981)]. The particle Reynolds number $Re_p = |\mathbf{V}|d_p/\nu$ is defined based on particle diameter d_p and the mean slip velocity $\mathbf{V}$. For solid volume fraction $\alpha_p = 5\%$, the total number of spheres is around 200 in the fixed bed. The cubic box that contains the spheres is of size 2π. Noted that the turbulence Reynolds number is small $Re_\lambda = 23$ which is well below the turbulence Reynolds number found in experiments. This is because the problem size as $256 \times 256 \times 512$. With the fixed resolution, the turbulent Reynolds number Re_λ is determined by Re_p and $u'/|U|$ using Eq. C.4 Appendix C. All the DNS in this chapter is done using the parallel immersed boundary method developed in Chapter 6.

The velocity isosurfaces from one realization of GCG and MHC are plotted in Figures 7.3 and 7.4 respectively. The fluctuating velocity u_1' is obtained by subtracting the mean slip

velocity **V** from the instantaneous velocity **U**, and the reference fluctuating velocity is the rms velocity in the box turbulence. Evidently, the magnitude of the fluctuating velocity $|u_1'|$ in GCG is higher than that in MHC, which indicates that the fluctuating velocity is enhanced for particle random arrangements with GCG. The numerical results are discussed in Section 7.4

7.4 Results

The numerical results from the immersed boundary method are discussed in this section. Using the ensemble averaging method, the fluid phase turbulent kinetic energy k_f is discussed in Section 7.4.1. It is observed that k_f increases along the streamwise direction inside the fixed bed. The energy spectrum of the fluid phase fluctuating energy is discussed in Section 7.4.2. The redistribution of the Reynolds-stress observed in Section 7.4.1 is discussed in Section 7.4.3.

7.4.1 The Estimation of TKE and Reynolds Stress

Since the upstream homogeneous turbulence sweeps through a fixed bed of spheres, it is reasonable to assume that the flow field is spatially homogeneous in the y-z directions, as the mean slip velocity **V** is imposed on the x direction. Multiple independent simulations (MIS) are performed for the two random arrangements, MHC and GCG. In this section, the ensemble averaging method is used to analyze fluid phase turbulence from these MIS.

The ensemble averaging of a multiphase turbulence field is defined using the indicator function I_β for phase β, where $\beta = f$ represents the fluid phase, and $\beta = p$ denotes the particle phase. The *density-weighted averaged* mean for physical quantity Q of phase β is defined as

$$\left\langle \tilde{Q}^{(\beta)} \right\rangle \equiv \frac{\langle I_\beta \rho Q \rangle}{\langle I_\beta \rho \rangle} \tag{7.2}$$

If $Q = 1$, then the volume fraction of phase β is obtained. For the incompressible flow with the constant thermodynamic density, the mean velocity without density weighting is defined as

$$\left\langle U_i^{(\beta)} \right\rangle \equiv \frac{\langle I_\beta U_i \rangle}{\langle I_\beta \rangle} \tag{7.3}$$

in this study.

The velocity field inside a fixed bed can be obtained from DNS, and MIS are also performed; thus, the estimation of the mean velocity field $\left\langle U_i^{(f)} \right\rangle$ can be formed as follows:

$$\left\langle U_i^{(f)}(\mathbf{x}) \right\rangle = \frac{\frac{1}{M}\sum_{\mu=1}^{M} U_i^{(\mu)}(\mathbf{x}) I_f^{(\mu)}(\mathbf{x})}{\alpha_f(\mathbf{x})} \tag{7.4}$$

where $\alpha_f(\mathbf{x})$ is the fluid phase volume fraction and is estimated as

$$\alpha_f(\mathbf{x}) = \frac{1}{M}\sum_{\mu=1}^{M} I_f^{(\mu)}(\mathbf{x}). \tag{7.5}$$

The mean velocity field estimated using Eq. 7.4 is a function of location $\mathbf{x}$. The indicator function field $I_f^{(\mu)}$ for a μ^{th} simulation is formed on regular Cartesian grids, and if the grid node (x_i, y_j, z_k) is occupied by fluid field, then $I_f^{(\mu)}(\mathbf{x}) = 1$, otherwise $I_f^{(\mu)}(\mathbf{x}) = 0$.

The fluid phase fluctuating velocity for μ^{th} MIS $\mathbf{u}''^{(f)}$ is

$$\left\{ \left(u_i''^{(f)} \right)^{(\mu)} \right\} = U_i^{(\mu)}(\mathbf{x}) - \left\langle U_i^{(f)}(\mathbf{x}) \right\rangle \tag{7.6}$$

Then the fluid phase Reynolds stress can be calculated as

$$\left\{ R_{ij}^{(f)}(\mathbf{x}) \right\} = \frac{\frac{1}{M}\sum_{\mu=1}^{M} I_f^{(\mu)} \left[\left(u_i''^{(f)}(\mathbf{x}) \right)^{(\mu)} \left(u_j''^{(f)}(\mathbf{x}) \right)^{(\mu)} \right]}{\alpha_f(\mathbf{x})}. \tag{7.7}$$

$U_i^{(\mu)}(\mathbf{x})$ is the i^{th} component of the instantaneous velocity field for a μ^{th} simulation. The TKE k_f is simply the half of the trace of $\left\{ R_{ij}^{(\beta)}(\mathbf{x}) \right\}$.

All the estimators in Eqs. 7.4 – 7.7 are functions of location $\mathbf{x}$, and if using the assumption that the flow field is homogeneous in y-z directions, we take the integration of the y-z plane and plot the mean velocity $\left\langle U^{(f)} \right\rangle$, $R_{ij}^{(f)}$ as functions of x. For example, the mean velocity can be estimated as follows:

$$\left\{ \left\langle \mathbf{U}^{(f)}(x_i) \right\rangle \right\} = \frac{\sum_{j,k=1}^{N_y, N_z} \left\langle \mathbf{U}^{(f)}(x_i, y_j, z_k) \right\rangle}{N_y \cdot N_z}. \tag{7.8}$$

The mean velocity $\left\langle U_1^{(f)}(x_i) \right\rangle$, TKE $k_f(x_i)$, Reynolds stress $\left\langle u_1''^{(f)} u_1''^{(f)} \right\rangle$, $\left\langle u_2''^{(f)} u_2''^{(f)} \right\rangle$ and $\left\langle u_3''^{(f)} u_3''^{(f)} \right\rangle$ are plotted in Figures 7.5—7.9. In Figures 7.5, 7.6, 7.8 and 7.9, the mean

quantities are plotted with error bars representing the standard deviation of the estimated quantities. In Figure 7.7, the standard deviation is plotted on the left-hand-side panel and the 95% confidence interval is plotted on the right-hand-side panel.

The 95% confidence interval is estimated use the student t distribution with the degree of freedom $M-1$ to estimate the statistical errors of these means, with M being the number of independent multiple runs. The student t distribution is chosen here since the variance is unknown and is estimated from the sample data. For a very large sample size ($M > 100$), t distribution is very close to the standard normal distribution. With a small sample size, the t distribution has relatively more weight in its tail than the normal distribution. With a normal distribution, 95% of the distribution is within -1.96 and 1.96 standard deviations of the mean. Using the t distribution, if the sample size is four, 95% of the area is within -3.18 and 3.18 standard deviations of its sample mean.

From these figures, it shows that there is relative small difference between MHC and GCG for the mean velocity $\langle U(x_i)\rangle$, $\left\{R_{22}^{(f)}(x_i)\right\}$ and $\left\{R_{33}^{(f)}(x_i)\right\}$. The Reynolds stress is anisotropic. The two independent invariants ξ and η of the normalized anisotropy tensor b_{ij} at different x location are found to be non-zero. The Lumley triangle [Pope (1999)] for the Reynolds stress anisotropy tensor b_{ij} is plotted in Figure 7.10. Significant redistribution of Reynolds stress is found for both MHC and GCG. On the ξ-η plane, most of the symbols follow on the $\eta = \xi$ line which indicates an axisymmetric Reynolds stress. The color of the symbols from blue to red in Figure 7.10 indicates the location of the state of anisotropy moving from $x = 0$ to $x = 12.8d_p$. Therefore, the Reynolds-stress becomes more anisotropic along the x direction inside the fixed bed.

The fluid phase TKE and Reynolds stress $\left\{R_{11}^{(f)}(x_i)\right\}$ in Figure 7.6 and 7.7 increase along the x direction inside the fixed bed for GCG, while $\left\{R_{11}^{(f)}(x_i)\right\}$ and k_f remain flat inside the fixed beds of MHC. The standard deviations are plotted in the left-hand-side panel of Figure 7.7 for the two sphere random arrangements (GCG and MHC). The standard deviation of fluid phase energy from GCG is considerably higher than that from Matérm hard-core, and this implies that the fixed bed with clusters introduces more statistical errors in the fluid phase

turbulence from GCG. The error bars with a 95% confidence interval are plotted in the right-hand-side panel of Figure 7.7. For just four MIS, 95% confidence intervals of $\left\{R_{11}^{(f)}(x_i)\right\}_1$ for GCG and MHC overlap. This indicates that more MIS is required for the convergence of fluid phase Reynolds stress and TKE.

As mentioned in Section 7.1, the experiments performed by Moran and Glicksman (2003a) reported the gas phase fluctuating velocity with particle concentrations ($\sim$ 1%–5%) in a circulating fluidized bed (CFB). The results indicate that at larger particle concentrations where clusters are formed, the gas phase fluctuations increase dramatically. This experimental result is implied from the fact that higher gas phase fluctuations are found at the larger particle concentration. However, the level of particle clustering cannot be measured directly in the experiment. The numerical results in our study reveal increasing fluid phase fluctuations inside GCG with $g(r)$ reported in Figure 7.2. These proves that the presence of particle clusters does enhance the fluid phase fluctuations from the aspect of numerical simulations.

It is also worth noting that the parameter range in the numerical and experimental studies can only be compared in a limited sense. First of all, the Kolmogorov length scale $\eta = 146\mu m$ in the CFB experiment is comparable to the particle length scale $d_p = 164\mu m$. The production length scale $l = 0.06$m that represents the largest eddy size of the gas phase turbulence is around 400 times of Kolmogorov length scale $\eta = 146\mu m$. The turbulent intensity is around 40%, and the turbulent Reynolds number $Re_\lambda \approx 136$. In the direct numerical study, the particle diameter d_p is around four times of the Kolmogorov length scale η (seen Table 7.2), and the turbulent Reynolds number $Re_\lambda = 23$ is much smaller compared to the experiments. Hence, the dissipation range of the energy spectrum is resolved in this DNS, but the largest length and time scales in the experiments cannot be solved since the resolution requirement is too high and the computational cost is prohibitive.

To understand the physical mechanism that drive the enhancement of fluid phase fluctuations by particle clusters, the budget of the transport equation of k_f and 2D energy spectrum for k_f and $R_{ii}^{(f)}$ are examined in the following section.

7.4.2 The 2D Energy Spectrum

In order to understand the physical mechanism behind the enhancement of fluid phase turbulence for GCG, the energy-spectrum of the Reynolds stress $R_{ii}^{(f)}$ is studied in this section. The energy spectrum $E(\kappa)$ is defined as

$$E(\kappa) = \oint \frac{1}{2}\mathbf{\Phi}_{ii}(\kappa)d\mathcal{S}(\kappa') \tag{7.9}$$

where $\kappa' = |\boldsymbol{\kappa}|$ is the magnitude of the wavenumber vector $\boldsymbol{\kappa}$, and $\mathbf{\Phi}_{ii}$ is the Fourier-transform of Reynolds stress $R_{ii}^{(f)}(\mathbf{x})$. For homogeneous single phase turbulence, the integration is performed overall the wavenumbers $\boldsymbol{\kappa} = \{\kappa_x, \kappa_y, \kappa_z\}$ with magnitude as κ'. In this study, the fluid phase turbulence is homogeneous only in y-z planes, where the wavenumber vector is $\boldsymbol{\kappa} = \{\kappa_y, \kappa_z\}$.

The energy spectra $E(\kappa_{yz})$ and the velocity spectra for Reynolds stress $R_{11}^{(f)}$, $R_{22}^{(f)}$ and $R_{33}^{(f)}$ at $x = 0.5d_p$, $6.4d_p$ and $12.8d_p$ are plotted in Figure 7.11—7.14. The maximum wave number number $\kappa_{max} = 120$ corresponds to the Kolmogorov length scale η, and $d_p/\eta = 4.16$, hence the corresponding wavenumber for d_p is $\kappa_{d_p} = 28.8$. From these figures, it is observed that the magnitude of $E_{11}(\kappa_{yz})$ is significantly higher than E_{22} and E_{33}. For both MHC and GCG, the energy spectra E_{22} and E_{33} at $x = 12.8d_p$ are almost the same for $\kappa_{yz} > 10$, as seen in Figure 7.16. The wiggles are observed at higher wavenumbers $|\kappa_{yz}| > 30$ in Figure 7.11—7.14, which is different from the energy spectrum of the homogeneous single phase turbulence.

To understand the wiggles at the high wavenumbers in the energy spectra, a simple numerical experiment is performed here. The random point fields $I_f(\mathbf{x})$ from MHC and GCG are used to multiple a scalar field $f(\mathbf{x})$, where the scalar field in the Fourier space is $\tilde{f}(\kappa_x, \kappa_y, \kappa_z) = \delta(\kappa_y - 1)\delta(\kappa_z - 2)$. Therefore, each y-z plane of this scalar field only has one wavenumber excited in the Fourier space. The scalar field affected by the random point field of MHC and GCG is

$$f_1(x_i, y_j, z_k) = f(x_i, y_j, z_k) \cdot I_f(x_i, y_j, z_k).$$

In Figure 7.17, the black diamond symbol represents the energy spectrum of the undisturbed scalar field. The spectra of the scalar field multiplied by the random point fields from MHC and GCG show the similar wiggles at higher wavenumber $|\kappa_{yz}| > 30$. All the wavenumbers

are all affected by the presence of particles and there is no significant difference between MHC and GCG at low wavenumbers.

The energy spectrum from GCG at the lower wavenumbers $|\kappa_{yz}| < 10$ are higher than that from MHC (seen Figure 7.15). It is hypothesized to be related to the clustering effect of the particle phase. The wavenumber corresponding to the particle size d_p is 28.8. It is useful to quantify the size of the particle cluster d_c and obtain the corresponding wavenumber κ_{d_c}. In polymer physics, the radius of gyration is used to describe the dimensions of a polymer chain. The radius of gyration of a particular molecule at a given time is defined as:

$$R_g^2 \equiv \frac{1}{N}\sum_{k=1}^{N} |\mathbf{r}_k - \mathbf{r}_{mean}|^2, \tag{7.10}$$

where $\mathbf{r}_{mean} = \frac{1}{N}\sum_{k=1}^{N} \mathbf{r}_k$ is the mean position of the N monomers, and $\mathbf{r}_k$ is the location of k^{th} monomer. Particle clusters can be found for one MIS of MHC and GCG, where each monomers in a cluster has a neighboring monomer with the distance less than some cutoff distance. In this work, the cluster size is chosen to be the radius of gyration of the particle cluster with the largest number of particles.

The cluster sizes from the four MIS of MHC and GCG are listed in Table 7.3. Since only four MIS are performed in this study, cluster sizes show large variation. With more MIS (more than 20), the cluster size of MHC converges to $1.55d$, while the cluster size of GCG converges to $2.49d$ and the wavenumber κ_{d_c} is estimated to be 11. The energy at wavenumber $\kappa_{yz} < 10$ from GCG is higher than that of MHC, where the cutoff wavenumber is close to GCG's κ_{d_c}. Therefore, the presence of particle clusters in GCG enhances the wavenumber less than κ_{d_c}.

Table 7.3 The radius of gyration of the four MIS from MHC and GCG.

	MHC	GCG
MIS 1	$1.484d_p$	$6.273d_p$
MIS 2	$1.551d_p$	$1.686d_p$
MIS 3	$1.739d_p$	$2.071d_p$
MIS 4	$1.534d_p$	$1.650d_p$

7.4.3 The Redistribution of Reynolds Stress $R_{ij}^{(f)}$

The turbulence upstream is homogeneous and isotropic. The significant redistribution of Reynolds stress is observed inside the fixed for both MHC and GCG, where $R_{11}^{(f)}$ is much higher than $R_{22}^{(f)}$ and $R_{33}^{(f)}$ (seen in Figure 7.10). The redistribution of Reynolds stress is studied by examining the important terms in the transport equation of the Reynolds stress $R_{ij}^{(f)}$,

$$\begin{aligned}
&\langle I_f \rho_f \rangle \left[\frac{\partial}{\partial t} + \left\langle U_k^{(f)} \right\rangle \frac{\partial}{\partial x_k} \right] R_{ij}^{(f)} + \frac{\partial}{\partial x_k} \left\langle I_f \rho u_i^{\prime\prime(f)} u_j^{\prime\prime(f)} u_k^{\prime\prime(f)} \right\rangle = \\
&- \left\langle I_f \rho u_i^{\prime\prime(f)} \rho u_k^{\prime\prime(f)} \right\rangle \frac{\partial \left\langle U_j^{(f)} \right\rangle}{\partial x_k} - \left\langle I_f \rho u_j^{\prime\prime(f)} \rho u_k^{\prime\prime(f)} \right\rangle \frac{\partial \left\langle U_i^{(f)} \right\rangle}{\partial x_k} \\
&+ \left\langle u_i^{\prime\prime(f)} \frac{\partial (I_f \tau_{kj})}{\partial x_k} \right\rangle + \left\langle u_j^{\prime\prime(f)} \frac{\partial (I_f \tau_{ki})}{\partial x_k} \right\rangle \\
&+ \left\langle u_i^{\prime\prime(f)} M_j^{(f)} \right\rangle + \left\langle u_j^{\prime\prime(f)} M_i^{(f)} \right\rangle
\end{aligned} \tag{7.11}$$

The two terms on the second line are the production $\mathcal{P}_{ij}$ due to the mean velocity gradients. The terms on the third line are the correlation between the fluctuating velocity and the gradient of stress. The last line is the interphase TKE transfer term. The fluctuating velocity-stress gradient correlation in gas solid turbulent flows has two parts:

$$\begin{aligned}
\left\langle u_j^{\prime\prime(f)} \frac{\partial (I_f \tau_{ki})}{\partial x_k} \right\rangle &= \left\langle u_j^{\prime\prime(f)} \frac{\partial \left(I_f \left(-p^{\prime\prime(f)} \delta_{ik} + 2\mu S_{ki} \right) \right)}{\partial x_k} \right\rangle \\
&= - \left\langle u_j^{\prime\prime(f)} \frac{\partial \left(I_f p^{\prime\prime(f)} \right)}{\partial x_i} \right\rangle + \left\langle u_j^{\prime\prime(f)} \frac{\partial \left(I_f 2\mu S_{ki} \right)}{\partial x_k} \right\rangle .
\end{aligned}$$

The first part is the correlation between fluctuating velocity and fluctuating pressure gradient in the fluid phase, while the second part is the correlation between fluctuating velocity and the gradient of viscous stress (or rate-of-strain). The rate-of-strain S_{ki} involved here is from the instantaneous velocity field $S_{kj} = \frac{1}{2} \left(\frac{\partial U_j}{\partial x_k} + \frac{\partial U_k}{\partial x_j} \right)$, where $\mathbf{U}$ is the instantaneous velocity field. The second term is usually modeled as dissipations in multiphase turbulence models. However, the correlation between fluctuating velocity and the gradient of viscous stress (or rate-of-strain) in multiphase turbulence is different from the dissipation ε defined in the single phase turbulence theory. The dissipation ε in the statistically homogeneous single phase turbulence can be shown to be $\left\langle u_j^{\prime} \frac{\partial 2\nu s_{ki}}{\partial x_k} \right\rangle = \varepsilon = 2\nu \left\langle s_{ij} s_{ij} \right\rangle$, which is a square term, and it reduces the transport equation for k_f to $\frac{dk_f}{dt} = -\varepsilon$ for the isotropic homogeneous turbulence.

We define

$$\Theta_{ij} \equiv \left\langle u_i''^{(f)} \frac{\partial \left(I_f 2\mu S_{kj}\right)}{\partial x_k} \right\rangle + \left\langle u_j''^{(f)} \frac{\partial \left(I_f 2\mu S_{ki}\right)}{\partial x_k} \right\rangle, \tag{7.12}$$

and

$$\Pi_{ij} \equiv -\left\langle u_i''^{(f)} \frac{\partial \left(I_f p''^{(f)}\right)}{\partial x_j} \right\rangle - \left\langle u_j''^{(f)} \frac{\partial \left(I_f p''^{(f)}\right)}{\partial x_i} \right\rangle. \tag{7.13}$$

In single phase turbulence, the transport equation for Reynolds stress R_{ij} is as follows:

$$\frac{\partial \langle u_i u_j \rangle}{\partial t} + \langle U_k \rangle \frac{\partial \langle u_i u_j \rangle}{\partial x_k} + \frac{\partial \langle u_i u_j u_k \rangle}{\partial x_k} = \nu \nabla^2 \langle u_i u_j \rangle + \mathcal{P}_{ij} - \frac{1}{\rho} \left\langle u_i \frac{\partial p'}{\partial x_j} + u_j \frac{\partial p'}{\partial x_i} \right\rangle - 2\nu \left\langle \frac{\partial u_i}{\partial x_k} \frac{\partial u_j}{\partial x_k} \right\rangle. \tag{7.14}$$

The dissipation $\varepsilon_{ij} = 2\nu \left\langle \frac{\partial u_i}{\partial x_k} \frac{\partial u_j}{\partial x_k} \right\rangle$ acts as an energy sink in the transport equation for R_{ij}. The difference between $\left\langle u_j''^{(f)} \frac{\partial (I_f 2\mu S_{ki})}{\partial x_k} \right\rangle$ and the dissipation ε_{ij} can be understood from the derivation of ε_{ij} in Eq. 7.14, which arises from $2\nu \left\langle u_i \frac{\partial s_{kj}}{\partial x_k} + u_j \frac{\partial s_{ki}}{\partial x_k} \right\rangle$

$$2\nu \left\langle u_i \frac{\partial s_{kj}}{\partial x_k} + u_j \frac{\partial s_{ki}}{\partial x_k} \right\rangle = \nu \left\langle u_i \nabla^2 u_j + u_j \nabla^2 u_i \right\rangle = -\varepsilon_{ij} + \nu \nabla^2 \langle u_i u_j \rangle.$$

The correlation between fluctuating velocity and the gradient of viscous stress $\left\langle u_i''^{(f)} \frac{\partial \left(I_f 2\mu S_{kj}\right)}{\partial x_k} \right\rangle$ in the two-phase turbulence cannot be further decomposed as $-\varepsilon_{ij} + \nu \nabla^2 \langle u_i u_j \rangle$ in the single phase turbulence theory due to the presence of the indicator function I_f in the derivative $\partial(\cdot)/\partial x_k$.

To understand the redistribution of Reynolds stress R_{ij}, the second order tensors $\mathcal{P}_{ij}$, Θ_{ij}, Π_{ij} and the interphase TKE transfer term are examined. Any second order tensor can be characterized by the trace of the tensor and the anisotropy tensor b_{ij}. The trace of the terms on the right-hand-side is examined first and to obtain the relative magnitude of these terms. In this study, the half of the trace of Θ_{ij} is denoted as $\Theta = \frac{1}{2}\Theta_{ii}$ and $\Pi = \frac{1}{2}\Pi_{ii}$.

The production term $\mathcal{P}_{ij}$ arises from mean velocity gradients and $\mathcal{P} = \frac{1}{2}\mathcal{P}_{ii}$ calculated from the velocity field is less than the magnitude of Θ but is not zero. It is noted from calculation that the mean velocity gradient $\partial \left\langle U_1^{(f)} \right\rangle / \partial x$ contributes most to the production $\mathcal{P}$. From the mean velocity $\left\langle U_1^{(f)} \right\rangle$ contour in Figure 7.18, it is observed that the mean velocity field is not smooth. The following analysis shows that the mean velocity field is homogeneous, and hence

the gradients of mean velocity should be zero and the production is expected to be zero with very large sample size.

Since the flow field is statistically homogeneous in the y-z directions, the mean velocity gradients along the y-z directions are expected to be zero. It is hypothesized that the mean velocity $\left\langle U_1^{(f)} \right\rangle$ varies very little inside the fixed bed along the streamwise direction as the number of sample size increases, and therefore the mean velocity gradient $\partial \left\langle U_1^{(f)} \right\rangle / \partial x$ is expected to be zero. This can be implied from the mean momentum equation for the streamwise direction x.

$$\alpha_f \rho_f \frac{\partial \left\langle U_1^{(f)} \right\rangle}{\partial t} + \alpha_f \rho_f \left\langle U_j^{(f)} \right\rangle \frac{\partial \left\langle U_1^{(f)} \right\rangle}{\partial x_j} + \alpha_f \rho_f \left\langle U_j^{(f)} \right\rangle \frac{\partial R_{ij}^{(f)}}{\partial x_j} = -\frac{\partial \langle I_f P \rangle}{\partial x_1} + \frac{\partial \langle I_f 2\mu S_{1j} \rangle}{\partial x_j} + M_1 \tag{7.15}$$

From the budget study of Eq. 7.15 in Table 7.4, it is observed that the mean pressure gradient balances the interphase momentum transfer term. The mean pressure is found to be a linear

Table 7.4 The volume integral of the terms in Eq. 7.15. The integral is normalized by $\int_{\mathcal{V}} (VV/d)\, dv$, where the control volume $\mathcal{V}$ is over the entire fixed bed and $V = 0.2029$ is the inlet velocity.

Volume integral of the terms	GCG	MHC
$\oint_{\mathcal{S}} \left\langle U_j^{(f)} \right\rangle \left\langle U_1^{(f)} \right\rangle dS$	0.0128	0.111
$\oint_{\mathcal{S}} \left\langle U_j^{(f)} \right\rangle R_{ij} dS$	0.0106	0.006
sum of left hand side terms	0.0235	0.0175
$\int_{\mathcal{V}} -\frac{\partial \langle I_f P \rangle}{\partial x_1} dv$	0.0964	0.0947
$\oint_{\mathcal{S}} \langle I_f 2\mu S_{1j} \rangle\, dS$	-0.0002	0.0001
$\int_{\mathcal{V}} M_1 dv$	-0.0713	-0.0767
sum of right hand side terms	0.0249	0.0181

function inside the fixed bed (as seen in Figure 7.19). If infinite number of realizations are performed, the interphase momentum transfer term is expected to be uniformly distributed inside the fixed bed, and the mean pressure gradient is expected to be a constant. Therefore, the velocity $\left\langle U_1^{(f)} \right\rangle$ is expected to be a constant along the streamwise direction, since the

right-hand-side of Eq. 7.15 is expected to be zero with the infinite sample size. From the above analysis, the production in Eq. 7.11 due to the mean velocity gradient will be zero with the large sample size M. In the following study, the relative magnitude of Θ and Π are examined as a function of the fixed bed depth x/d_p. However, the interphase TKE transfer term is not studied as a function of x/d_p, and only the volume integral of this term is reported and compared with the volume integral of Θ and Π.

Assuming homogeneity in the y and z directions, the estimate of the three dimensional field $\Theta(\mathbf{x})$ in the transport equation for k_f is formed as follows

$$\{\Theta(x_i)\}_1 = \frac{\sum_{j,k=1}^{N_y,N_z} \Theta(x_i, y_j, z_k)}{N_y \cdot N_z}. \tag{7.16}$$

The $\Pi(x_i)$ and $\Theta(x_i)$ are plotted in Figure 7.20 as a function of x/d_p. These terms are normalized by Vk_{ref}/d_p, where k_{ref} is the TKE in the upstream homogeneous turbulence, d_p is the particle diameter and V is the mean slip velocity. This normalization is for the convective terms in Eq. 7.11. The fluctuating velocity and viscous stress correlation $\Theta(x)$ acts like an energy sink and the magnitude of this term is larger than that of Π. After $x > 6d_p$ downstream, the magnitude of $\Theta(x)$ from GCG is smaller than that from MHC, and by integrating $\Theta(\mathbf{x})$ from $x = 6d_p$ to $x = 11d_p$, the volume integral of GCG is 34% less than that of MHC. Therefore, $\Theta(\mathbf{x})$ of MHC dissipates more energy compared to $\Theta(\mathbf{x})$ of GCG, and $\Theta(\mathbf{x})$ directly contributes to the increasing TKE in the second half of the fixed bed ($6 < x/d_p < 12$) with the GCG random particle configuration (as seen in Figure 7.6).

The interphase TKE transfer is not plotted as a function of x/d_p in Figure 7.20. The evaluation of this term can be done using the ensemble averaging method as follows:

$$\langle Q(\mathbf{x}) \rangle = \frac{\frac{1}{M}\sum_{\mu=1}^{M} Q(\mathbf{x})\Sigma_f^{\mu}(\mathbf{x})}{\frac{1}{M}\sum_{\mu=1}^{M} \Sigma_f^{\mu}(\mathbf{x})} \tag{7.17}$$

where $\Sigma_f^{\mu}(\mathbf{x})$ is the surface measure defined in Chapter 4, Eq. 4.50. Let $Q = u_i''^{(f)} M_i^{(f)}$ in Eq. 7.17, then one can obtain a three dimensional field for $\left\langle u_i''^{(f)} M_i^{(f)} \right\rangle$. The sample space

for surface measurable quantities is much smaller compared to that of the volume measurable quantities, and the surface measurable space of 4 MIS from MHC is shown in Figure 7.21. From this figure, it is obvious that the statistical error is expected to be quite high for interphase energy transfer terms due to the small sample size. Therefore, the variation of the interphase TKE transfer term along the x direction is not studied here, but the volume integral of the trace of the interphase TKE transfer term is calculated and is compared with the volume integral of Θ in Table 7.5.

Table 7.5 The volume integrals of Θ, Π, production and interphase TKE transfer term in Eq. 7.20. The integral is normalized by $\int_{\mathcal{V}} (k_{ref}V/d_p)\, dV$, and the control volume is over the entire fixed bed.

Volume integral of terms	MHC	GCG
$\int_{\mathcal{V}} \Theta(\mathbf{x}) dV$	-1.625459	-1.464937
$\int_{\mathcal{V}} \left\langle u_i''^{(f)} M_i^{(f)} \right\rangle dV$	1.9282	1.7777
$\int_{\mathcal{V}} \Pi(\mathbf{x}) dV$	-0.0154	0.007
$\int_{\mathcal{V}} \mathcal{P}(\mathbf{x}) dV$	0.6635	0.6726

From Table 7.5[4], it is noted that Θ, the fluctuating velocity and strain-rate gradient correlation, and the interphase TKE transfer term are the dominant terms on the right-hand-side of the transport equation for $R_{ii}^{(f)}$. The volume integral of the convective term is of order 10^{-2}, and the triple velocity correlation term is of order 10^{-3}. Therefore, the anisotropic state of the second order tensor Θ_{ij} and the interphase TKE transfer term is studied here, which is characterized by two independent invariants ξ and η of the anisotropy tensor b_{ij}. Here $6\eta^2 = b_{ij}b_{ij}$ and $6\xi^3 = b_{ij}b_{jk}b_{ki}$.

Since these two tensors are functions of $\mathbf{x}$, the independent invariants ξ and η can be formed for every $\mathbf{x}$ location. We choose to compute the independent invariants for the volume integrals of Θ_{ij} and the interphase TKE transfer term, where the integration is over the entire fixed bed. The independent invariants ξ and η for these two second order tensors are listed in Table

[4]From the analysis of the mean velocity, the volume integral of the production term is expected to be zero if the sample size is large enough.

7.6, and it is noted that these two tensors are highly anisotropic. Hence, from the study of

Table 7.6 The independent invariants ξ and η for Θ_{ij} and the interphase TKE transfer terms.

	ξ	η
Θ_{ij} (GCG)	0.2120	0.2120
Interphase TKE (GCG)	0.3549	0.3562
Θ_{ij} (MHC)	0.2219	0.2219
Interphase TKE (MHC)	0.3616	0.3630

the relative magnitude and the anisotropy state of the terms in Eq. 7.11, we can draw the following conclusions:

i) The correlation between the fluctuating velocity and the gradient of viscous stress Θ_{ij} and the interphase TKE transfer term are the dominant terms on the right-hand-side of Eq. 7.11, where Θ_{ij} acts as energy sink and the interphase TKE transfer term is the energy source.

ii) The anisotropic state of the tensor Θ_{ij} and the interphase TKE transfer tensor is characterized by the independent invariants ξ and η. According to the interpretation of the values of (ξ, η) on the Lumley triangle [Pope (1999)], the values of (ξ, η) suggest the degree of anisotropy is higher for the interphase TKE transfer tensor compared to that of Θ_{ij} tensor.

7.5 Discussion

The numerical results discussed in Section 7.4 show increasing fluid phase fluctuations in the fixed bed of spheres with clusters (GCG random particle configuration). The analysis of 2D energy spectrum of GCG and MHC shows that the energy at lower wavenumbers for GCG is higher than that for MHC. The cut-off wavenumber $\kappa_{d_p} \approx 10$. Using the concept of the radius of gyration, the size of particle cluster can be estimated. The particle cluster size of GCG is found to be $2.49d_p$, while the particle size of MHC is found to be $1.55d_p$. The wavenumbers that correspond to MHC and GCG's particle cluster size are 18.5 and 11.5 respectively. The presence of particle clusters in GCG enhances the energy at wavenumbers

smaller than $\kappa_{d_c} = 11$. However the energy spectrum studied is two dimensional, the correlation along the streamwise direction x is not studied. Since the velocity field is not homogeneous along the x direction, other numerical techniques should be used to study the correlation.

The relative magnitudes of Θ and the interphase TKE transfer term in Table 7.5 show that Θ for MHC dissipates more energy compared to that of GCG. It is also observed that GCG's Θ in the second half of the fixed bed is smaller than that of MHC. The increasing TKE along the x direction can be attributed to the term Θ_{ij} in the transport equation of R_{ij}. The gradient of rate-of-strain in the definition of Θ_{ij} is expected to be higher at the front of the sphere, since the flow is blocked at this location. For the fixed bed with the higher level of particle clustering, more spheres are located in the wake region of other spheres. Hence $\partial S_{kj}/\partial x_k$ around these spheres is expected to be smaller, and the magnitude of Θ is smaller for the fixed bed with GCG. Therefore, $\Theta_{ij}(\mathbf{x})$, which is usually modeled as dissipation in the multiphase turbulence models, should consider the particle clustering effect, which is generally left out in the gas-solid turbulence models available in the literature.

Second-order statistics of the particle phase, which is a common way to describe the particle clustering effects, was considered in the modeling of interphase TKE terms in Amhadi's model. The particle clustering effects are not considered in the models for dissipation terms in the existing multiphase turbulence models. The above analysis reveals that the particle clustering effects should be included in the dissipation models.

The discussion of the particle clustering effect on multiphase turbulence models is based on the estimation of the mean quantities in Section 7.4, where the ensemble averaging is used. It is worthwhile to discuss the sample size M on the estimation of the mean quantities. With only 4 MIS, the $\alpha_\beta = \langle I_\beta \rangle$ field is not a smooth field. The central plane of $\alpha_p(\mathbf{x})$ past $y = \mathcal{L}/2$ for 4 MIS of Matérn hard-core is plotted in Figure 7.22, and $\alpha_f(\mathbf{x})$ is just $1 - \alpha_p(\mathbf{x})$. The fluid phase mean velocity $\left\langle U_1^{(f)} \right\rangle$ is not smooth either, as seen in Figure 7.18, which imposes extra difficulty as the mean velocity gradient is required in the quantification of the production $\mathcal{P}_{ij}$.

Since the volume fraction field is not smooth, it is hypothesized that the number of independent runs, or in other words, the sample size of the ensemble averaging is not enough such

that the statistical error is very high and contaminate the estimation of $\alpha_f(\mathbf{x})$. To determine the number of MIS required to reduce the uncertainty in the estimated mean, the following numerical experiment is conducted:

(i) the random point field with Matérn hard-core distribution is generated M times with a certain solid volume fraction;

(ii) the mean $\alpha_p(\mathbf{x})$ is formed using the formulation similar to Eq. 7.5;

(iii) since the random point field with a Matérn hard-core distribution is homogeneous in all directions, the variance of $\alpha_p(\mathbf{x})$ can be calculated and compared with an analytical solution.

One can verify the number of independent simulations required such that the estimated variance of α_p is close to the theoretical value $\alpha_p - \alpha_p^2$.

A Matérn hard-core point field is generated in a cubic box with the solid volume fraction $\alpha_p = 5\%$ and the ratio between the box size and the particle diameter d_p is 12.8. All the parameters of this simulation are exactly the same as those used in the upstream turbulence past a fixed bed of spheres. The middle plane of $\alpha_p(\mathbf{x})$ is plotted with $M = 5$, 50, as seen in Figures 7.23 and 7.24. With the scale of $\alpha_p(\mathbf{x})$ to be 0 and 1, it is observed from these two plots that the central planes of $\alpha_p(\mathbf{x})$ become smooth. Under the condition that the random point process follows the Matérn hard-core distribution, the variance of $\alpha_p(\mathbf{x})$ is plotted in Figure 7.25. The estimated variance of α_p is within 10% of the theoretical value $\alpha_p - \alpha_p^2$ for $M \approx 8$, and 5% of the theoretical value for $M > 20$. Hence, to obtain a better statistical estimation of α_f and α_p at least 8 MIS are needed.

7.6 Summary

In this study, the upstream homogeneous turbulence past a fixed bed of spheres with two particle random arrangements is studied using the immersed boundary method. One of the particle random arrangements is with Matérn hard-core distribution (MHC), where particles distribute uniformly in the space. The other is the clustering state of inelastic granular cooling

gas (GCG). The principal findings from this numerical study are:

i) the fluid phase TKE is enhanced along the streamwise direction inside the fixed bed for GCG. The Reynolds-stress $R_{ij}^{(f)}$ inside the fixed bed becomes anisotropic, and $R_{11}^{(f)}$ is significantly larger than $R_{22}^{(f)}$ and $R_{33}^{(f)}$.

ii) The 2D energy spectra study shows that for GCG the energy at lower wavenumber $\kappa < 10$ is higher than the energy spectra of MHC. The cutoff wavenumber corresponds to the cluster size estimated by the radius of gyration.

iii) The correlation between the fluctuating velocity and the gradient of viscous stress Θ_{ij} and the interphase TKE transfer term are the dominant terms on the right-hand-side of the transport equation for $R_{ij}^{(f)}$, where Θ_{ij} acts as energy sink and the interphase TKE transfer term is the energy source. The analysis of the anisotropic state shows that the degree of anisotropy is higher for the interphase TKE transfer tensor compared to that of Θ_{ij} tensor.

This study suggests that length scales based on cluster size, as opposed to particle size, should be used to estimate the increased levels of gas fluctuations caused by the solid phase. This study also suggests that models that do not consider the effect of the clusters on the gas phase turbulence will not predict the flow dynamics inside the fluidized bed correctly.

The effects of the sample size M are examined Section 7.5. It is noted that with a sample size $M \approx 8$, the sample variance of the volume fraction $\alpha_p(\mathbf{x})$ deviates 10% from the theoretical value of the variance for Matérn hardcore distributions. Since only four samples are used for GCG and MHC respectively in this study, more samples are required to obtained smooth α_p with less statistical errors, and to reduce the uncertainty in the estimation of the ensemble averaged mean velocity field, Reynolds stresses and pressure field.

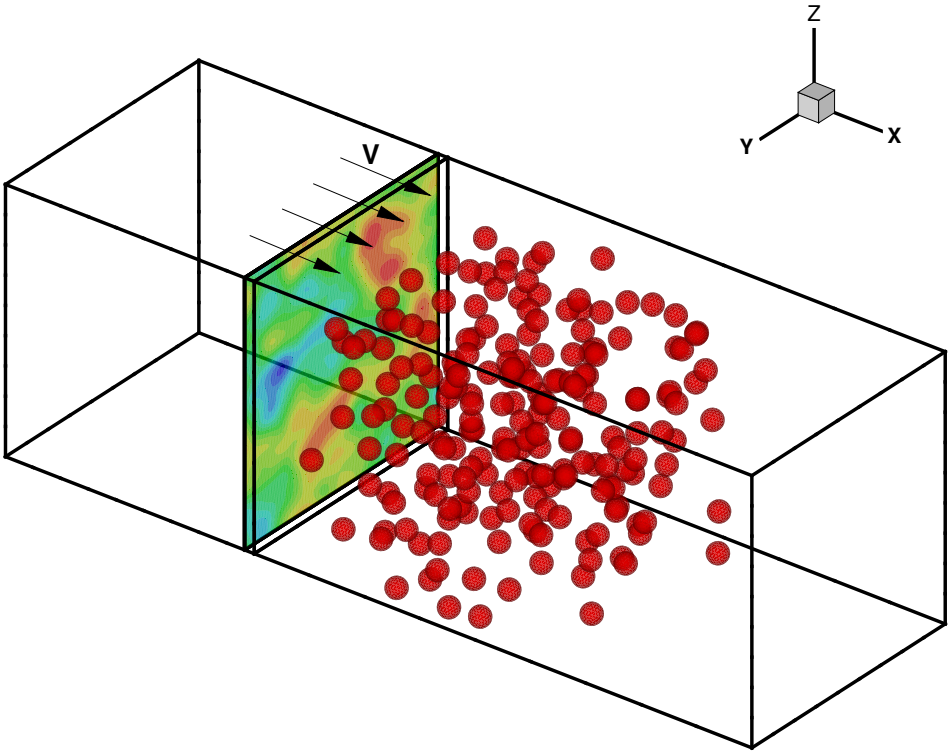

Figure 7.1 The sketch of the flow domain with multiple stationary spheres.

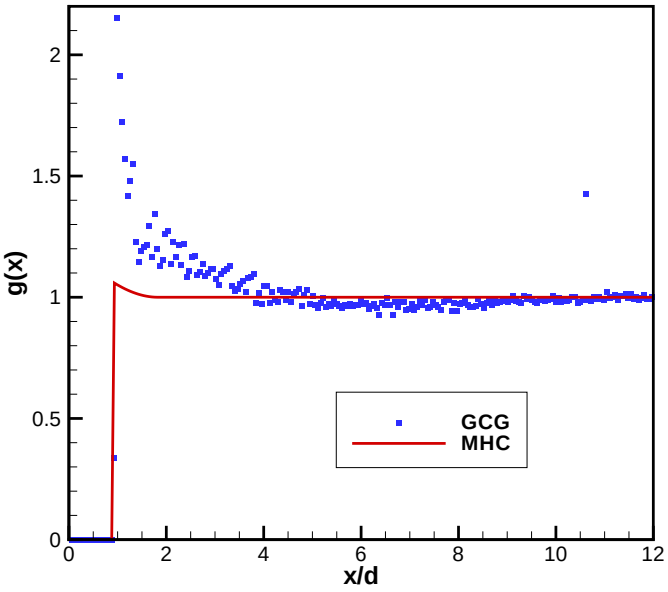

Figure 7.2 The pair correlation for MHC and GCG. The solid line represents the analytical form of the pair correlation for the Matérn hard-core distribution [Stoyan et al. (1986)]. The filled squares represent the pair correlation for the clustering state of inelastic granular cooling gas obtained by calculations.

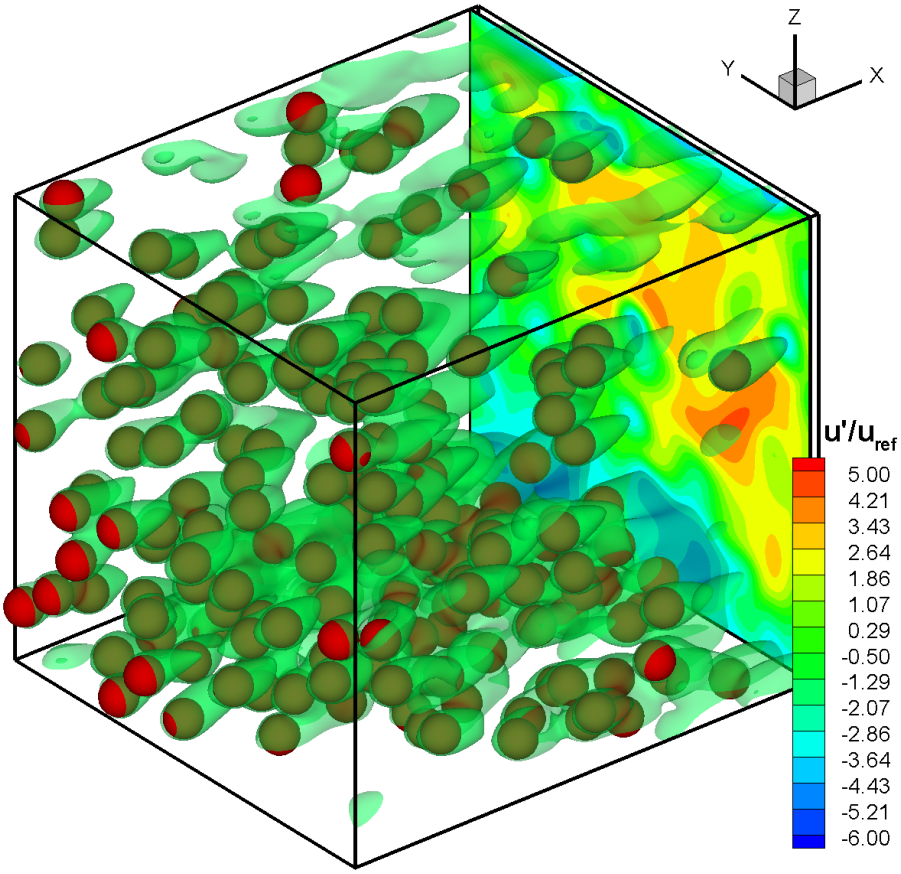

Figure 7.3 The velocity isosurface of the instantaneous velocity field from GCG. The contour plot at the end of the fixed bed is the magnitude of fluctuating velocity $|u'|$. The scale of the contour is the magnitude of fluctuating velocity $|u'|$ normalized by $|u_{ref}| = \sqrt{\frac{2}{3}k_f}$ where k_f is TKE in the isotropic turbulence.

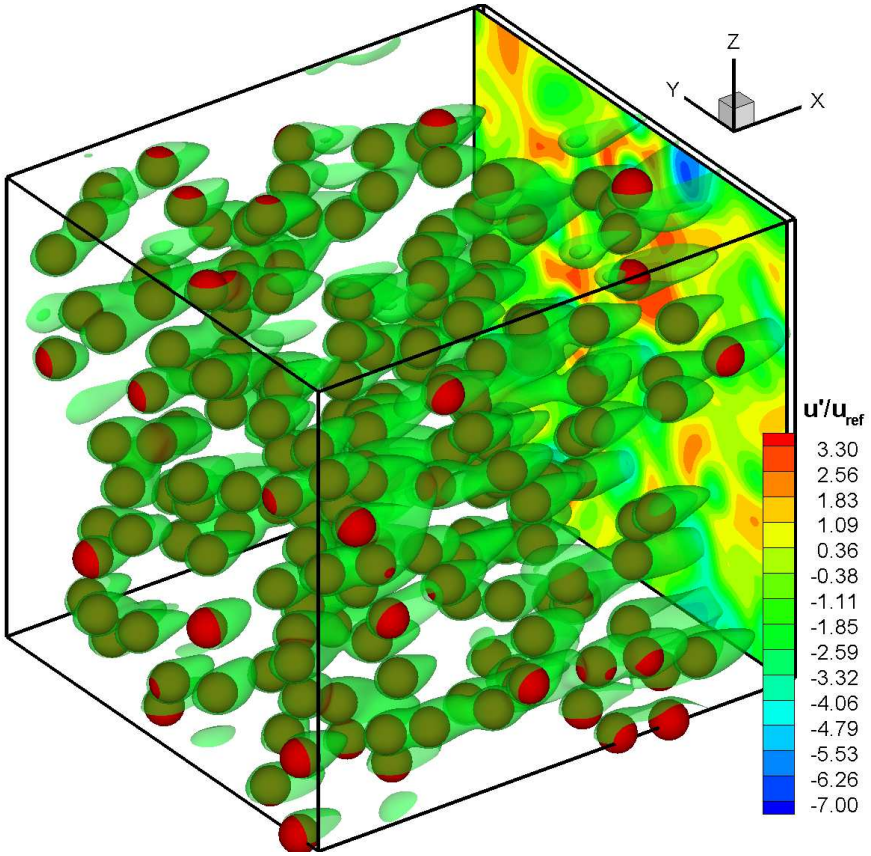

Figure 7.4 The velocity isosurface of the instantaneous velocity field from MHC. The contour plot at the end of the fixed bed is the magnitude of fluctuating velocity $|u'|$. The scale of the contour is the magnitude of fluctuating velocity $|u'|$ normalized by $|u_{ref}| = \sqrt{\frac{2}{3}k_f}$ where k_f is TKE in the isotropic turbulence.

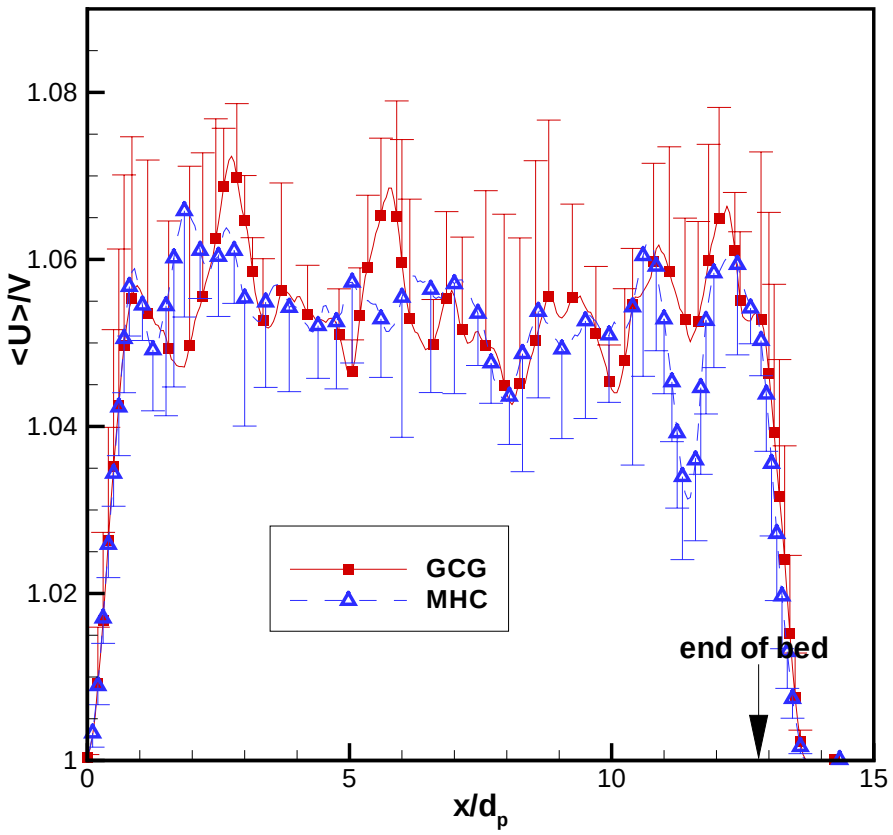

Figure 7.5 The ensemble averaged mean velocity $\{\langle U^{(f)}(x_i)\rangle\}$ for Matérn hardcore and GCG with variation in x direction. The mean velocity is normalized by the mean slip velocity $V = 0.2029$.

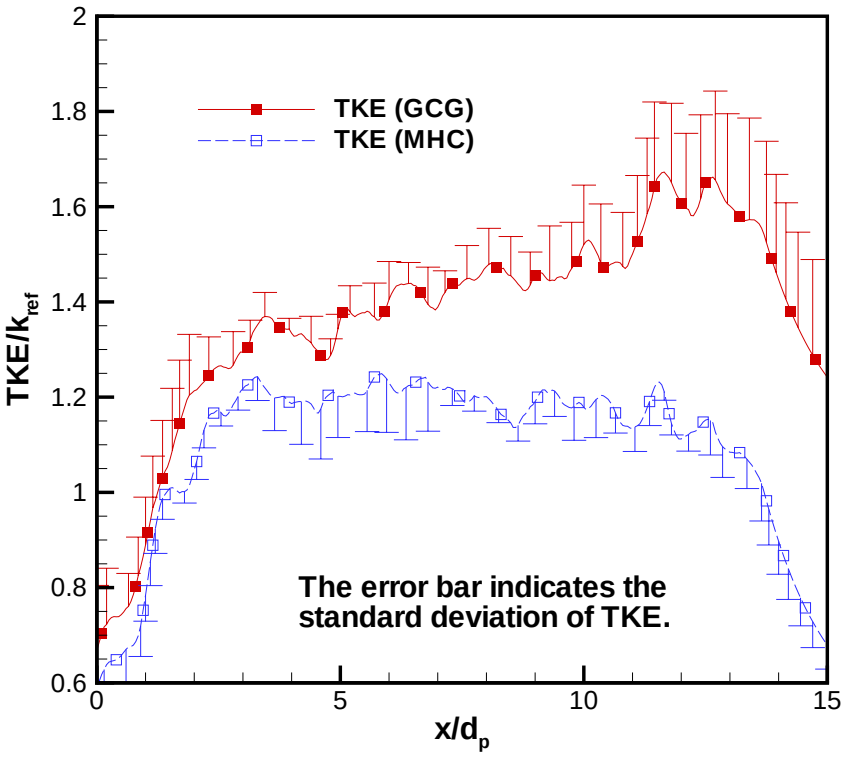

Figure 7.6 The comparison of normalized $k_f(x_i)$ between Matérn hard-core and granular cooling gas. The error bars in the plot indicate the standard deviation of $k_f(x_i)$. k_f is normalized by the TKE in the box turbulence $k_{ref} = 0.002359$.

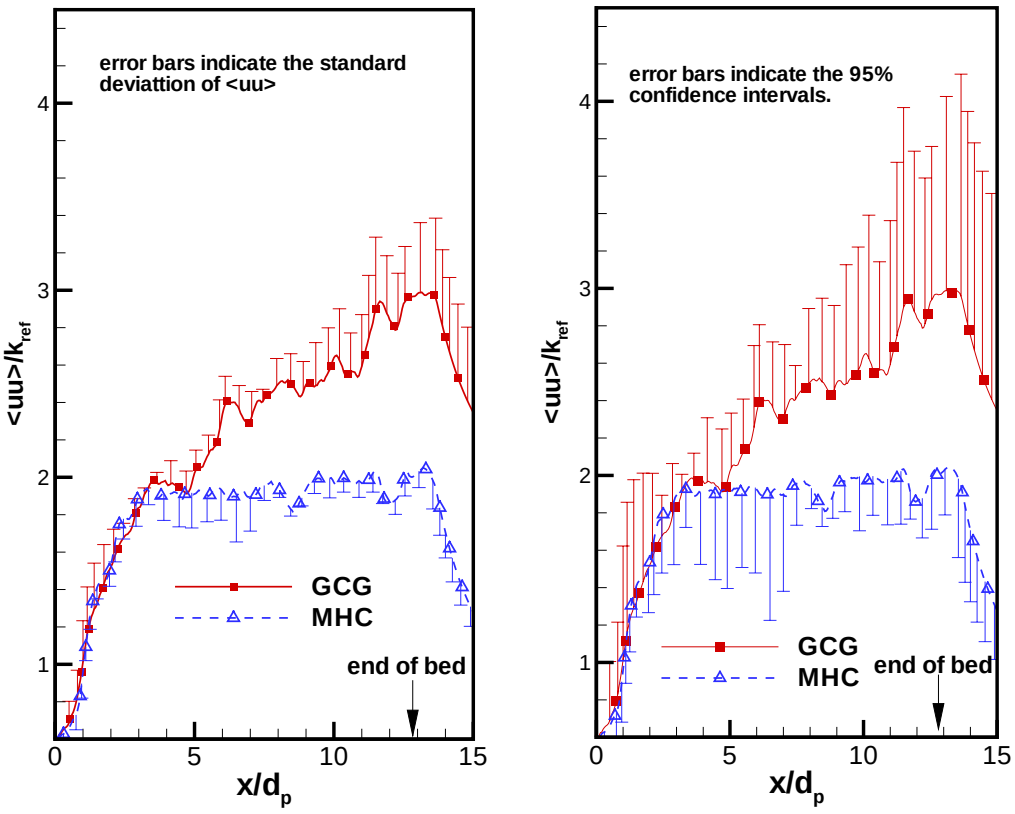

Figure 7.7 The comparison of normalized $\left\{R_{11}^{(f)}(x_i)\right\}$ between Matérn hardcore and granular cooling gas. The error bars in left-hand-side panel indicate the standard deviation of $\left\{R_{11}^{(f)}(x_i)\right\}$, while the error bars on the right-hand-side panel indicates the standard error for 95% confidence interval. The reference value is the TKE in the box turbulence $k_{ref} = 0.002359$.

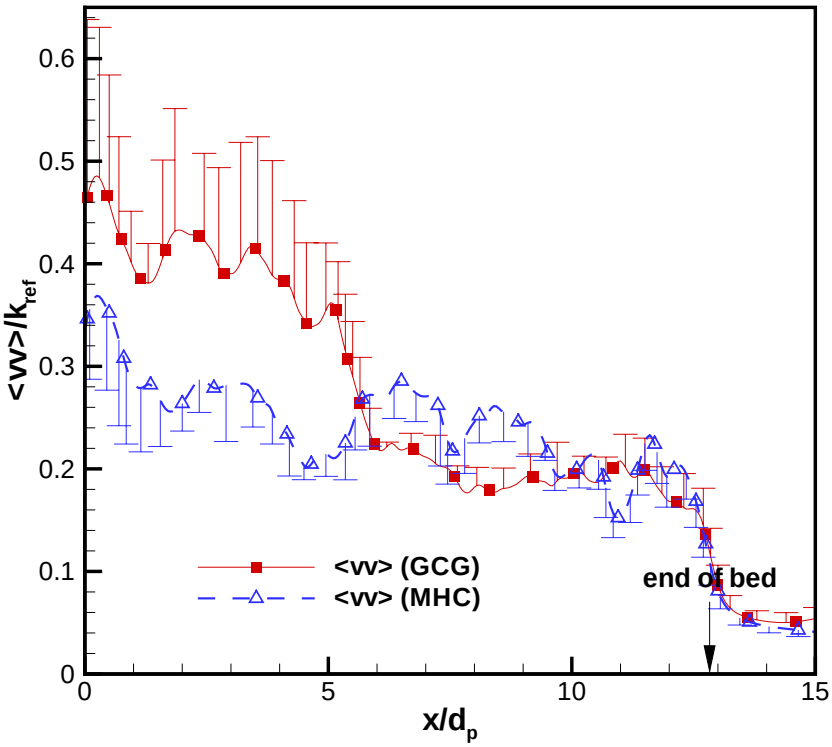

Figure 7.8 The comparison of normalized $\left\{R_{22}^{(f)}(x_i)\right\}_1$ between Matérn hard-core and granular cooling gas. The error bars in the plot indicate the standard deviation of $\left\{R_{22}^{(f)}(x_i)\right\}_1$ for 4 MIS. The reference value is the TKE in the box turbulence $k_{ref} = 0.002359$.

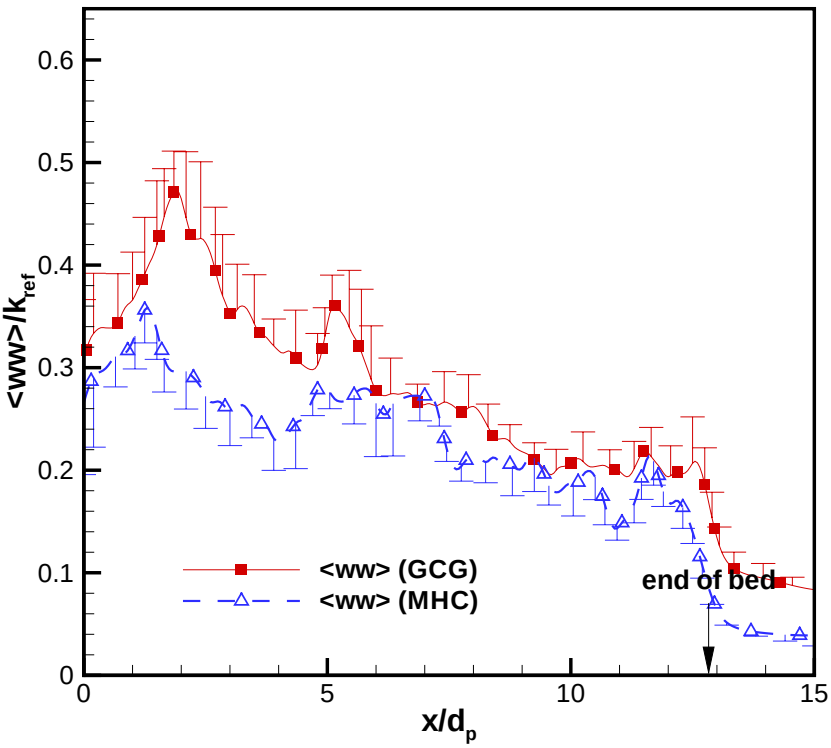

Figure 7.9 The comparison of normalized $\left\{R_{33}^{(f)}(x_i)\right\}$ between Matérn hard-core and granular cooling gas. The error bars in the plot indicate the standard deviation of $\left\{R_{33}^{(f)}(x_i)\right\}$ for 4 MIS. The reference value is the TKE in the box turbulence $k_{ref} = 0.002359$.

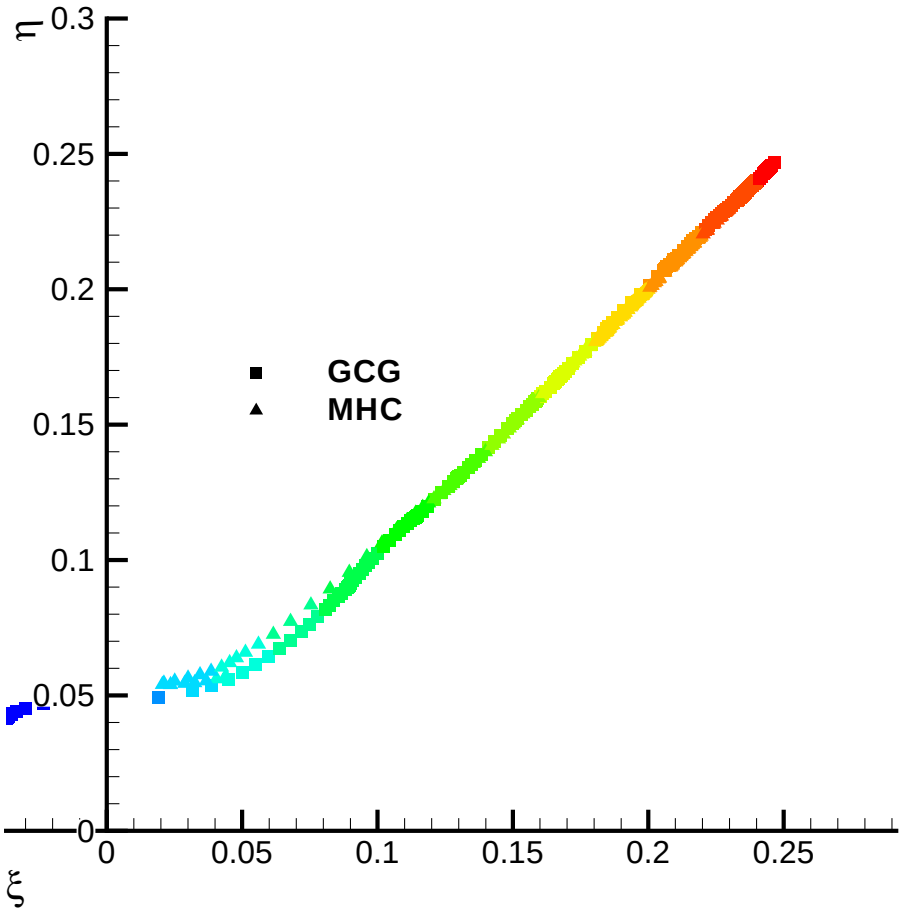

Figure 7.10 The Lumley triangle on the plane of the invariants of ξ and η of the Reynolds stress anisotropy tensor. The color of the symbols from blue to red in the figure indicates the location of the state of anisotropy moving from $x = 0$ to $x = 12.8d_p$.

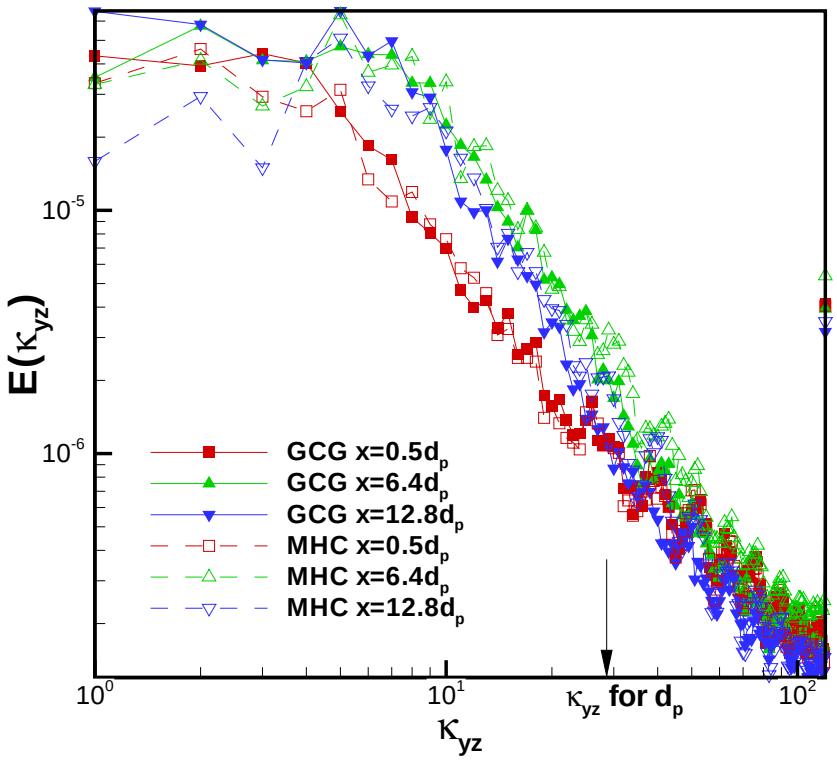

Figure 7.11 The two-dimensional energy spectrum for MHC and GCG and $x = 0.5d_p,\ 6.4d_p,\ 12.8d_p$. κ_{yz} is the magnitude of wavenumber vector in the y-z plane.

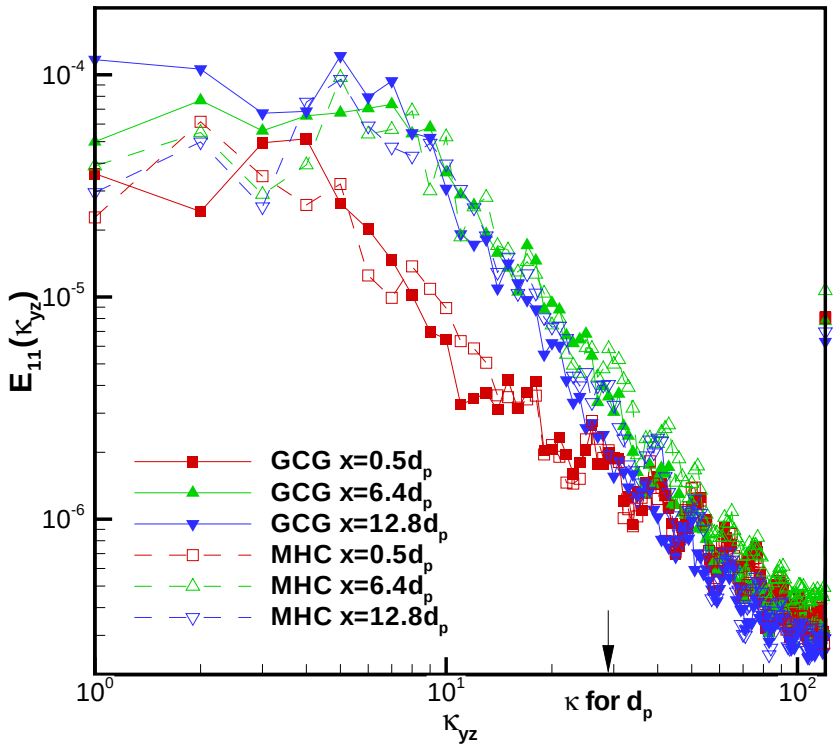

Figure 7.12 The two-dimensional velocity spectrum of $R_{11}^{(f)}$ for MHC and GCG and $x = 0.5d_p,\ 6.4d_p,\ 12.8d_p$. κ_{yz} is the magnitude of wavenumber vector in the y-z plane.

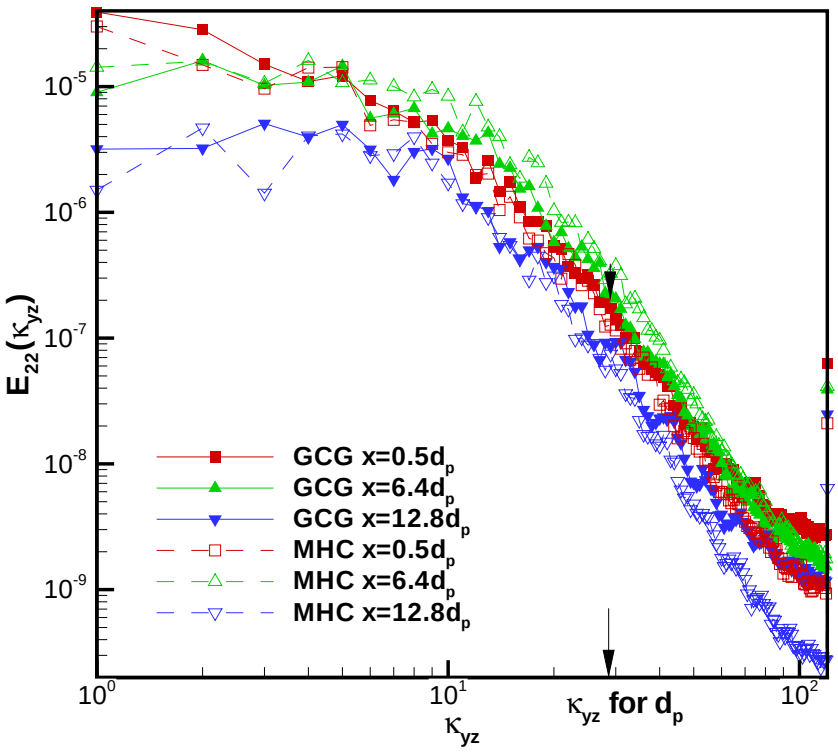

Figure 7.13 The two-dimensional velocity spectrum of $R_{22}^{(f)}$ for MHC and GCG and $x = 0.5d_p,\ 6.4d_p,\ 12.8d_p$. κ_{yz} is the magnitude of wavenumber vector in the y-z plane.

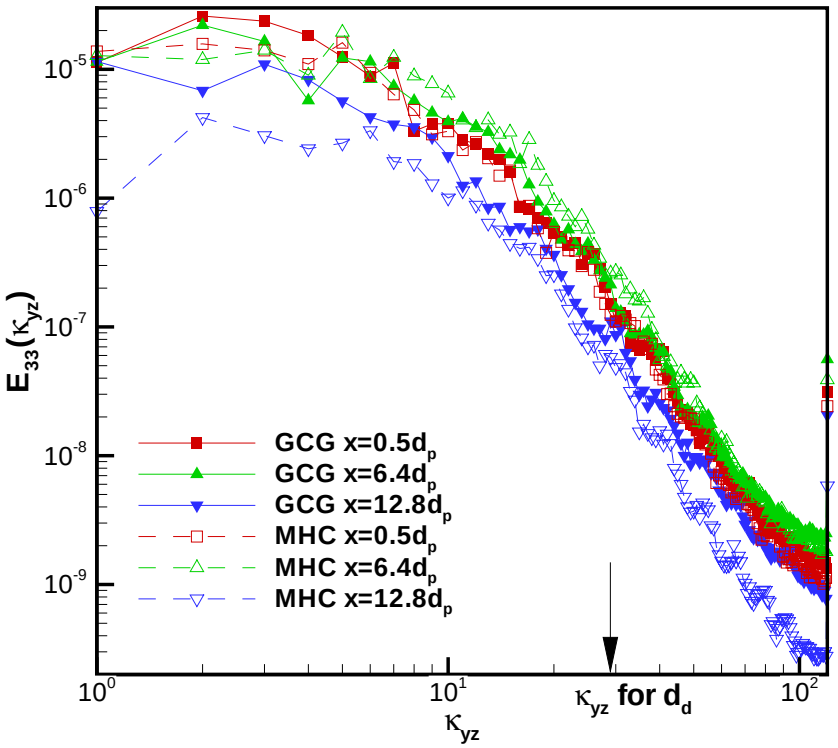

Figure 7.14 The two-dimensional velocity spectrum of $R_{33}^{(f)}$ for MHC and GCG and $x = 0.5d_p,\ 6.4d_p,\ 12.8d_p$. κ_{yz} is the magnitude of wavenumber vector in the y-z plane.

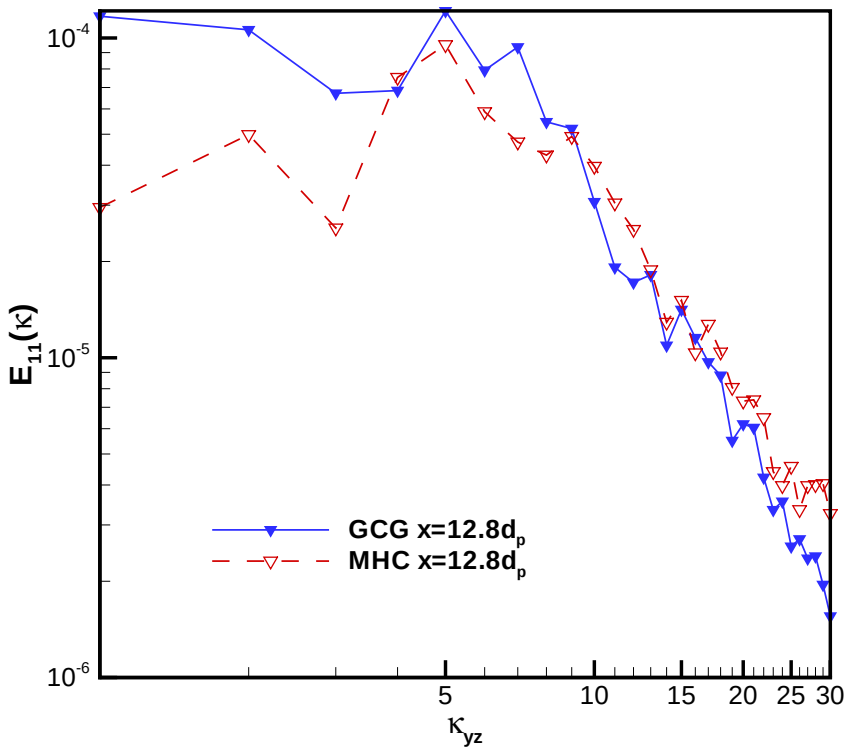

Figure 7.15 The two-dimensional energy spectrum for MHC and GCG and $x = 12.8d_p$ at lower wavenumbers $\kappa_{yz} < 30$. κ_{yz} is the magnitude of wavenumber vector in the y-z plane.

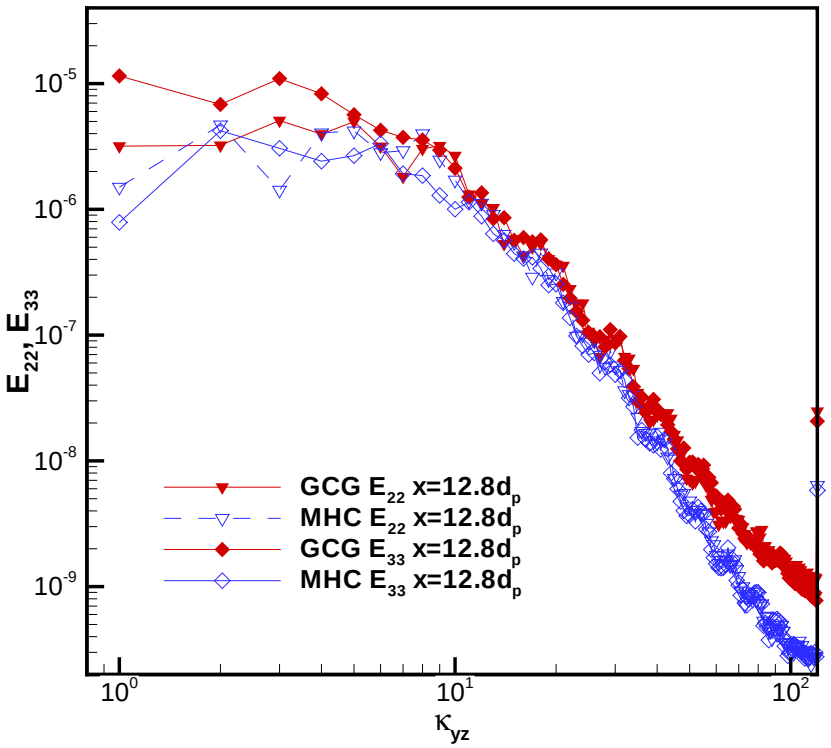

Figure 7.16 The two-dimensional velocity spectrum of $R_{22}^{(f)}$ and $R_{33}^{(f)}$ for MHC and GCG and $x = 12.8d_p$. κ_{yz} is the magnitude of wavenumber vector in the y-z plane.

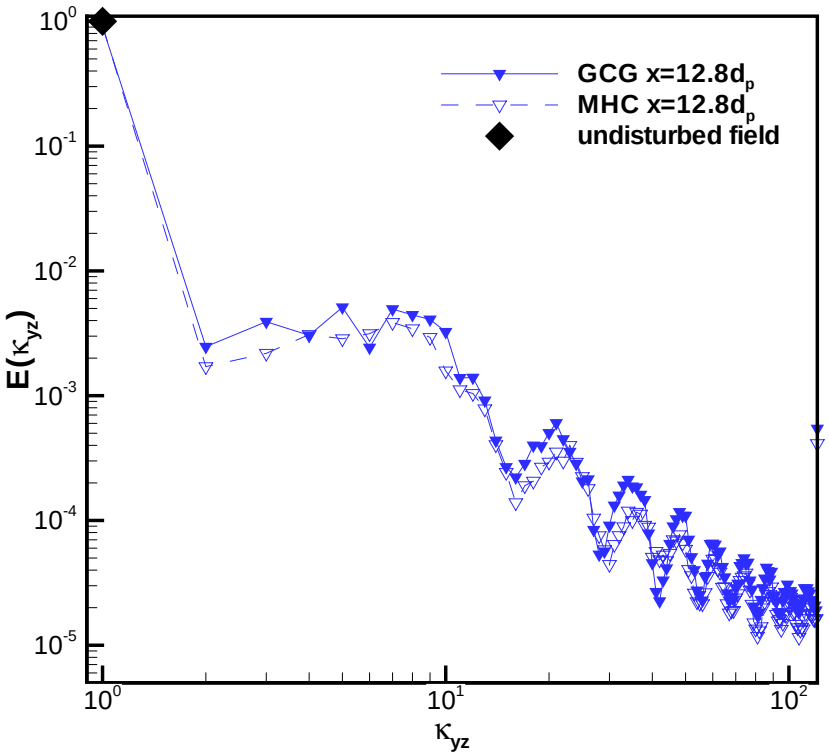

Figure 7.17 The two-dimensional velocity spectrum of the scalar field $f(\mathbf{x})$ multiplying the random point fields $I_f(\mathbf{x})$ from MHC and GCG.

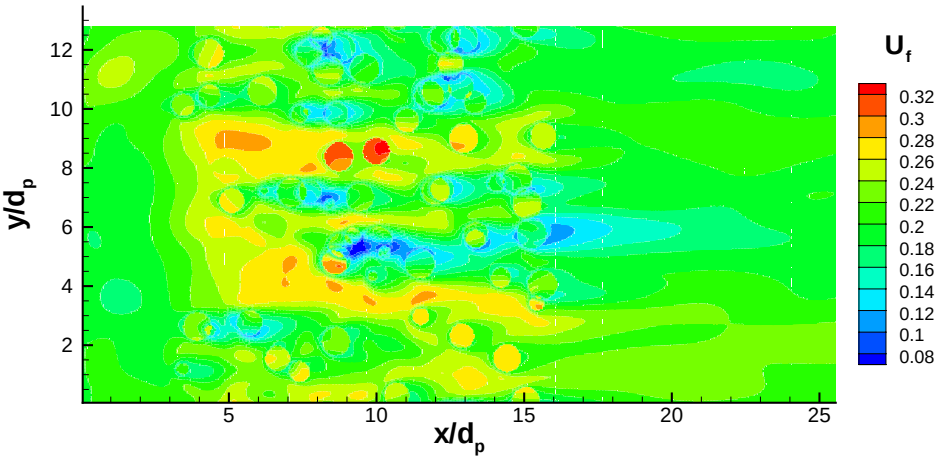

Figure 7.18 The expected mean $\left\langle U_1^{(f)}(\mathbf{x}) \right\rangle$ field from Matérn hard-core distribution used in runs for upstream turbulence past random arrangement of spheres.

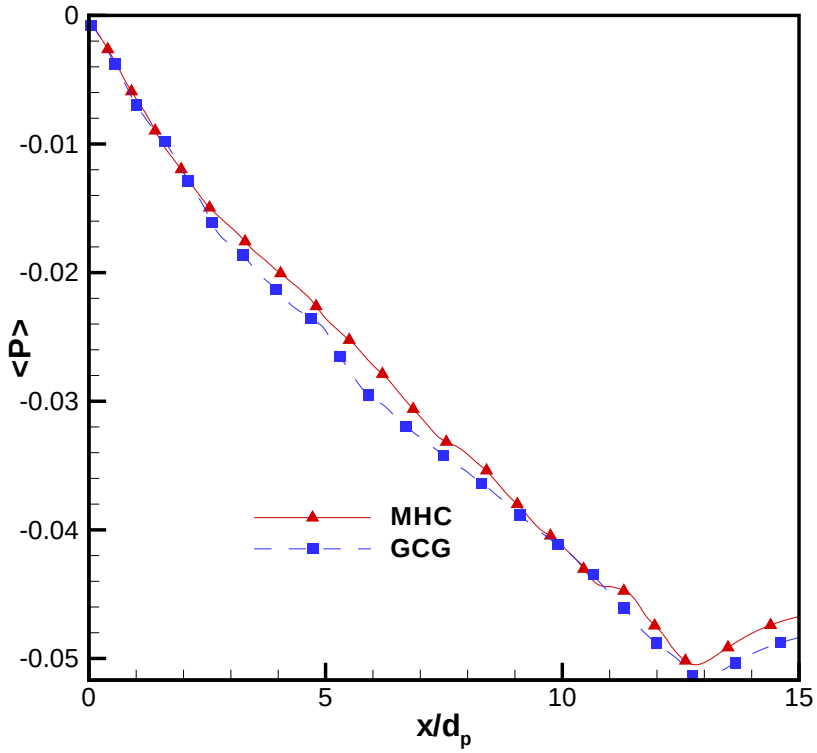

Figure 7.19 The mean pressure inside the fixed bed of spheres for MHC and GCG.

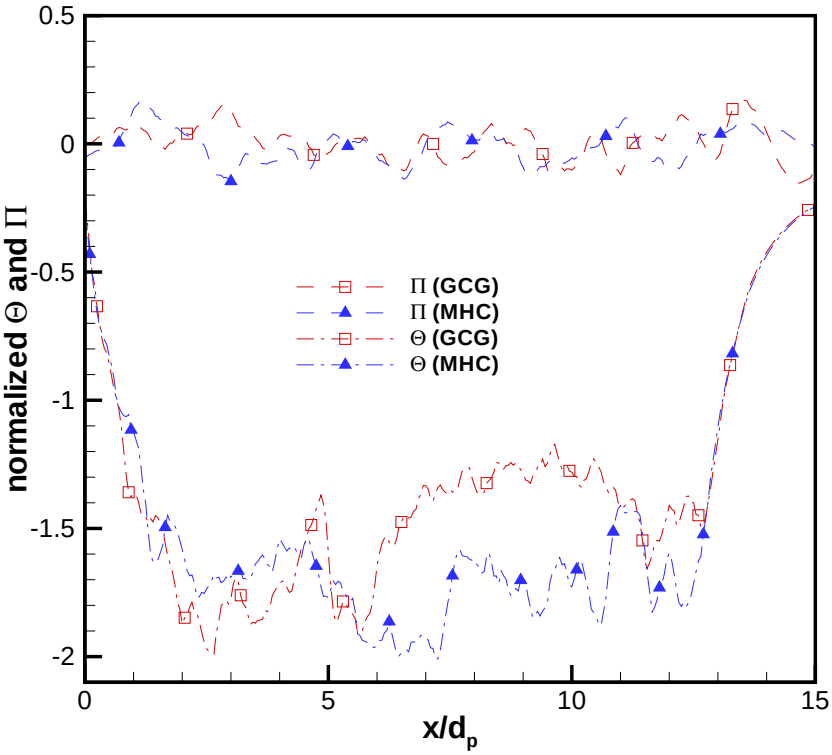

Figure 7.20 The normalized half trace of the second order tensor corresponding to $\Theta = \frac{1}{2}\Theta_{ii}$ and $\Pi = \frac{1}{2}\Pi_{ii}$ inside the fixed bed for MHC and GCG. These terms are normalized by $\frac{Vk_{ref}}{d_p}$, where k_{ref} is the TKE in the upstream homogeneous turbulence, d_p is the particle diameter and V is the mean slip velocity.

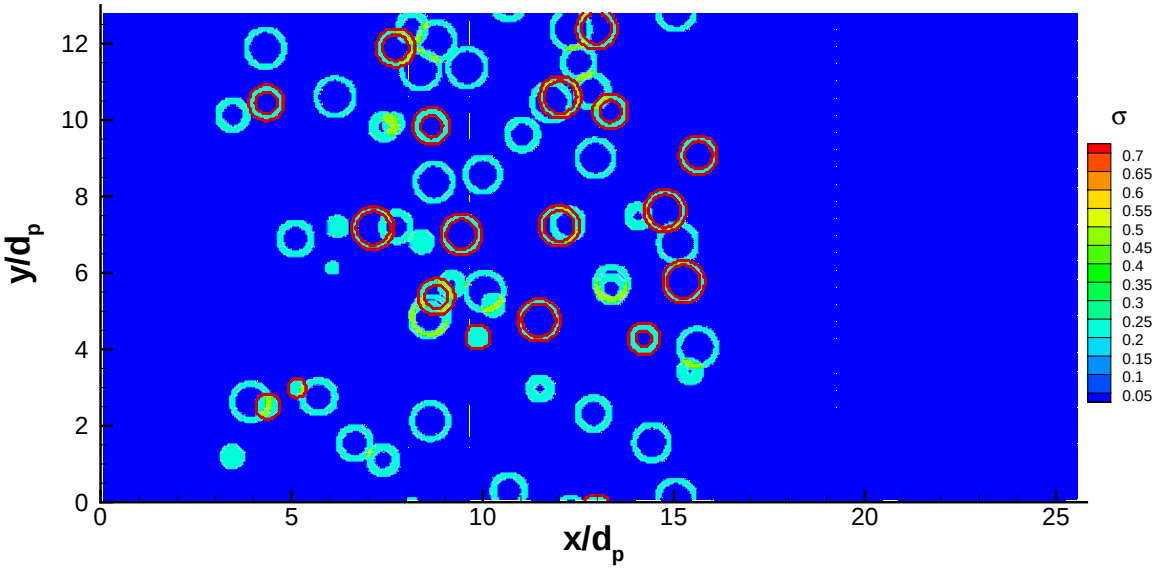

Figure 7.21 The surface area measure $\sigma(\mathbf{x})$ for MHC where the contour field is $\sigma(\mathbf{x})$ and the red line represents the surface area from one run of MHC.

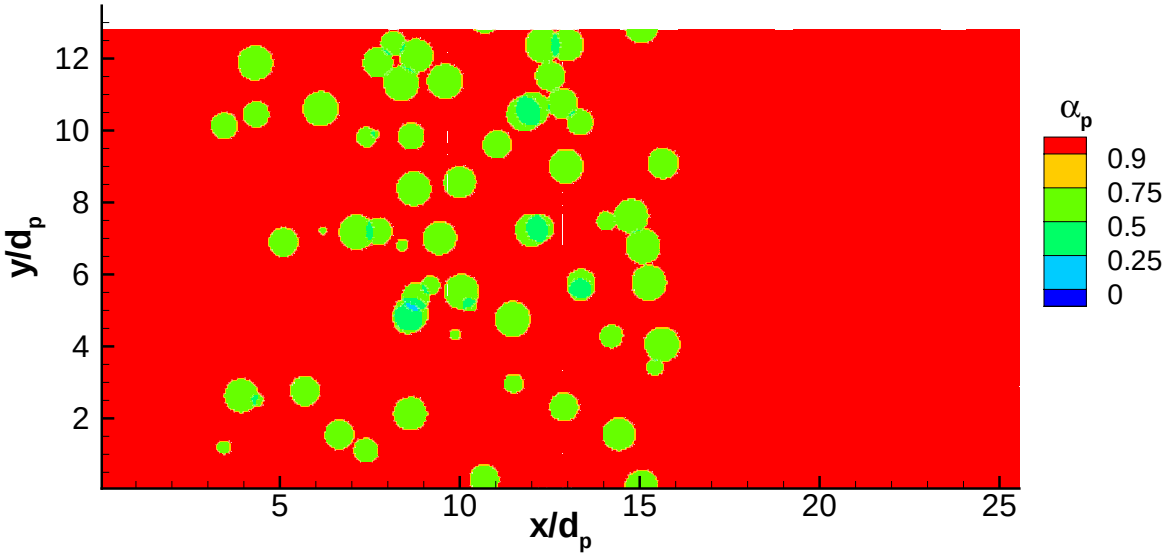

Figure 7.22 The expected mean $\alpha_f(\mathbf{x})$ field from Matérn hard-core distribution used in runs for upstream turbulence past random arrangement of spheres.

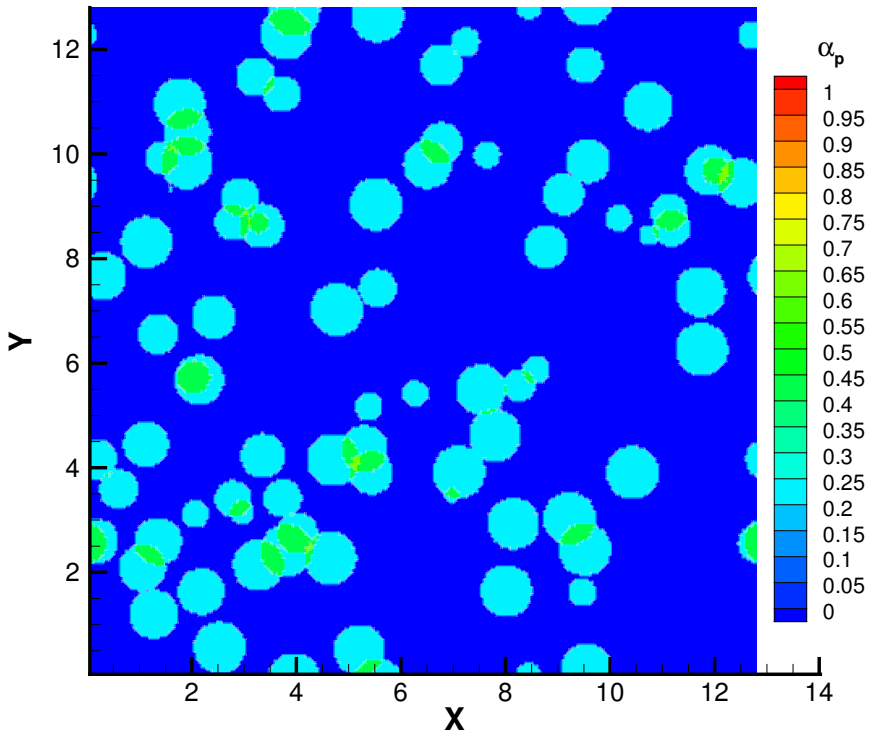

Figure 7.23 The expected mean $I_p(\mathbf{x})$ field from 5 MIS.

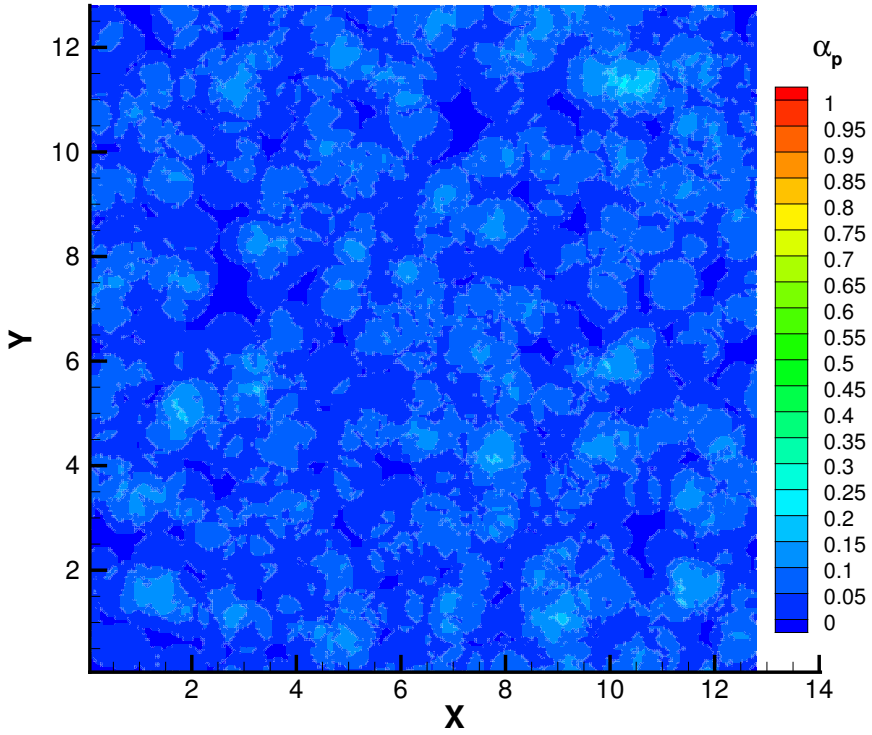

Figure 7.24 The expected mean $I_p(\mathbf{x})$ field from 50 MIS.

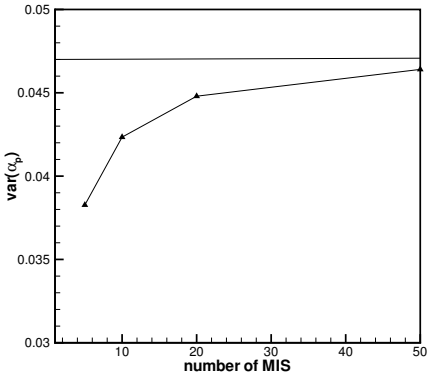

Figure 7.25 The variance of $\alpha_p(\mathbf{x})$ field for Matérn hardcore distribution.

CHAPTER 8. FUTURE WORK

In this chapter, possible future work is discussed. In this research, a new multiphase turbulence model EEM is proposed in Chapter 3, where this model is validated for the canonical problems for particle-laden turbulent flows. However some general modeling issues pertinent to EEM need further study.

The equilibration of energy model (EEM) is validated for dilute particle-laden homogeneous turbulent flows. The validity of EEM for the entire range of parameters, such as the solid volume fraction, the mass loading ratio and the particle Reynolds number needs further investigation. For the dense gas-solid flows, collisions in the particle phase become important and hence the particle energy dissipation through collision should be included in the transport equations for particle phase TKE. The validity of EEM for the inhomogeneous flow cases needs further improvement, even though EEM is validated for the homogeneous shear particle-laden flows by comparing the model predictions with DNS results. EEM should be validated for other inhomogeneous flow cases, such as the particle-laden turbulent pipe flows, for which experimental dataset is available. This brings up the wall boundary conditions required in multiphase turbulence models, which is not studied in this work. Another important physical phenomena found in the gas-solid turbulent flows is the generation of fluid phase TKE due to the large particles. If the particle Reynolds number is considerably larger than one, then wake structures appear behind particles, and fluid phase fluctuation is expected to be generated in these wake regions. This physical phenomena should also be modeled in EEM.

EEM is formulated by considering the behavior of a two–phase flow system in the limit of stationary turbulence. In this limit, the mixture TKE is kept constant by artificially forcing the fluid turbulence in a homogeneous particle–laden turbulent flow. The model parameter C_2

is defined as the ratio of the equilibrium values of particle–phase specific energy $e_f^e = \rho_f \alpha_f k_f$ to the total mixture energy e_m,

$$C_2 = \frac{e_f^p}{e_m}, \quad \frac{e_f^e}{e_m} = 1 - C_2,$$

and C_2 is bounded between 0 and 1. It is hypothesized that C_2 is a strong function of mass loading, and could be a function of the particle Stokes number St , particle Reynolds number Re_p, particle volume fraction and the initial k_f/k_p ratio. Due to the lack of "true" DNS dataset, C_2 is currently modeled as a function of mass loading. The ideal test case for validating C_2 is to perform a "true" DNS for particle–laden turbulence while keeping the mixture energy constant. By varying the particle Stokes number St, particle Reynolds number Re_p, and the initial k_f/k_p ratio, the hypothesis for C_2 could be validated directly, which is referred as *test case A* in this Chapter. The model constant C_π in the interphase TKE transfer terms can also be determined using the dataset from the test case A. Since the mixture TKE is kept constant by artificially forcing the fluid turbulence, the fluid phase viscous dissipation is compensated by the artificial forcing in the fluid turbulence, $\frac{de_m}{dt} = 0$ and $\varepsilon_f = 0$. The temporal evolution of interphase TKE transfer terms can be used to determine C_π once C_2 is determined.

Besides using "true" DNS to determine the model coefficient of EEM, other test case can be designed to improve the multiphase turbulence model. EEM is validated with DNS dataset using the point-particle approximation. As it is discussed earlier, the dissipation rate reported in point–particle DNS is not the "true" dissipation rate, since particles are modeled as point force in the flow field and the boundary layer around each particle is not fully resolved. The results from the experimental study for particle–laden homogeneous turbulence [Hwang and Eaton (2006a)] indicate that the point–particle DNS is not able to obtain the amount of TKE attenuation observed in experiments. In another words, the fluid dissipation rate captured in point–particle DNS is smaller than those observed in experiments. If a "true" DNS for particle–laden decaying homogeneous turbulence is performed where the parameters are similar to those in Collin's DNS study, we can obtain the dissipation rate ε_f^t. The dissipation model of EEM is currently the model for the single phase ε_f with addition of interphase exchanges. With ε_f^t calculated from "true" DNS, a better dissipation model can be built for EEM.

As it is discussed in Chapter 5 and 6, "true" DNS using the immersed boundary method is computationally expensive. The idea using "true" DNS dataset to determine the model coefficients C_2 and C_π in EEM cannot be achieved right now. With the limited computational resource, the modulation of fluid phase TKE with particle clustering effects is studied in Chapter 7, where the particle clustering effect is a second-order statistics of particle phase and is not directly connected to the study of determining the model parameters in EEM. If the spheres in the fixed bed start to move and respond to the surrounding flow field, the additional numerical issues need to be addressed with the immersed boundary method are:

(i) when particles come close and the inter–particle distance becomes less than several grid points, the lubrication force need to be incorporated;

(ii) when particles collide, the hard-sphere model or soft-sphere collision needs to be considered.

Once these numerical issues are addressed and the simulator is validated with experimental and numerical benchmarks for moving particles in the turbulent flow field, the model coefficients for EEM can be determined. To simulate test case A, we also need a forcing scheme that can compensate the energy loss in the mixture energy. From the 2D energy spectra studied in Chapter 7, it is noted that the fluid phase energy spectrum from the immersed boundary method has wiggles, which imposed extra difficulties in developing the forcing scheme that keeps the mixture energy constant.

APPENDIX A. THE SERIAL ALGORITHM FOR THE IMMERSED BOUNDARY METHOD

A.1 Serial Algorithm for Step 1: the Nonlinear Term Calculation

The nonlinear term has three components:

$$S_x = \frac{\partial uu}{\partial x} + \frac{\partial uv}{\partial y} + \frac{\partial uw}{\partial z}, \tag{A.1}$$

$$S_y = \frac{\partial uv}{\partial x} + \frac{\partial vv}{\partial y} + \frac{\partial vw}{\partial z}, \tag{A.2}$$

$$S_z = \frac{\partial wu}{\partial x} + \frac{\partial wv}{\partial y} + \frac{\partial ww}{\partial z}. \tag{A.3}$$

Since all the velocity components are in Fourier space, the calculation of $\tilde{u}\tilde{u}$ in Fourier space should be evaluated using convolution representation. To avoid the expensive convolution, the velocity components $\tilde{u}$ $\tilde{v}$, and $\tilde{w}$ are all transformed into real space. The velocity calculations are performed in real space and then transformed back to Fourier space. Partial derivatives in y and z are all evaluated using wave numbers. The second order central difference stencil is used to approximate the partial derivatives in x. Hence, the nonlinear terms are eventually evaluated as follows:

$$\begin{aligned}
\tilde{S_x} &= \frac{(\widetilde{uu})_{i+1} - (\widetilde{uu})_{i-1}}{2\Delta x} + \iota\kappa_y (\widetilde{uv})_i + \iota\kappa_z (\widetilde{uw})_i, \\
\tilde{S_y} &= \frac{(\widetilde{uv})_{i+1} - (\widetilde{uv})_{i-1}}{2\Delta x} + \iota\kappa_y (\widetilde{vv})_i + \iota\kappa_z (\widetilde{vw})_i, \\
\tilde{S_z} &= \frac{(\widetilde{uw})_{i+1} - (\widetilde{uw})_{i-1}}{2\Delta x} + \iota\kappa_y (\widetilde{vw})_i + \iota\kappa_z (\widetilde{ww})_i,
\end{aligned}$$

where the subscript i represents the grid index for the x direction.

The nonlinear term Sx is evaluated as follows:

for $i = 1$ to NX **do**

a) backward 2D Fourier transform velocity $\tilde{u}$ $\tilde{v}$, $\tilde{w}$ at i^{th} plane to real space

b) form uu, uv, and uw in the real space

c) forward 2D Fourier transform uu, uv and uw to Fourier space

d) $\tilde{S}_{xi} = \iota\kappa_y \left(\widetilde{uv}\right)_i + \iota\kappa_z \left(\widetilde{uw}\right)_i$

e) $\left(\tilde{S}_x\right)_{i-1} = \left(\tilde{S}_x\right)_{i-1} + \dfrac{\left(\widetilde{uv}\right)_i}{2\Delta x}$

f) $\left(\tilde{S}_x\right)_{i+1} = \left(\tilde{S}_x\right)_{i+1} - \dfrac{\left(\widetilde{uv}\right)_i}{2\Delta x}$

end for

A.2 Serial Algorithm for Step 2: the Forcing Function Calculation

The calculation of the forcing function for N_p particles is performed as follows.

for $j = 1$ to N_p **do**

for $i1$ to N_s **do**

a) Find the neighboring points' location;

b) obtain $\mathbf{u}^n$, $\frac{1}{\rho}\nabla P$, $\mathbf{S}$ and $\nabla^2\mathbf{u}^n$ at the neighboring points;

c) interpolate $\mathbf{u}^n$, $\frac{1}{\rho}\nabla P$, $\mathbf{S}$ and $\nabla^2\mathbf{u}^n$ to the interface point x_p;

d) use forcing function Eq. 5.33 to evaluate forcing $\mathbf{f}$ at the surface point;

e) interpolate $\mathbf{f}$ on the surface point $\mathbf{x}_p$ back to the neighboring grid points.

end for

end for

The forcing $\mathbf{f}$ is calculated in real space; therefore, the velocity $\mathbf{u}^n$, pressure gradient $\dfrac{1}{\rho}\nabla P$, and nonlinear terms $\mathbf{S}$ and $\nabla^2\mathbf{u}^n$ are in real space. Details of the above steps are explained below.

Step a. We explain the finding neighboring points using the two dimensional case, since the three dimensional case will be similar.

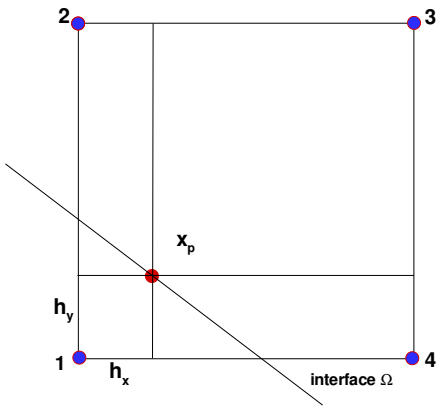

Figure A.1 2-D neighboring point calculation.

$$
\begin{aligned}
x_1 &= \left\lfloor \frac{x_p}{\Delta x} \right\rfloor \quad & y_1 &= \left\lfloor \frac{y_p}{\Delta x} \right\rfloor \\
x_2 &= \left\lfloor \frac{x_p}{\Delta x} \right\rfloor \quad & y_2 &= \left\lceil \frac{y_p}{\Delta x} \right\rceil \\
x_3 &= \left\lceil \frac{x_p}{\Delta x} \right\rceil \quad & y_3 &= \left\lfloor \frac{y_p}{\Delta x} \right\rfloor \\
x_4 &= \left\lceil \frac{x_p}{\Delta x} \right\rceil \quad & y_4 &= \left\lceil \frac{y_p}{\Delta x} \right\rceil
\end{aligned}
$$

where $\lfloor \cdot \rfloor$ is the floor function for a real number and $\lceil \cdot \rceil$ is the ceiling function. Δx is the grid spacing for the uniform Cartesian grids. Hence, $h_x = \left(\frac{x_p}{\Delta x} - \left\lfloor \frac{x_p}{\Delta x} \right\rfloor \right) \Delta x$, and $h_y = \left(\frac{y_p}{\Delta x} - \left\lfloor \frac{y_p}{\Delta x} \right\rfloor \right) \Delta x$.

Step b. From the results in step a, now calculate $\mathbf{u}^n$, $\frac{1}{\rho}\nabla P$, $\mathbf{S}$ and $\nabla^2 \mathbf{u}^n$ at the neighboring points.

Step c. The interpolation of $\mathbf{u}^n$, $\frac{1}{\rho}\nabla P$, $\mathbf{S}$ and $\nabla^2 \mathbf{u}^n$ to the interface point x_p can now be performed as follows. The following two-dimensional linear interpolation scheme is used

$$
u(x_p) = \left[(\Delta x - h_x)(\Delta x - h_y) u_1 + h_x h_y u_3 + (\Delta x - h_x) h_y u_2 + h_x (\Delta x - h_y) u_4 \right] \frac{1}{\Delta x^2} \qquad \text{(A.4)}
$$

where the subscript of u denotes the velocity value at the corresponding point in Figure A.1, and u_p represents the velocity at surface point x_p. Using this interpolation scheme, the point

1 in Figure A.1 which is closest to xp will have the largest weight

$$(\Delta x - h_x)(\Delta x - h_y)/\left(\Delta x^2\right) \tag{A.5}$$

Point 3 which is furthest from the surface point xp has the smallest weight

$$h_x h_y/\left(\Delta x^2\right) \tag{A.6}$$

Step d. Using the results of step c and using Eq. 5.33, calculate the forcing function $\mathbf{f}$ at the surface point.

Step e. Using the results of step d, interpolate $\mathbf{f}$ on the surface point x_p back to the neighboring grid points as follows.

$$\mathbf{f}_1 = \mathbf{f}(x_p)(\Delta x - h_x)(\Delta x - h_y)/(\Delta x)^2,$$

$$\mathbf{f}_2 = \mathbf{f}(x_p)(\Delta x - h_x)h_y/(\Delta x)^2,$$

$$\mathbf{f}_3 = \mathbf{f}(x_p)h_x h_y/(\Delta x)^2,$$

$$\mathbf{f}_4 = \mathbf{f}(x_p)h_x(\Delta x - h_y)/(\Delta x)^2.$$

APPENDIX B. PARALLELIZATION OF STEP 1: THE NONLINEAR TERM CALCULATION

Since the domain decomposition along the x direction is used, the nonlinear term Sx is evaluated on the rank k process as follows:

call *mpi_irecv* to receive data from rank $k-1$

call *mpi_irecv* to receive data from rank $k+1$

for $i = 1$ to loc_NX **do**

backward 2D Fourier transform velocity $\tilde{u}$ $\tilde{v}$, $\tilde{w}$ at i^{th} plane to real space

form (uu), (uv) and (uw) in the real space

forward 2D Fourier transform uu, uv and uw to Fourier space $\widetilde{uu}$, $\widetilde{uv}$ and $\widetilde{uw}$.

$\tilde{S}_{xi} = \iota\kappa_y \left(\widetilde{uv}\right)_i + \iota\kappa_z \left(\widetilde{uw}\right)_i$

if $i \neq loc\_NX$ **then**

$$\left(\tilde{S}_x\right)_{i+1} = \left(\tilde{S}_x\right)_{i+1} - \frac{\left(\widetilde{uu}\right)_i}{2\Delta x}$$

end if

if $i \neq 1$ **then**

$$\left(\tilde{S}_x\right)_{i-1} = \left(\tilde{S}_x\right)_{i-1} + \frac{\left(\widetilde{uu}\right)_i}{2\Delta x}$$

end if

if $i = 1$ **then**

use MPI_ISEND to send $\widetilde{uu}$ to rank k-1

end if

if $i = loc\_NX$ **then**

use MPI_ISEND to send $\widetilde{uu}$ to rank k+1

end if

end for

call *mpi_waitall*

for $\widetilde{uu}$ received from rank $k+1$, $\left(\tilde{S}_x\right)_{loc\_NX} = \left(\tilde{S}_x\right)_{loc\_NX} + \dfrac{(\widetilde{uu})}{2\Delta x}$

for $\widetilde{uu}$ received from rank $k-1$, $\left(\tilde{S}_x\right)_1 = \left(\tilde{S}_x\right)_1 + \dfrac{(\widetilde{uu})}{2\Delta x}$

APPENDIX C. ESTIMATIONS OF MEMORY REQUIREMENTS FOR THE IMMERSED BOUNDARY METHOD

The resolution of the smallest motions, characterized by the Kolmogorov scale η, demands sufficiently small grid spacing $\Delta x/\eta$, or correspondingly, a sufficiently large maximum wavenumber κ_{max} when solving the Navier-Stokes equations in Fourier space. Experience shows that $\kappa_{max}\eta \geq 1.5$ is the criterion for good resolution of the dissipative length scales. The other spatial resolution requirement that the box size $\mathcal{L}$ large enough to hold the energy–containing motions, can be represented by the relation between $\mathcal{L}$ and the integral length scale L_{11}, and $\mathcal{L} = 8L_{11}$. This requirement is not easy to use in the study of the numerical resolution requirement, since L_{11} can be obtained accurately by integrating the two–point correlation function $f_r(x)$. The approximation that L_{11}/L (where $L = k_f^{3/2}/\varepsilon_f$) has asymptotic value 0.43 is only valid at very high Reynolds number. An alternative constraint for resolving large scale motions in turbulence is that the length scale characterizing the large eddies should be smaller than box size $\mathcal{L}$. One good candidate for the length scale characterizing the large eddies is $L = k_f^{3/2}/\varepsilon_f$.

The true DNS with exact no-slip, no-penetration boundary conditions imposed on each particle, put more constraints on the resolution requirements. One is that there are sufficient number of grids to resolve the boundary layer around each particle. The scaling for boundary layer states that $\delta/d \sim 1/\sqrt{Re_p}$, where δ is length scale for boundary layer and d is the diameter for particles. For the uniform grid size, if 5 grid points are used to resolve the boundary layer around each particle, for $Re_p = 50$, then the scaling requires at least 35 grid points for the particle diameter. The resolution requirements for particle–laden turbulent flows can be summarized as:

1. $\kappa_{max}\eta > 1.5$,

2. $\mathcal{L} > L = k^{2/3}/\varepsilon$,

3. $\Delta x/\delta < \frac{1}{2}$.

The important non-dimensional parameters for particle–laden turbulence are Re_p, u'/U and Re_λ, where $Re_\lambda = \dfrac{u'\lambda_g}{\nu}$ is the Taylor micro-scale Reynolds number. If the CFB, or FCC riser is the corresponding physical system for the DNS study, then the particle Reynolds number Re_p, and upstream turbulent intensity are specified. Since

$$Re_\lambda = \frac{u'\lambda_g}{\nu} = \mathrm{Re}_p \frac{u'}{U}\frac{\lambda_g}{d} = Re_p \frac{u'}{U}\frac{\lambda_g}{\eta}\frac{\eta}{d},$$

the free parameter left is the ratio between particle size d and some length scale from isotropic turbulence, for example, $\dfrac{\lambda_g}{d}$ or $\dfrac{\eta}{d}$. For isotropic turbulence, the relations between micro-scales in homogeneous turbulence are given by

$$\lambda_g/L = \sqrt{10} Re_L^{-1/2}, \tag{C.1}$$

$$\eta/L = Re_L^{-3/4}. \tag{C.2}$$

Then for some $\dfrac{\eta}{d}$,

$$Re_\lambda = \left(Re_p \frac{u'}{U}\frac{\eta}{d}\right)^2 \sqrt{15}. \tag{C.3}$$

To satisfy the third requirement, $L < \mathcal{L}$, substitute Eq. C.3 in Eq. C.1 and use the fact that $Re_\lambda = \sqrt{\dfrac{20}{3} Re_L}$, the following relation can be obtained:

$$L = \eta Re_L^{3/4} = \eta \left(\frac{3}{20}\right)^{3/4} Re_\lambda^{3/2} < \mathcal{L},$$

$$\left(Re_p \frac{u'}{U}\right)^3 \left(\frac{\eta}{d}\right)^4 \left(\frac{3}{2}\right)^{3/2} < \mathcal{L}/d \tag{C.4}$$

$$\frac{\eta}{d} Re_\lambda^{3/2} \left(\frac{3}{20}\right)^{3/4} < \mathcal{L}/d \tag{C.5}$$

One can understand the inequalities from two perspectives:

1. for fixed grid resolution for particle diameter and total number of grid points N for the domain ($\mathcal{L}/d$ known), one can choose η/d to satisfy the resolution requirement in Eq.

C.4. The following table lists the maximum η/d ratio for $\mathcal{L}/d = 10$ with variation of Re_p and u'/U, where $\mathcal{L}/d = 10$ means that if N=200, 20 grid points are used to represent the particle in the flow field.

Table C.1 The maximum η/d ratio for $\mathcal{L}/d = 10$ with variation of Re_p and u'/U.

Re_p	20	20	20	50	50	50
u'/U	10%	20%	30%	10%	20%	30%
η/d	1/1.5	1/1.85	1/2.5	1/3	1/5	1/6.19
Re_λ	15.5	18.0	22.0	24.7	35.0	40.4
λ_g/d	5.2	4.5	3.6	3.3	2.3	2.0

2. This inequality can also be used to estimate $\mathcal{L}/d$ ratio for specified Re_p, u'/U, Re_λ. First substitute Re_p, u'/U, Re_λ in Eq. C.3 to obtain η/d,

$$\frac{\eta}{d} \sim \frac{Re_\lambda^{1/2}}{Re_p \frac{u'}{U}}$$

then Eq. C.5 gives the lower bound for $\mathcal{L}/d$ ratio.

In the single phase DNS, N is scaled as

$$N \sim 1.6 \left(\frac{L}{\eta}\right) = 1.6 Re_L^{3/4} \approx Re_\lambda^{3/2}.$$

The similar scaling can be obtained for $N = \mathcal{L}/\Delta x$ in particle–laden turbulence DNS

$$N = \frac{\mathcal{L}}{\Delta x} = \frac{\mathcal{L}}{d}\frac{d}{\delta}\frac{\delta}{\Delta x} \sim \left(\frac{\eta}{d}\right) Re_\lambda^{3/2} \sqrt{Re_p} \frac{\delta}{\Delta x} \sim \frac{Re_\lambda^2}{Re_p^{1/2}\frac{u'}{U}}. \tag{C.6}$$

The additional $Re_\lambda^{1/2}$ in the estimation for N is due to η/d ratio. $\kappa_{max}\eta$ in this case is much larger than the lower bound 1.5 . In another words, the dissipative scale is over-resolved. The requirement of $\kappa_{max}\eta \geq 1.5$ corresponds to the grid spacing in physical space as

$$\frac{\Delta x}{\eta} = \frac{2\pi}{1.5} \approx 2.1$$

If $d/\eta = 4$ and using 20 grid points to represent the particle, then $\Delta x/\eta = 0.2$ and $\kappa_{max}\eta = 5\pi$ if the domain length is 2π. The following table gives the estimation for N for $Re_p = 50$, $u'/U = 40\%$, and $\delta/\Delta x = 3$.

Table C.2 The estimate of N for $Re_p = 50$, $u'/U = 40\%$, $\delta/\Delta x = 3$.

Re_λ	20	50	80
d/η	5.1	2.0	1.3
N	400	16,140	105,800

The last column is close to the particle–laden turbulent flows found in CFB or FCC riser; if 20 grids are used to represent particles, N is roughly 10^5 and N^3 needs memory storage space up to petabytes, which is impossible to achieve at this moment.

From the above analysis, one can choose a suitable parameter range for particle–laden turbulent flows if using the pseudo-spectral and the immersed boundary methods to simulate the particle-laden turbulent flows. It is worth noting that the estimation of the memory consumption in this study, is based on the assumption that the underlying numerical grids are uniform Cartesian grids. If other numerical methods are used to approximate the embedded irregular objects in the flow field, the estimation of memory requirement discussed in this section cannot be applied. However the resolution requirements for particle-laden turbulent flows discussed in this Appendix is still useful.

APPENDIX D. TRANSPORT EQUATION FOR THE INSTANTANEOUS KINETIC ENERGY E_f

In this section, the instantaneous kinetic energy E_f is first studied for the laminar flow past a stationary particle, then one MIS run of GCG and MHC is examined respectively.

D.1 The Budget Study for Laminar Flow Past a Stationary particle

Consider the transport equation for the instantaneous kinetic energy of fluid phase $E \equiv \frac{1}{2}\mathbf{U}_f(\mathbf{x},t)\cdot\mathbf{U}_f(\mathbf{x},t)$,

$$\frac{DE}{Dt} + \nabla\cdot\mathbf{T} = -2\nu S_{ij}S_{ij} \tag{D.1}$$

where $S_{ij} \equiv \frac{1}{2}\left(\partial U_j/\partial x_i + \partial U_i/\partial x_j\right)$ is the rate-of-strain tensor, and

$$T_i \equiv \frac{U_i p}{\rho} - 2\nu U_j S_{ij} \tag{D.2}$$

is the flux of energy. Integrating the transport equation for E over the control volume $\mathcal{V}$, we obtain the following equation:

$$\frac{d}{dt}\iiint_{\mathcal{V}} E d\mathcal{V} + \iint_{\mathcal{A}} (\mathbf{U}E + \mathbf{T})\cdot\mathbf{n}dA = -\int_{\mathcal{V}} 2\nu S_{ij}S_{ij}dV. \tag{D.3}$$

For laminar flow past a stationary particle, the time derivative in Eq. D.3 can be neglected since the flow field can be considered to be a stationary process. The second term is the surface integral that accounts for the inflow, outflow and the work done on the control surface, which represents the transfer of E from one region to another. It is also noted that the interface $\mathcal{S}$ includes the interface Ω_p between solid particles and the fluid phase. However on the interface Ω_p, U_j is zero (around machine accuracy), hence the magnitude of T_i is around zero. The value of $\iint_{\Omega_p}\mathbf{T}\cdot\mathbf{n}dS$ calculated from DNS database confirms the observation that the the energy

flux at the particle surface Ω_p is far less than the energy flux at the surface of control volume $\mathcal{A}$.

The flux of energy and the dissipation in the integral equation Eq. D.3 is listed in Table D.1 for the laminar flow past a stationary particle with $Re_p = 50$. The control volume $\mathcal{V}$ contains the sphere, and in x direction the controlled volume starts upstream the 3 particle diameters from the center of the sphere and ends downstream the 5 particle diameters from the center of the sphere. The surface Ω_p is the interface between particle and the fluid, while $\mathcal{A}$ is the outer

Table D.1 The integrals of the energy flux and the dissipation from the instantaneous velocity and pressure fields of upstream turbulence past the single stationary sphere. The percentages in $(\cdot)$ indicate the value of the integrals normalized by the volume integral of the dissipation.

The terms in Eq. D.3	value of the integrals
$\int_{\mathcal{A}} (\mathbf{U}E) \cdot \mathbf{n} dA$	0.568×10^{-4} (-9.3%)
$\int_{\mathcal{A}} \mathbf{T} \cdot \mathbf{n} dA$	-0.693×10^{-3} $(114\%$ $)$
$-\int_{\mathcal{V}} 2\nu S_{ij} S_{ij} dV$	-0.608×10^{-3} $(\ 100\%)$
$\int_{\Omega_p} (\mathbf{U}E + \mathbf{T}) \cdot \mathbf{n} dA$	1.826×10^{-6} (0.3%)
difference	0.286×10^{-6} $(\ 4.7\%)$

surface of the controlled volume $\mathcal{V}$. The sum of energy flux and the dissipation should be zero. From the value in Table D.1 the difference is 4.7% of the dissipation $\int_{\mathcal{V}} 2\nu S_{ij} S_{ij} dV$. This could be due to the methods used to calculate the rate-of-strain S_{ij}. In the calculation of S_{ij} terms, the derivatives in y and z are calculated in Fourier space and transformed back to real space, and this method is know to have very high accuracy. The first order finite difference schemes are used to calculate $\partial(\cdot)/\partial x$, which are expected to be less accurate and will introduce some numerical errors.

From this study, we can observe that the integral of the energy flux along the interface Ω_p is almost zero and the energy flux at the outer surfaces of the control volume $\mathcal{V}$ balances the total dissipation, and the contribution from $\mathbf{U}E$ is small, compared to the flux of energy $\int_{\mathcal{A}} \mathbf{T} \cdot \mathbf{n} dA$.

D.2 The Budget Study for Upstream Turbulence Past the Fixed Bed of Spheres

After evaluating the method used to calculate the transport equation for instantaneous kinetic energy E, we will use this method to study the instantaneous kinetic energy balance for upstream turbulence past a fixed bed of spheres with the particle random arrangements as Matérn hardcore and granular cooling gas.

In the integral equation, the time derivative can be neglected since the upstream turbulence past the fixed bed of sphere can be considered to be a statistically stationary process. The instantaneous energy inside the fixed settles down after half flow through time, and after that the fluid phase instantaneous kinetic energy shows less than 1% variation around the time averaged total energy E, as seen in Figure D.1.

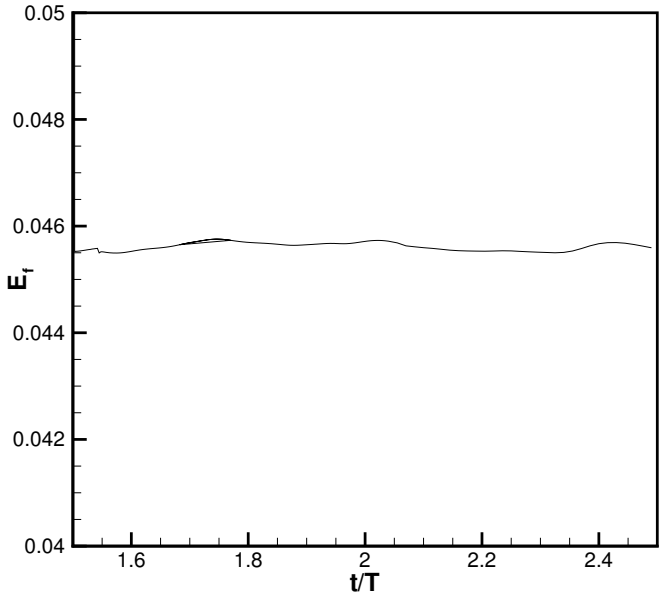

Figure D.1 The evolution of total kinetic energy E for one realization of homogeneous upstream turbulence past a fixed bed of spheres. The reference time T is the one flow through time $T = \frac{L_x}{V}$.

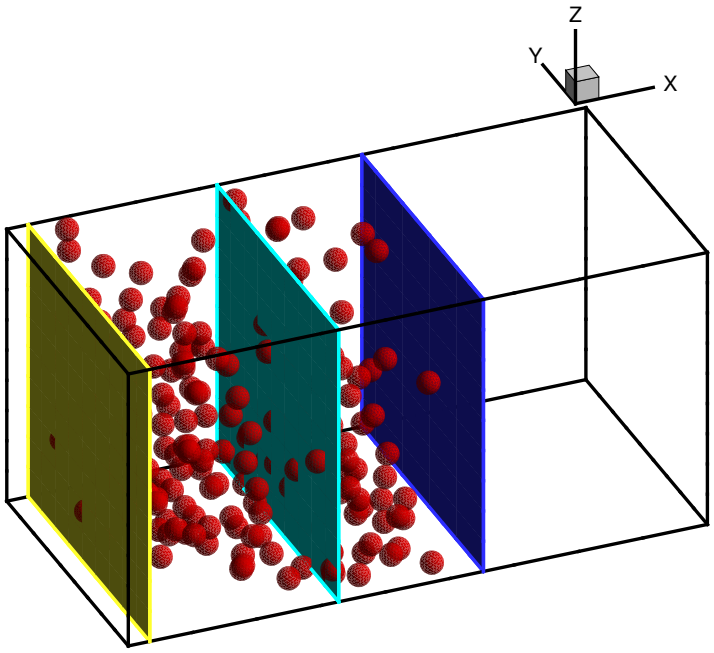

Figure D.2 The control volume used in the budget study of the integral equation of the instantaneous energy E_f.

Table D.2 shows the value of the flux of energy and the dissipation computed for upstream turbulence past a fixed bed of spheres for MHC and GCG. Only one realization from MHC and GCG is studied respectively. The control volume $\mathcal{V}$ is chosen to contain all the particles. For example, in Figure D.2 the control volume starts from yellow plane upstream and ends at the blue plane downstream.

From the data in Table D.2, it is observed that the dissipation from one realization of MHC is 19% more than that from MHC. However the budget study of Eq. D.3 is from the perspective of the single phase turbulence, and the instantaneous kinetic energy $E = \frac{1}{2}U_iU_i$ instead of turbulence kinetic energy k_f is studied.

Table D.2 The integrals of the energy flux and the dissipation from the instantaneous velocity and pressure fields for one MIS of GCG and MHC respectively. The percentages in $(\cdot)$ indicate the value of the integrals normalized by the volume integral of the dissipation.

The term in Eq. D.3	MHC	GCG
$\iint_{\mathcal{A}} \mathbf{U}E \cdot \mathbf{n} d\mathcal{S}$	0.031 (-10.5%)	0.105 (-41.9%)
$\iint_{\mathcal{A}} T \cdot \mathbf{n} d\mathcal{S}$	-0.312 (105.9%)	-0.337 (136.4%)
$-\iiint_{\mathcal{V}} 2\nu S_{ij} S_{ij} dV$	-0.294 (100%)	-0.247 (100%)
the magnitude of difference	0.0135 (4.6%)	0.015 (5.5%)

BIBLIOGRAPHY

Ahmadi, G. (1989). A two-equation turbulence model for compressible flows based on the second law of thermodynamics. *J. Non-Equilib. Thermodyn.*, 14:45–59.

Ahmadi, G. and Ma, D. (1990). A thermodynamical formulation for dispersed multiphase turbulent flows: I basic theory. *Int. J. of Multiphase Flow*, 16(2):323–340.

Ahmed, A. M. and Elghobashi, S. (2000). On the mechanisms of modifying the structure of turbulent homogeneous shear flows by dispersed particles. *Phys. Fluids*, 12(11):2906–2930.

Ahmed, A. M. and Elghobashi, S. (2001). Direct numerical simulation of particle dispersion in homogeneous turbulent shear flows. *Phys. Fluids*, 13:3346–3364.

Amsden, A. A., O'Rourke, P. J. and Butler, T. D. (1989). KIVA–II: A Computer Program for Chemically Reactive Flows with Sprays. Technical report, Los Alamos National Laboratory.

Badia, J. M. and Vidal, A. M. (1993). A parallel algorithm to solve tridiagonal systems on distributedmemory multiprocessors. In *Parallel and Distributed Processing, 1993. Proceedings.*, Gran Canaria, Spain.

Bagchi, P. and Balachandar, S. (2003). Effect of turbulence on the drag and lift of a particle. *Phys. Fluids*, 15(11):3496–3513.

Bagchi, P. and Balachandar, S. (2004). Response of the wake of an isolated particle to an isotropic turbulent flow. *J. Fluid Mech.*, 518:95–123.

Besnard, D. C. and Harlow, F. H. (1985). Turbulence in two–field incompressible flows. Technical report, LA-10187MS, Los Alamos Lab, Albuquerque, NM.

Billingsley, P. (1995). *Probability and Measure*. Wiley-Interscience, 3rd edition edition.

Boivin, M., Simonin, O. and Squires, K. D. (1998). Direct numerical simulation of turbulence modulation by particles in isotropic turbulence. *J. Fluid Mech.*, 375:235–263.

Boivin, M., Simonin, O. and Squires, K. D. (2000). On the prediction of gas-solid flows with two-way coupling using large eddy simulation. *Phys. Fluids*, 12(8):2080–2090.

Bolio, E., Yasuna, J. A. and Sinclair, J. L. (1995). Dilute turbulent gas–solid flow in risers with particle–particle interactions. *AIChE Journal*, 41(6):1375–1388.

Bolio, E. J. and Sinclair, J. L. (1995). Gas turbulence modulation in the pneumatic conveying of massive particles in vertical tubes. *Int. J. of Multiphase Flow*, 21(6):985–1001.

Chen, J.-H., Wu, J.-S. and Faeth, G. M. (2000). Turbulence generation in homogeneous particle–laden flows. *AIAA J.*, 38:636–642.

Clift, R., Grace, J. R. and Weber, M. E. (1978). *Drops and particles*. Academic, New York.

Crowe C., Sommerfeld, M. and Tsuji, Y. (1998). *Multiphase flows with droplets and particles*. CRC Press.

Drew, D. A. (1983). Mathematical modeling of two-phase flow. *Ann. Rev. Fluid Mech.*, 15:261–291.

Drew, D. A. and Passman, S. L. (1999). *Theory of multicomponent fluids*, volume 135 of *Applied mathematical sciences*. Springer.

Elghobashi, S. and Abou-Arab, T. (1983). A two–equation turbulence model for two–phase flows. *Phys. Fluids*, 26:931–938.

Elghobashi, S., Abou-Arab, T., Rizk, M. and Mostafa, A. (1984). Prediction of the particle-laden jet with a two-equation turbulence model. *Int. J. of Multiphase Flow*, 10(6):697–710.

Elghobashi, S. (1991). Particle-laden turbulent flows: direct simulation and closure models. *Applied Scientific Research*, 48(3-4):301–314.

Elghobashi, S. and Truesdell, G. C. (1993). On the two–way interaction between homogeneous turbulence and dispersed solid particles, I:turbulence modification. *Phys. Fluids A*, 5(7):1790–1801.

Fallon, T. and Rogers, C. B. (2002). Turbulence-induced preferential concentration of solid particles in microgravity conditions. *Experiments in Fluids*, 33:233–241.

Ferrante, A. and Elghobashi, S. (2003). On the physical mechanisms of two–way coupling in particle isotropic turbulence. *Phys. Fluids*, 15(2):315–329.

Garg, R., Ferziger, J. H. and Monismith, S. G. (1997). Hybrid spectral finite difference simulations of stratified turbulent flows on distributed memory architectures. *International Journal For Numerical Methods in Fluids*, 24:1129–1158.

Glowinski, R., Pan, T. W., Hesla, T. I., Joseph, D. D. and Periaux, J. (2001). A fictitious domain approach to the direct numerical simulation of incompressible viscous flow past moving rigid bodies: application to particulate flow. *J. Computational Physics*, 169:363–426.

Goldstein, D., Handler, R. and Sirovich, L. (1993). Modeling a no–slip flow boundary with an external force field. *J. Comp. Phys.*, 105(2):354–366.

Gore, R. A. and Crowe, C. T. (1989). Effect of particle size on modulating turbulent intensity. *Int. J. Multiphase Flows*, 15(2):279-285

Hill, R. J., Koch, D. L. and Ladd, A. J. C. (2001a). The first effects of fluid inertia on flows in ordered and random arrays of spheres. *J. Fluid Mech.*, 448:213–241.

Hill, R. J., Koch, D. L. and Ladd, A. J. C. (2001b). Moderate-reynolds-numbers flows in ordered and random arrays of spheres. *J. Fluid Mech.*, 448:243–278.

Hu, H. H., Patankar, N. A. and Zhu, M. Y. (2001). Direct numerical simulations of fluid–solid systems using the arbitrary lagrangian–eulerian technique. *J. Computational Physics*, 169(427-462).

Hwang, W. and Eaton, J. K. (2004). *Modification of Homogeneous and Isotropic Turbulence by Solid Particles*. PhD dissertation, Stanford University.

Hwang, W. and Eaton, J. K. (2006a). Homogeneous and isotropic turbulence modulation by small heavy (St $\sim$ 50) particles. *J. Fluid Mech.*, 564:361–393.

Hwang, W. and Eaton, J. K. (2006b). Turbulence attenuation by small particles in the absence of gravity. *Int. J. of Multiphase Flow*.

Kaneda, Y. and Yakokawa, M. (2005). Dns of canonical turbulence with up to 4096^3. In Winter, G., editor, *Parallel Computational Fluid Dynamics 2004: Multidisciplinary Applications*, pages 23–32. Elsevier.

Kataoka, I., Serizawa, A. and Matsumoto, T. (1989). Basic equations of turbulence in gas-liquid two-phase flow. *Int. J. of Multiphase Flow*, 15(5):843–855.

Kim, J. and Moin, P. (1985). Application of a fractional-step method to incompressible navier–stokes equations. *J. Computational Physics*, 59:308–323.

Koch, D. L. and Hill, R. J. (2001). Inertial effects in suspension and porous-media flows. *Annu. Rev. Fluid Mech.*, 33:619–647.

Kunii, D. and Levenspiel, O. (1969). *Fluidization Engineering*. John Wiley & Sons.

Launder, B. E. (1996). An introduction to single-point closure methodology. In T.B. Gatski, M. H. and Lumley, J., editors, *Simulation and Modeling of Turbulent Flows*, chapter 6, pages 243–310. Oxford University Press, New York.

Legendre, D., Merle, A. and Magnaudet, J. (2006). Wake of a spherical bubble or a solid sphere set fixed in a turbulent environment. *Phys. Fluids*, 18(4):048102.

Ma, D. and Ahmadi, G. (1990). A thermodynamical formulation for dispersed multiphase turbulent flows: II simple shear flows for dense mixtures. *Int. J. of Multiphase Flow*, 16(2):341–351.

Mashayek, F. and Taulbee, D. B. (2001). Statistics in particle-laden plane strain turbulence by direct numerical simulation. *Int. J. Multiphase Flow*, 27(2):347–378.

Mashayek, F. and Taulbee, D. B. (2002). Turbulent gas-solid flows, part i: Direct simulations and reynolds stress closures. *Numerical Heat Transfer, Part B: Fundamentals*, 41(1):1–29.

Maxey, M. R. and Riley, J. J. (1983). Equation of motion for a small rigid sphere in a non-uniform flow. *Phys. Fluids*, 26:883–889.

Mizukami, M., Parthasarathy, R. N. and Faeth, G. M. (1992). Particle-generated turbulence in homogeneous dilute dispersed flows. *Int. J. of Multiphase Flow*, 18(3):397–412.

Moran, J. C. and Glicksman, L. R. (2003b). Mean and fluctuating gas phase velocities inside a circulating fluidized bed. *Chemical Engineering Science*, 28(9):1867–1878.

Moran, J. C. and Glicksman, L. R. (2003a). Experimental and numerical studies on the gas flow srrounding a single cluster applied to a circulating fluidized bed. *Chemical Engineering Science*, 58(9):1879–1886.

Moses, B. and Edwards, C. (2005). LES_Stype Filtering and partly-Resolved Particles. In *Americas 18th Annual Conference on Liquid Atomization and Spray Systems*, Irvine, CA. ILASS.

Mostafa, A. and Elghobashi, S. (1985). Two–equation turbulence model for jet flows laden with vaporizing droplets. *Int. J. of Multiphase Flow*, 11(4):515–533.

Orszag, S. and Patterson, G. (1972). Numerical simulation of three-dimensional homogeneous isotropic turbulence. *Phys. Rev. Lett.*, 28:76–79.

Pai, G. M. and Subramaniam, S. (2004). Analysis of turbulence models in Lagrangian-Eulerian spray computations. In *Proceedings of the 17th Annual Conference on Liquid Atomization and Spray Systems*. Intl. Liquid Atomization and Spray System Soc.

Pai, G. M. and Subramaniam, S. (2006). Modeling interphase turbulent kinetic energy transferin lagrangian-eulerian spray computations. *Atomization and Sprays*, 16(7):807–826.

Parthasarathy, R. N. and Faeth, G. M. (1990). Turbulence modulation in homogeneous dilute particle–laden flows. *J. Fluid Mech.*, 220:485–514.

Peskin, C. S. (1977). Flow patterns around heart valves: a numerical method. *J. Comp. Phys.*, 25.

Peskin, C. S. (2002). The immersed boundary method. *Acta Numerica*, 11:479–517.

Pope, S. B. (1999). *Turbulent flows*. Cambridge University Press.

Povitsky, A. (1998). Parallelization of the pipelined thomas algorithm. Technical Report NASA/CR-1998-208736, Institute for Computer Applications in Science and Engineering, NASA Langley Research Center, Hampton, VA. ICASE Report No. 98-48.

Pruppacher, H. R., Le Clair, B. P. and Jamoelec, A. E. (1970). Some relations between drag and flow pattern of viscous flow past a sphere and a cyliner at low and intermediate reynolds numbers. *J. Fluid Mech.*, 44(4):781–790.

Rogallo, R. S. (1981). Numerical experiments in homogeneous turbulence. Technical Report TM81315, NASA.

Sangani, A. S., Mo, G., Tsao, H.-K. and Koch, D. L. (1996). Simple shear flows of dense gas-solid suspensions at finite stokes numbers. *J Fluid Mech.*, 313:309–341.

Schumann, U. (1977). Realizability of reynolds-stress turbulence models. *Phys. Fluids*, 20(5):721–725.

Sheng, J., Meng, H. and Fox, R. O. (2000). A large eddy piv method for turbulence dissipation rate estimation. *Chem. Engng Sci.*, 55:4423–4434.

Simonin, O. (1996a). Continuum modeling of dispersed turbulent two-phase flows part 2: Model predictions and discussion. Technical report, Von Karman Institute of Fluid Dynamics Lecture Series.

Simonin, O. (1996b). Continuum modelling of dispersed turbulent two-phase flows part 1: General model description. Technical report, Von Karman Institute of Fluid Dynamics Lecture Series.

Sinclair, J. and Jackson, R. (1989). Gas-particle flow in a vertical pipe with particle-particle interactions. *AIChE J*, 35:1473–1486.

Snir, M., Otto, S., Huss-Lederman, S., Walker, D. and Dongarra, J. (1998). *MPI–The complete reference*, volume 1. The MPI Press, second edition.

Sofiane, B. (2002). Private communication. MFIX mail list, WWW.MFIX.ORG.

Squires, K. D. and Eaton, J. K. (1990). Particle response and turbulence modification in isotropic turbulence. *Phys. Fluids A*, 2(7):1191–1203.

Stoyan, D., Kendall, W. S. and Meche, J. (1986). *Stochastic Geometry and its applications*. Probability and mathematical statistics. John Wiley & Sons.

Subramaniam, S. (2000). Statistical representation of a spray as a point process. *Phys. Fluids*, 12(10):2413–2431.

Subramaniam, S. (2001). Statistical modeling of sprays using the droplet distribution function. *Phys. Fluids*, 13(3):624–642.

Subramaniam, S. (2002). Properly constrained interphase momentum transfer models for constant-density two-phase flow: resolution of the ill-posedness issue in canonical problems. In *15th Annual Conference on Liquid Atomization and Spray Systems*. ILASS.

Subramaniam, S. (2003). Modeling turbulent two–phase flows. In *16th Annual Conference on Liquid Atomization and Spray Systems*. ILASS.

Sundaram, S. and Collins, L. R. (1999). A numerical study of the modulation of isotropic turbulence by suspended particles. *J. Fluid Mech.*, 379(9):105–143.

Ten Cate, A., Derksen, J. J., Portela, L. M., and Van Den Akker, H. E. A. (2004). Fully resolved simulations of colliding monodisperse spheres in forced isotropic turbulence. *J. Fluid Mech.*, 519:233–271.

Tsao, H.-K. and Koch, D. L. (1995). Simple shear flows of dilute gas-solid suspensions. *J. Fluid Mech.*, 296:211–245.

Tsuji, Y., Morikawa, Y. and Shiomi, H. (1984). LDV measurements of an air-solid two-phase flow in a vertical pipe. *J. Fluid Mech.*, 139:417–434.

Wylie, J. J. and Koch, D. L. (1999). Clustering of suspensions in stoke's flow. *Phys. Fluids*, 12:964.

Wylie, J. J., Koch, D. L. and Ladd, A. J. C. (2003). Rheology of suspensions with high particle inertia and moderate fluid inertia. *J. Fluid Mech.*, 480:95.

Van der Hoef, M. A., Beetstra, R. and Kuipers, J. A. M. (2005). Lattice-boltzmann simulations of low-reynolds-number flow past mono- and bidisperse arrays of spheres: results for the permeability and drag force. *J. Fluid Mech.*, 528:233–254.

Williams, F. A. (1958). Spray combustion and atomization. *Phys. Fluids*, 1(6):541–545.

Xu, Y. (2004). An improved multiscale model for dilute turbulent gas–particleflows based on the equilibration of energy concept. Master's thesis, Iowa State University.

Xu, Y. and Subramaniam, S. (2006). A multiscale model for dilute turbulent gas-particle flows based on the equilibration of energy concept. *Phys. Fluids*, 18.

Yang, T. S. and Shy, S. S. (2005). Two-way interaction between solid particles and homogeneous air turbulence: particle settling rate and turbulence modification measurements. *J. Fluid Mech.*, 526:171–216.

Yusof, M. (1996). *Interaction of massive particles with turbulence.* PhD dissertation, Cornell University.